Diffusion of implanted silver and cesium in glassy carbon

by

Dolly Frans Langa

Submitted in partial fulfillment of the requirements for the degree

PHILISOPHIAE DOCTOR (PhD) in Physics

In the Faculty of Natural and Agricultural Sciences at the University of Pretoria

April…...2019

Supervisor/Promoter: Prof. J.B. Malherbe

SUMMARY

Diffusion of implanted silver and cesium in glassy carbon

By

Dolly Frans Langa

Submitted in partial fulfillment of the requirements for the degree of (PhD) in Physics in the Faculty of Natural and Agricultural Sciences at the University of Pretoria

Supervisor/Promoter: Prof. J.B. Malherbe

Glassy carbon also known as vitreous carbon has a number of special properties making it a very interesting material with many applications. It is a non-graphitizing carbon which combines glassy and ceramic properties with those of graphite. Among the several interesting and unique properties of glassy carbon, are: extremely high corrosion resistance, high temperature resistance up to 3000°C, and impermeable to gases and liquids. Glassy carbon is manufactured by the carbonization (pyrolysis) of an organic precursor. It consists of very small crystallites randomly orientated. The bonds are mostly sp^2 but also with some sp^3.

The effects of ion implantation and subsequent annealing on the surface topography, structural changes and on the diffusion of cesium and silver into glassy carbon (Sigrador® G) are reported. The in-diffusion investigation was only done for the silver into the glassy carbon. The glassy carbon samples with 100 nm thickness layer of naturally occurring silver on their surface were vacuum annealed for 5 hours at temperatures of 600°C and 750°C. No silver in-diffusion was observed but the silver conglomerated on the surface into island structures Cesium and silver ions were separately implanted into glassy carbon at 360 keV to a fluence of 2×10^{16} ions/cm^2 at room temperature, 350°C and 600°C. To remove surface irregularities before implantation the glassy carbon samples were mechanically polished with diamond paste to a mirror finish and chemically cleaned.

The cesium and silver implanted glassy carbon samples were investigated under different annealing conditions. The influence of ion implantation and annealing on the surface topography was investigated by the scanning electron microscopy (SEM). The SEM results of the samples showed that implantation and subsequent annealing strongly influenced the surface morphology of the glassy carbon. The SEM also showed a great difference in the surface topography of the polished virgin glassy carbon surface as compared to the as-implanted samples. The effects of laser beam annealing under ambient air and moisture during Raman measurements at high power on the cesium implanted glassy carbon sample are also reported. The SEM study on the spot where the laser beam was focused showed that the damaged carbon layers were removed, exposing the bulk of the material that was not affected by cesium implantation.

The Raman spectroscopy was used to monitor the corresponding structural changes induced in glassy carbon due to ion implantation and subsequent annealing. This investigation was only done for the cesium implanted glassy carbon. The Raman spectrum of the polished virgin glassy carbon surface, which is a disordered carbon, showed two sharp peaks, namely the D (disorder) and G (graphite) peaks at 1350 cm^{-1} and 1592 cm^{-1}, respectively. The Raman study showed that there was less damage in to glassy carbon when cesium was implanted at high temperatures than at room temperature. Upon annealing the room temperature cesium implanted glassy carbon sample, Raman spectroscopy showed that there was some recrystallization of the glassy carbon. This means that some of the damage due to implantation were annealed out.

The depth profiles of the as-implanted samples and subsequent annealing were obtained by Rutherford backscattering spectrometry (RBS). RBS-determined depth profiles of the glassy carbon implanted with cesium ions revealed that there is a strong redistribution of the cesium ions towards the surface. The redistribution of the cesium occurred already at room temperature implantation and enhanced at elevated substrate implantation temperature. However, no implanted cesium atoms were lost in that process, but rather accumulated on the surface of glassy carbon. Contrary, annealing the glassy carbon implanted with cesium at room temperature, resulted not only in the diffusion and redistribution of cesium but also in a significant sublimation/evaporation of cesium into the vacuum.

The RBS determined depth profiles of the glassy carbon implanted with silver at room temperature, then annealed isothermally at 350°C at times ranging from 30 minutes to 3 hours showed not much diffusion of silver into the glassy carbon. There was no real broadening of the Ag implanted profile, indicating no or little diffusion of the silver into the bulk of the substrate material and towards the surface. Isochronal annealing of the room temperature silver implanted glassy carbon sample for 1 hour at temperatures ranging from 400°C to 700°C showed continuous loss of silver. After annealing at 700°C, the silver disappeared completely from the glassy carbon being lost in the vacuum. To calculate the diffusion coefficient of silver in glassy carbon, the optimum temperature of 575 °C was chosen. The diffusion coefficient of silver into glassy carbon was calculated to be $D = 5.30 \times 10^{-2}$ nm^2/s.

DECLARATION

I, Dolly Frans Langa, declare that the thesis, which I hereby submit for the degree PhD in Physics at the University of Pretoria is my own work and has not been previously submitted by me for a degree at this or any other tertiary institution.

Signature: ……  ……..…….

Date: …02 April 2019…….

ACKNOWLEDGEMENTS

I would like to sincerely thank the following people and institutions for their valuable contribution towards this study.

i. My supervisor, Prof. J.B. Malherbe for his patient and thorough guidance, discussions and support throughout this academic journey.

ii. Prof. E. Friedland for being prepared to give much needed advice and criticism.

iii. Dr N. van der Berg for his support and guidance to discover such interesting results and to take to heart the truth he so generously shared about Analytical Physics.

iv. Mr A.J. Botha, for the help with Scanning Electron Microscopy.

v. Prof. C. Theron and Dr T.T. Hlatshwayo, for all the help with the accelerator.

vi. Dr. L. Prinsloo and Dr M Mlambo, for the help, discussion and advice with the Raman Spectroscopy.

vii. SANHARP, University of Pretoria, National Research Foundation, and *Bundesministerium für Bildung und Forschung* (Germany) for their financial support is gratefully acknowledged.

viii. Fellow post graduate students for the encouragement and moral support.

ix. My three brothers and my sister, you have each contributed in your special way, and I cherish our bond.

x. I dedicate this to my two sons, Tshepo and Kabelo, and daughter Bontle – although I have tried to express appreciation and gratitude for you're ever ending love, emotional support and belief in me, it can never compensate for all the hardships you have had to endure because of my studies.

TABLE OF CONTENTS

CHAPTER 1

INTRODUCTION

Since the beginning of the twentieth century, research and development in the field of nuclear science and technology have led to wide scale applications in research, medicine, industry and in the generation of electricity by nuclear fission. In common with certain other human activities, these practices generate waste that requires management to ensure the protection of human health and the environment now and in the future, without imposing undue burdens on future generations. The current preferred disposal option is to store it in containers on the earth's surface. Materials issues are important during the entire process of nuclear-waste management; performance of the materials used in nuclear waste management determines its safety/hazards. It is from this background that in this dissertation we investigated the suitability of glassy carbon (SIGRADUR® G) as a containment material for storage of radioactive waste. The focus is specifically on diffusion barrier properties of glassy carbon to silver and cesium at various annealing temperatures and times.

1.1 NUCLEAR WASTE AND NUCLEAR WASTE CONTAINERS

Radioactive nuclear wastes comprise a variety of materials requiring different types of management to protect people and the environment. They are normally classified as low-level waste (LLW), medium-level waste (MLW) and high-level waste (HLW), according to the amount and types of radioactivity in them. Low-level waste is generated from hospitals, laboratories and industry, as well as the nuclear fuel cycle. It comprises paper, rags, tools, clothing, filters, etc. which contain small amounts of mostly short-lived radioactivity. It is not dangerous to handle, but must be disposed of more carefully than normal garbage. Medium-level waste contains higher amounts of radioactivity and may require special shielding. It typically comprises resins, chemical sludge and reactor components, as well as contaminated materials from reactor decommissioning. High-level waste may be the used fuel itself, or the principal waste from reprocessing [1]. LLW and HLW represent the most important types of nuclear waste. In terms of volume, LLW takes up about 85% of the nuclear waste generated, while more than 99% of the total radioactivity in nuclear waste is contained in HLW [2].

A key consideration in nuclear waste management is the development of highly durable waste containers that ensure the long-term stability of the materials, the isolation of radioactivity during transportation, interim storage and disposal, and non-leakage from the container. Waste materials used for the burial of low-level waste (LLW) include carbon-steel drums, liners, and boxed and high-integrity containers (HICs). They are placed in a disposal facility with either soil or cement backfills. Carbon steel containers are inexpensive, but undergo both uniform corrosion and pitting corrosion within the soil and cemented systems. Hence, the life time of carbon steel containers in a disposal system is expected to be short. The type of HICs widely used is a combination of both a high-density polyethylene and concrete over pack. This type of high-integrity container is expected to fail eventually by degradations of the concrete casing and creep of high-density polymers [3].

High-level waste (HLW) package materials are subjected to harsh environments and various kinds of physical and chemical stress. The presence of HLW inventory will lead to elevated temperatures and high levels of radiation. The host media for the repository can be the sources of oxygen and water which will cause oxidation of the container material, resulting in the loss of structural integrity. Radiation effects, such as radiation hardening and embrittlement, enhance diffusion, and enhanced creep rate, must be taken into consideration. Candidate materials for HLW canisters and over packs are generally metals such as copper, iron, stainless steel, titanium alloys, and nickel-based alloys [4].

i. Studies on native copper deposits and archaeological artifacts indicate very good environmental stability [5]. However, it is known to be poor in brine as well as in radiation environment [6].

ii. Iron is not very corrosion-resistant, but is less prone to catastrophic failure.

iii. Stainless steel has good mechanical properties and very corrosion resistant, but catastrophic failures are possible through stress-corrosion cracking or intergranular corrosion.

iv. Titanium alloys are mechanically strong and possess good corrosion resistance. However, they can experience brittle failure with the uptake of hydrogen.

v. Nickel-based alloys are similar to titanium in that they are very corrosion resistant. They are easier to weld that titanium, but could be more expensive [2].

1.2 GLASSY CARBON (SIGRADUR® G)

Carbon is one of the elements capable of forming variable structures. It forms a great variety of crystalline and disordered structures because it can exit in three hybridisations, namely; sp^3, sp^2 and sp, as shown in figure 1.1. In the sp^3 configuration as in diamond, a carbon forms four sp^3 orbitals, which makes a strong σ bond to an adjacent atom. In the sp^2 configuration as in graphite, a carbon atom makes three sp^2 orbitals to form σ bonds and the fourth $p\pi$ orbital form a π bond. In the sp^1 configuration there are two σ bonds in the $\pm x$-axis and two $p\pi$ bonds along the y and z directions [7].

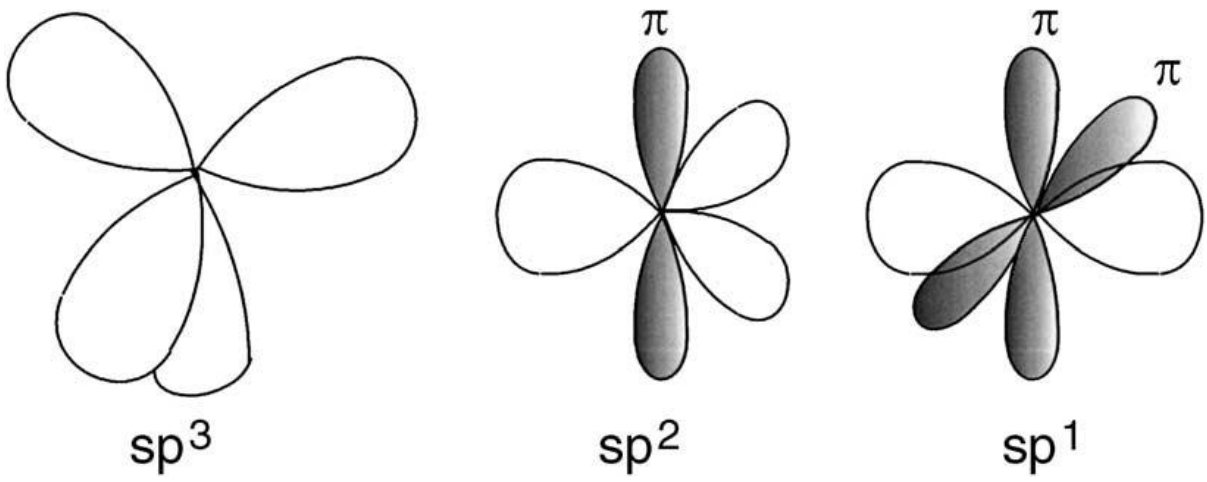

Figure 1.1. The sp^3, sp^2, sp hybridised bonding of carbon. Taken from [7].

These allotropes, such as diamond and graphite, can have drastically different properties despite the chemical similarity of the material. As carbon has strong covalent bonds, the strong bonds make it possible to construct much larger and exotic entities such as fullerenes and carbon nanotubes consisting of hundreds of individual carbon atoms. The process of developing carbon material in which carbon atoms are the principal constituents is called carbonization (or pyrolysis). This process involves the heat treatment of some carbon precursors which depends strongly on the carbon precursors and the conditions of heat treatment (temperature, heating rate, atmosphere, etc.). In most cases the stacking of the carbon layer is random. In order to make these carbon layer to grow and stack in a graphitic structure, heat treatment at a high temperature above 2500 °C is needed. In some cases the graphitic structure develops and the process is called graphitization. However, it does not always occur, the development of a graphitic structure depends on the carbonization process. When the carbonization of precursors

like resins occurs rapidly, the resultant carbon materials are porous. If the carbonization process is performed so slowly that the resultant solid carbon could shrink, so called glass-like carbons are produced, which contain a large amount of closed pores [8]. Carbonization of most hydrocarbons form carbon materials like coke which are readily converted into well-ordered graphite when the temperature passes the carbonization temperature, i.e. 1200 °C [9].

Glassy carbon (GC), also called vitreous carbon, is an advanced material of pure carbon combining glassy and ceramic properties with those of graphite. It is known that carbons produced by the solid-phase pyrolysis of organic materials falls into two distinct classes. The graphitizing carbons tend to be soft with relatively high densities, and can be readily transformed to crystalline graphite by heating at temperatures in the range 2200 – 3000 °C. In contrast, non-graphitized carbons are hard, low density materials that cannot be transformed into crystalline graphite even at high temperatures [10]. Glassy carbon is made by the process called solid phase pyrolysis, whereby the resins as precursor are heated very slowly at temperature in the range 900 – 1000 °C [11]. Allowing the carbonized products to shrink homogeneously by keeping their forms which have random orientation and contains large amount of closed pores [8]. Among the glassy carbon family, different types can be produced depending on the temperature during carbonization. The glassy carbon Sigradur® G, which we used in this study, is manufactured at higher temperatures than their counterpart Sigradur® K. Their physical properties are different, for example the later has a higher density than the former. Glassy carbon is an example of a non-graphitizing carbon, which is a carbon that cannot be transformed into crystalline graphite even at temperature of 3000ºC [12]. The structure of glassy carbon has been the subject of research since it was first produced in the early 1960s. It has a fullerene-related microstructure and this leads to a great variety of unique material properties making it a very interesting material with many applications. Due to its high purity glassy carbon is suitable for applications in the chemical analysis, semiconductor technology and ultra-pure materials technology.

1.2.1 STRUCTURE OF GLASSY CARBON

Some of the earliest models of glassy carbon assumed, described the presence of both sp^2 and sp^3 bonded atoms [13]. Graphitic domains were considered to be interspersed with tetrahedral domains, perhaps linked by short oxygen containing bridges. The sp^2 bonded carbon atoms are arranged in planes with a hexagonal symmetry. Non-six membered rings (pentagons

and heptagons) bend the hexagonal carbon plane. Based on the assumption that the molecular orientation of the polymeric precursor material is memorized to some extend after carbonization; a model shown in figure 1.2 was put forward. Thus the structure bears some resemblance to that of a polymer, in which fibrils are very narrow, curved and twisted ribbons of graphitic carbon. Micro-structurally, it consists of a tangle of graphite like ribbons or micro-fibrils. These fibres are of the order of 100Å long and 30 Å wide [14].

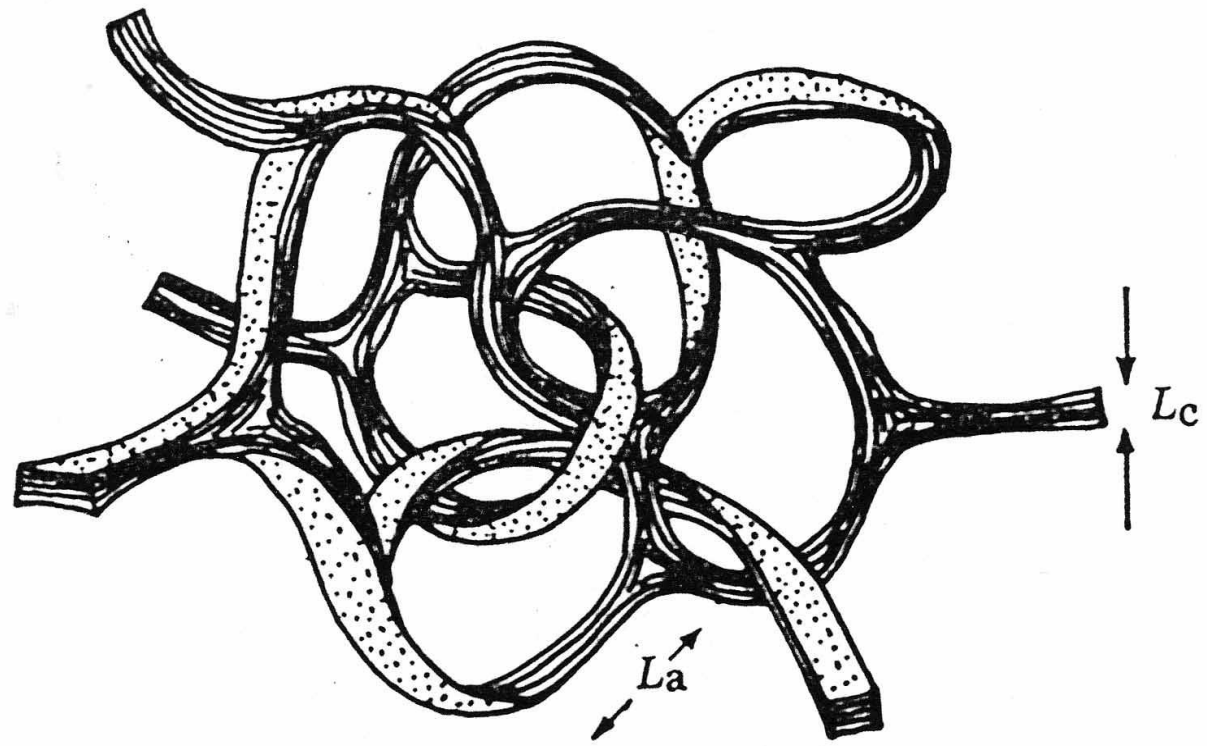

Figure 1.2 The Jenkins-Kawamura model of glassy carbon. L_a and L_c are the lengths of the graphitic domain perpendicular and parallel to the graphitic *c* axis. Taken from [13].

Detailed studies of non-graphitizing carbons prepared by pyrolysis of sucrose and graphitizing carbon prepared by pyrolysis of aromatic hydrocarbon (anthracene) were carried out using high-resolution transmission electron microscopy (TEM). Figure 1.3 shows typical TEM images of non-graphitizing and graphitizing carbons prepared at 1000°C, with the insert showing diffraction patterns. The micrograph of the non-graphitizing carbon, Fig. 1.3 (a), shows the structure to be disordered consisting of tightly curled single carbon layer, and the diffraction pattern showing diffused rings which is the characteristic of a disordered or amorphous materials. While on the other hand, the appearance of the graphitizing carbon, Fig. 1.3 (b), closely resembles that of graphite and heating at 2600°C in inert atmosphere produces

large crystals of highly ordered graphite [15]. The diffraction pattern of the insert shows that there is a preferred orientation of the crystals.

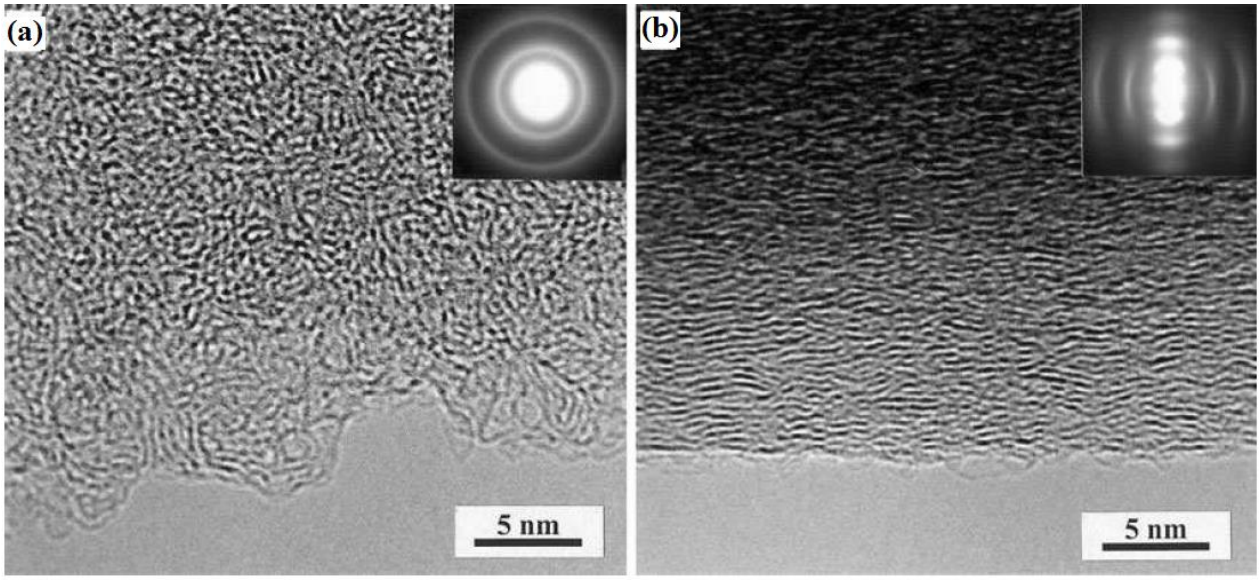

Figure 1.3. TEM image of the microstructure of carbons prepared by (a) pyrolysis of sucrore in a nitrogen atmosphere at 1000°C and (b) pyrolysis of aromatic hydrocarbon anthracene at 1000°C. Taken from [15].

Heat-treating non-graphitizing carbon at a temperature of 2600°C in inert atmosphere produces the disordered and porous material as shown in Fig. 1.4. Their structure shows that they contained closed nanoparticles, often hexagonal or pentagonal in shape, which are made up of curved and faceted graphitic layers. The closed nature of the nanoparticles and their hexagonal or pentagonal shape provided evidence that the particles have a completely closed fullerene-like structure [15].

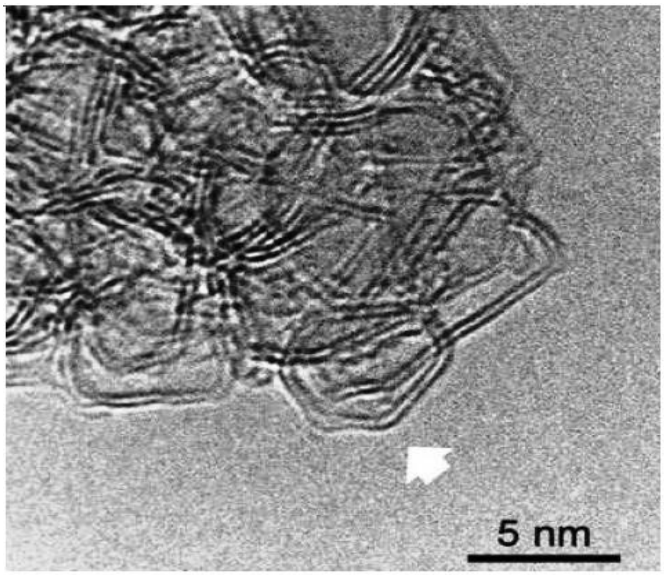

Figure 1.4. TEM micrograph showing the closed structure a polymer derived carbon heated at 2600°C in inert atmosphere. Taken from [15].

1.2.2 CHARACTERISTIC PROPERTIES

Unlike graphite, glassy carbon has a fullerene-related microstructure. This leads to a great variety of unique material properties [10] [16], viz.:

i. *High temperature resistance* in inert gas or vacuum up to 3000°C. Glassy carbon increase in strength and shows no loss of ductility with a rise in temperature up to 2700 K.
ii. Due to its closed microstructure glassy carbon has high *corrosion resistance* to acid and alkaline agents. However, strong oxidizing substances like oxygen over 600°C can attack glassy carbon. Graphite is reduced to a power in concentrated sulphuric and nitric acids at room temperature, while glassy carbon is unaffected by such treatment even after several months.
iii. *Impermeable* to gas and liquids, no open porosity, and shows *no wetting* by metallic melts.
iv. It has *high hardness and strength* but *low density*.
v. It has *low thermal expansion* and *extreme resistance to thermal shock*. Therefore, it retains its shape under heat treatment which is very advantageous for all high temperature conditions.

These properties are the key factors in the development of highly durable waste containers that ensures the long-term stability of the materials and the isolation of radioactivity during transportation, interim storage and disposal

1.3 DIFFUSION IN GLASSY CARBON

A number of diffusion studies of impurities, like beryllium, cobalt and manganese, have been done on glassy carbon. Prior to publication [17] no previous cesium migration data for glassy carbon was available. It is reasonable to expect that the ballistic collisions processes taking place inside the glass-carbon substrate materials during implantation process may cause local compositional and short-range structural changes (i.e. radiation damage) within the material, which can act as diffusion traps for the implanted material during annealing. This will then cause different diffusion kinetics. To illustrate this, two examples are described in some detail below.

Migration kinetics of low concentration implanted beryllium in glassy carbon at annealing temperatures of 1285 °C and 1340 °C was reported, with the annealed sample concentration profiles showing two distinctive components, as shown in figure 1.3 [18].

i. The main profile broadening assigned to beryllium trapping in defects during annealing.

ii. Tails on both sides of the profile maximum related to faster migration.

The results of the deduced diffusion coefficients of Be migration for both tails, viz. the damaged and defect-free material are shown in table 1.1. It was concluded in this work by [18] that it would seem that light impurity atom diffusion in glassy carbon is of the same magnitude than in diamond.

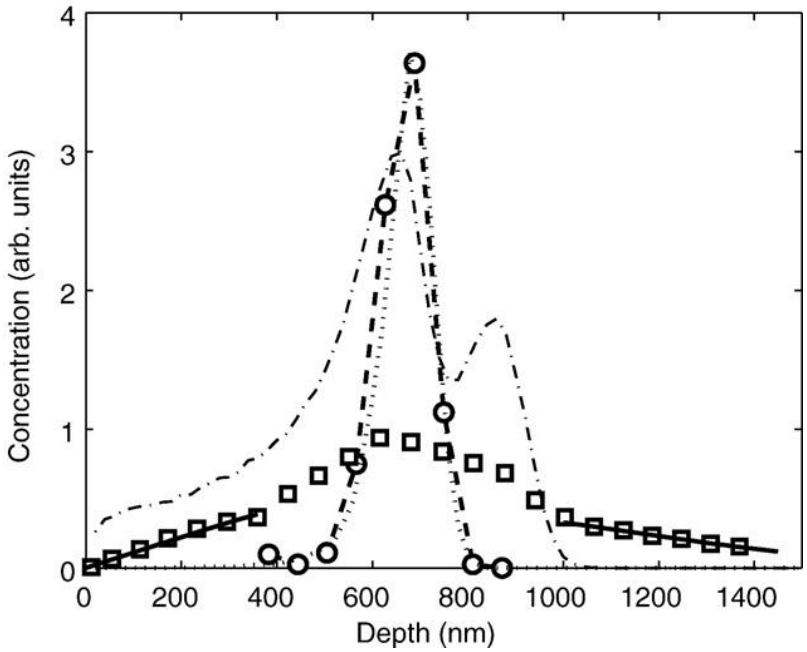

Figure 1.5. Measured (O and dashed line drawn to guide the eye) and SRIM-2008 calculated (dotted line) 7Be profiles in GC produced by 260 keV implantation (O) and subsequent annealing at 1340 for 45 min (□). The solid lines represent the fits of the appropriate solution of the diffusion equation to the profiles representing the migration towards the surface and into the bulk. The vacancy distribution produced by the 7Li and 7Be co-implantation as calculated by the SRIM program is described by the dash-dotted line. Taken from [18].

Table 1.1. Annealing parameters and the deduced diffusion coefficient values for the migration of the implanted beryllium in glassy carbon [18].

Annealing temperature	Annealing Time [min]	Diffusion coefficients [m^2/s]	
		Damaged Material	Defect-free material
1285	30	$(3.0 \pm 0.5) \times 10^{-17}$	$(2.2 \pm 0.3) \times 10^{-17}$
1340	45	$(2.5 \pm 0.3) \times 10^{-17}$	$(4.5 \pm 0.3) \times 10^{-17}$

Helium diffusion coefficients measurements in R7T7 borosilicate glass were also previously reported. It was shown that helium concentration depth profile broadens with the annealing temperature and time, due to the helium diffusion with the glassy matrix. Helium

mobility was observed at annealing temperature as low as 253 K. From temperatures of 273K, an asymmetry in the depth profiles appeared to reveal anisotropy of the helium diffusion [19]. There was increased diffusion in the surface region which experienced radiation damage. These results are shown in figure 1.6.

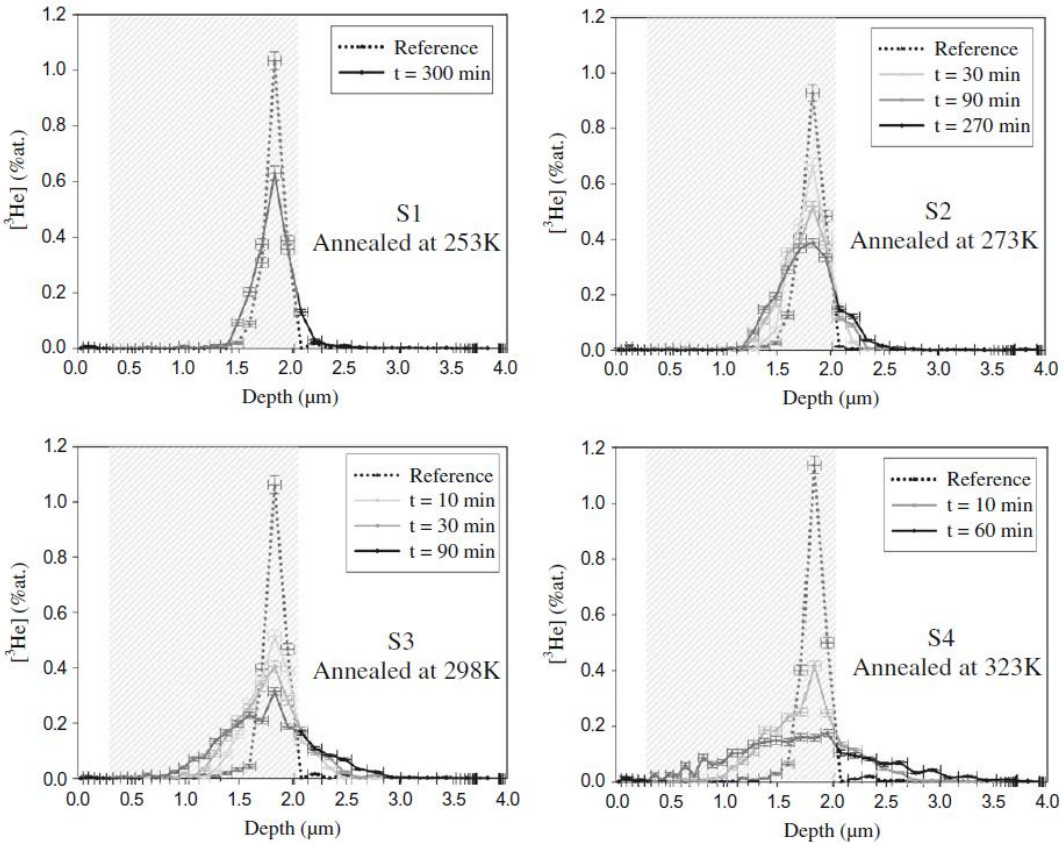

Figure 1.6. Depth profiles of R7T7 borosilicate glass implanted with 600 keV ^{3}He at 2×10^{16} $^{+}$He/cm^{2}, then annealed at 253 K, 273 K, 298 K and 323 K. Taken from [19].

1.4 THESIS SCOPE AND OBJECTIVES

Since the ultimate aim is to investigate the suitability of glassy carbon (Sigradur® G) as a containment material for long-term storage of radioactive waste, the scope and objectives of this research is to investigate the following:

i. Diffusion barrier properties of glassy carbon to implanted silver and cesium at various annealing temperatures and times. The diffusion mechanisms of silver and cesium through glassy carbon at these temperatures will be investigated.

ii. The effects of ion implantation and heat treatment on the surface of glassy carbon.

To investigate these, glassy carbon was implanted separately with silver and cesium at room and at high temperatures (350 and 600 °C). The room temperature implanted samples were isochronally vacuum annealed at temperatures ranging from 200 °C to 800 °C for one hour. All samples were studied by Rutherford backscattering spectrometry (RBS), scanning electron microscopy (SEM) and Raman spectroscopy.

1.5 REFERENCES

[1] "Nuclear Waste," 2015. [Online]. Available: www.world-nuclear.org/education/waste.htm. [Accessed: 20-Aug-2015].

[2] M.-S. Yim and K. Linga Murty, "Materials Issues in Nuclear Waste Management," *J. Miner. Met. Mater. Soc.*, vol. 52, pp. 26–29, 2000.

[3] Y. S. Tang and J. H. Saling, *Radioactive waste management*. CRC Press, 1990.

[4] R. A. Van Konynenburg, R. D. McCright, A. K. Roy, and D. A. Jones, "Engineered Materials Characterization Report for the Yucca Mountain Site Characterization Project Volume 1: Introduction, History, and Current Candidates," in *Nuclear Waste Packaging Focus '91 Conference*, 1991, p. 91.

[5] W. M. Miller, N. Chapman, I. McKinley, R. Alexander, and J. A. T. Smellie, *Natural analogue studies in the geological disposal of radioactive wastes*. Amsterdam: Elsevier, 1994.

[6] L. Werme, P. Sellin, and N. Kjellbert, "Copper canisters for nuclear high level waste disposal . Corrosion aspects," 1992.

[7] J. Robertson, "Diamond-like amorphous carbon," *Mater. Sci. Eng. R Reports*, vol. 37, pp. 129–281, 2002.

[8] M. Inagaki and F. Kang, *Materials Science and Engineering of Carbon: Fundamentals*. Elsevier, 2014.

[9] H. O. Pierson, *Handbook of carbon, graphite, diamonds and fullerenes: processing, properties and applications*. New Jersey: Noyes Publications, 1993.

[10] P. J. F. Harris, "New Perspectives on the Structure of Graphitic Carbons," *Crit. Rev. Solid State Mater. Sci.*, vol. 30, pp. 235–253, 2005.

[11] P. J. F. Harris, "Structure of non-graphitising carbons," *Int. Mater. Rev.*, vol. 42, pp. 206–218, 1997.

[12] P. J. F. Harris, "Fullerene-related structure of commercial glassy carbons," *Philos. Mag.*, vol. 84, pp. 3159–3167, 2004.

[13] G. M. Jenkins, K. Kawamura, and L. Ban, "Formation and steructure of polymeric carbons," *Proceeding R. Soc. London A*, vol. 327, pp. 501–517, 1972.

[14] G. M. Jenkins and K. Kawamura, *Polymeric carbons-carbon fibre, glass and char*. Cambridge: Cambridge University Press, 1976.

[15] P. J. F. Harris, "Fullerene-like models for microporous carbon," *J. Mater. Sci.*, pp. 565–577, 2013.

[16] "HTW-Germany Glassy Carbon," 2015. [Online]. Available: http://www.htw-gmbh.de/technology.php5?lang=en&nav0=2. [Accessed: 25-Aug-2015].

[17] D. F. Langa, N.G. van der Berg, E. Friedland, J.B. Malherbe, A.J. Botha, P. Chakraborty, E. Wendler and W. Wesch, "Heat treatment of glassy carbon implanted with cesium at room and high temperatures," *Nucl. Instruments*

Methods Phys. Res. Sect. B Beam Interact. with Mater. Atoms, vol. 273, pp. 68–71, 2012.

[18] O. Koskelo, U. Koster, I. Riihimaki, and J. Raisanen, “Migration kinetics of ion-implanted beryllium in glassy carbon,” *Diam. Relat. Mater.*, vol. 17, pp. 1991–1993, 2008.

[19] F. Chamssedine, T. Sauvage, S. Peuget, T. Fares, and G. Martin, “Helium diffusion coefficient measurements in R7T7 nuclear glass by He-3(d,alpha)H-1 nuclear reaction analysis,” *J. Nucl. Mater.*, vol. 400, pp. 175–181, 2010.

CHAPTER 2

DIFFUSION

From the theory of heat it is well known that atoms in a crystal oscillate around their equilibrium positions. If these oscillations are large enough to overcome the potential barrier between an atom and its neighbours, it can change lattice sites. It is this movement of atoms from one site to another that gives rise to diffusion in solids. Diffusion is the process whereby atoms or molecules are transported from a region of higher concentration to a region of lower concentration in a system, which can be gaseous, liquid or solid. Diffusion increases with temperature and in solids can be enhanced by irradiation. Changes in the arrangement of atoms or molecules in solids and the subsequent changes to the physical and mechanical properties occur by diffusion. Inhomogeneous materials can become homogeneous by diffusion. For diffusion to occur, the temperature should be high enough to overcome the energy barriers to atomic motion. Hence, any real understanding of phase change, homogenization, etc., must be based on the knowledge of diffusion.

2.1 MATHEMATICAL BASIC OF DIFFUSION

If an inhomogeneous single phase alloy is annealed, matter will flow in a manner which decreases the concentration gradients. Fick's first law in equation (2.1) is used in steady state diffusion, i.e., when the concentration within the diffusion volume does not change with respect to time. Microscopically it connects the diffusion coefficient D and the concentration gradient ϕ to the diffusion flux J. If the x-axis is taken parallel to the concentration gradient of a component, the flux of that component can be described in differential form by the equation [1]

$$J = -D\frac{\partial \phi}{\partial x} \tag{2.1}$$

This equation fits the empirical fact that the flux goes to zero as the specimen become homogeneous, that is, when the specimen reaches equilibrium. Although it need not have been the case, experimental data shows that D, or equivalently the ratio of $-J$ to the concentration

gradient, is independent of the magnitude of the gradient. In three dimensional vector notations, the general statement of Fick's first law is

$$J = -D\nabla\phi \tag{2.2}$$

The most common diffusion process in solids generally is in a non-steady state condition when the concentrations within the diffusion volume changes with time but particles are neither created nor destroyed. Thus, we have the continuity equation [She89]

$$\frac{\partial\phi}{\partial t} = -\frac{\partial J}{\partial x} \tag{2.3}$$

For linear flow and constant D, implying that D is not a function of position, this continually changing state diffusion is described by Fick's second law, which can be written by combining equations (2.1) and (2.3)

$$\frac{\partial\phi}{\partial t} = D\frac{\partial^2\phi}{\partial x^2} \tag{2.4}$$

For the case of three-dimensional diffusion the Fick's second law is written as

$$\frac{\partial\phi}{\partial t} = D\nabla^2\phi \tag{2.5}$$

Finally if the diffusion coefficient is not a constant, but depends upon the coordinate and/or concentration, the Fick's second law looks like

$$\frac{\partial\phi}{\partial t} = \nabla\left(D\nabla\phi\right) \tag{2.6}$$

The solution of these differential equations depends strongly on the boundary conditions of an experiment. For a semi-infinite body, i.e. a body bounded at $x = 0$ and extended to $x = \infty$, the solution to the differential equation (2.4) can be analytically found to be [2]

$$\phi(x,t)=\frac{1}{2\sqrt{\pi Dt}}\int_0^\infty \phi(\xi,0)\left[\exp\left(-\frac{(\xi-x)^2}{4Dt}\right)-\exp\left(-\frac{(\xi+x)^2}{4Dt}\right)\right]d\xi \qquad (2.7)$$

where $\phi(\xi,0)$ is the initial profile of the diffusing atom.

The diffusion coefficient at different temperatures is often found to be well predicted by

$$D = D_0 exp\left(-\frac{E_A}{RT}\right) \qquad (2.8)$$

where D is the diffusion coefficient, D_o is the maximum diffusion coefficient (at infinite temperature) also named the pre-exponential factor, E_A is the activation energy for diffusion, T is the absolute temperature and R is the gas constant. It can also be observed that there exists a linear proportional relation between lnD and $1/T$. Thus by plotting and considering intercepts, values of E_A and D_o can be determined experimentally.

Several methods have been used to obtain the general solution of a diffusion for different initial and boundary conditions. To solve the diffusion coefficient for the Fickian diffusion, the solution to the Fick diffusion equation (2.4) was derived for an initial Gaussian implanted profile with projected range R_p and range straggling ΔR_p, i.e.

$$\emptyset\ (\xi, 0) = \mathrm{A_o exp}\left[-\frac{(\xi - \mathrm{R_p})^2}{2\Delta \mathrm{R_p^2}}\right] \qquad (2.9)$$

where ξ is the depth below the surface. The solution is given by [3]:

$$\phi(x,t) =$$

$$\frac{A_0 \cdot \Delta R_p}{2\sqrt{2Dt + \Delta R_p{}^2}} e^{\left(-\frac{(x-R_p)^2}{4Dt+2\Delta R_p^2}\right)} \left[1 + erf\left(\frac{2DtR_p + x\Delta R_p^2}{\Delta R_p \sqrt{2(2Dt)^2 + 4Dt\Delta R_p^2}} \right) - ke^{\left(-\frac{xR_p}{Dt+\Delta R_p^2/2}\right)} \left\{ 1 + erf\left(\frac{2DtR_p - x\Delta R_p^2}{\Delta R_p \sqrt{2(2Dt)^2 + 4Dt\Delta R_p^2}} \right) \right\} \right] \tag{2.10}$$

and

$$k = 1 - \left[\frac{2N_0}{A_0} \frac{\sqrt{2Dt + \Delta R_p{}^2}}{\cdot \Delta R_p} \exp\left(\frac{R_p^2}{4Dt + 2\Delta R_p^2} \right) \Big/ \left\{ 1 + erf\left(\frac{R_p \sqrt{Dt}}{\Delta R_p \sqrt{2Dt + \Delta R_p^2}} \right) \right\} \right] \tag{2.11}$$

Where the two limiting cases for the parameter *k*, viz. $k = 1$ represents in the case of a perfect sink at the surface of the substrate, and $k = -1$ represents in the case of a perfect reflecting surface.

2.2 MECHANISMS OF DIFFUSION

All atoms in a perfect crystal are at specific atomic sites. In real crystals, however, given atomic sites may not be occupied, i.e. there may be a *vacancy*. On the other hand, impurity atoms, small or relatively large, may either occupy a non-regular atomic site (an *interstitial impurity*) or a normal atomic site in the parent lattice (a *substitutional impurity*) [4]. It is well know from the theory of heat that atoms in a crystal oscillate around their equilibrium positions. With sufficient energy to break the bonds with its neighbours (activation energy), these

oscillations become large enough to allow an atom to change sites. It is these jumps from one site to another which give rise to diffusion in solids, and it is vital to understand the various mechanisms of diffusion. There are several factors that affect diffusion such as the diffusing species, the microstructure of the substrate, chemical reactions between the substrate atoms and the diffusing species, etc. A few possible main mechanisms for atomic diffusion are discussed in this section [5].

2.2.1 INTERSTITIAL MECHANISM

A small atom that occupy interstitial space is said to move by the interstitial mechanism when it passes from one interstitial site to one of its nearest-neighbour interstitial sites without permanently displacing any of the matrix atoms, as illustrated in figure 2.1. The small atom in an interstitial site can move through the lattice much more rapidly than substititional atoms since it does not require the presence of a vacancy [6]. Before the interstitial atom can jump to the nearest-neighbour site, the matrix atoms must move apart enough to let it through. Thus an appreciable local distortion of the lattice must occur before the jump can occur. It is this distortion which constitutes the barrier to an interstitial atom changing sites [5]. The interstitial mechanism described here operates in alloys where the solute dissolves interstitially, e.g. carbon in iron, hydrogen in platinum and copper in silicon. In addition it can occur in substitutional alloys. For example, in radiation damage studies energetic bombarding particles can knock out atoms in normal lattice sites into interstitial positions to form what are called self-interstitials. These diffuse quite easily, once formed [2].

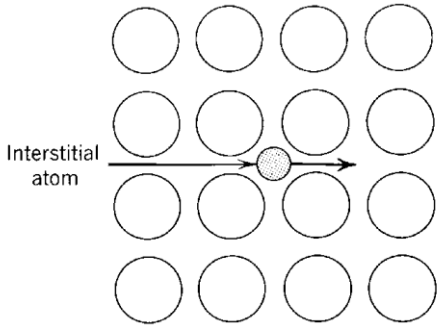

Figure 2.1 Schematic representation of interstitial diffusion mechanism. Taken from [6].

2.2.2 VACANCY MECHANISM

In all crystals some of the lattice sites are unoccupied. These unoccupied sites are called vacancies and they are present in pure metals and alloys at all temperatures [1]. If one of the atoms on an adjacent site jumps into the vacancy, the atom is said to have diffused by a vacancy mechanism. This is illustrated schematically in figure 2.2 and it is noted that the atoms move in the direction opposite to the vacancy. The distortional energy put into the lattice in moving an atom into an adjacent vacancy (vacancy mechanism) is small as compared to that for the interstitial mechanism. Thus because of the low distortional energy required atomic diffusion into vacancies has been found to be the most dominant compared to other diffusion mechanisms at high temperatures when there are many defects [5].

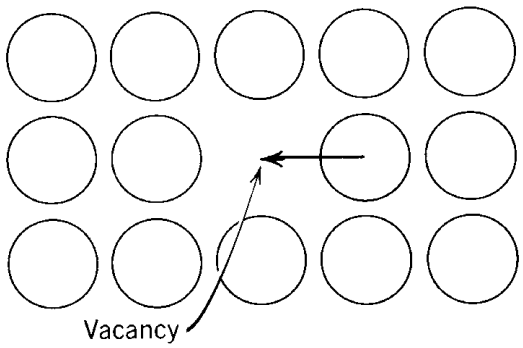

Figure 2.2 Schematic representation of vacancy diffusion mechanism. Taken from [6].

2.2.3 INTERSTITIALCY MECHANISM

If a relatively large atom occupies an interstitial position, it will produce large distortion if it jumps from one interstitial site to a neighbouring interstitial site. This would make the interstitial mechanism not probable, thus the interstitial atom may move by another mechanism known as interstitialcy mechanism. In the interstitialcy mechanism an interstitial atom pushes one of its neighbours on a normal lattice site into another interstitial position and itself occupies the lattice site of the displaced atom. This mechanism is illustrated schematically in figure 2.3.

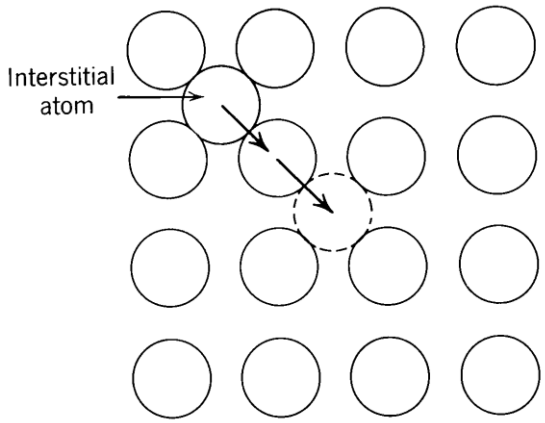

Figure 2.3 Schematic representation of interstitialcy diffusion mechanism. Taken from [6].

2.2.4 FACTORS THAT INFLUENCE DIFFUSION

Ease of the diffusion process is characterized by the parameter D, the diffusion coefficient. The value of the diffusion coefficient for a system depends on several factors, viz., diffusing species, temperature, lattice structure and presence of defects. If the *diffusing species* is able to occupy interstitial sites, then it can easily diffuse through the parent matrix. On the other hand if the size of substitutional species is smaller or almost equal to that of parent size, substitutional diffusion would be easier. Thus the size of diffusing species will have a great influence on the diffusion coefficient of the system. *Temperature* has a great influence on the diffusion coefficient and the diffusion rate. Neighbouring atoms that need to move to let the diffusing atoms pass create a barrier to diffusion. Thus, atomic vibrations created by temperature assist diffusion. Diffusion is faster in open *lattice structure* or in in open directions than closed directions. *Presence of defects* like dislocations and grain boundaries, act as short-circuit paths for diffusing species, where the activation energy is diffusion is less. Thus the presence of defects enhances the diffusion coefficient of diffusing species [5][7].

2.3 MEASUREMENT OF DIFFUSION COEFFICIENTS

Methods for the measurement of diffusion coefficients can be grouped into two major categories, viz. direct methods which are based on Fick's law and indirect methods which are not based directly on Fick's laws. Some of these methods are discussed by [8].

For this thesis, the Rutherford Backscattering Spectrometry (RBS) was used and based on a high energy beam of α-particles which are preferentially scattered by heavy ions in the sample. The energy spectrum of scattered α-particles can be used to determine the concentration depth distribution of scattering nuclei. This technique is mainly suitable for detecting heavy elements in a matrix of substantially low atomic weight. Due to the energy straggling of the incident beam the profile depth is limited to less than few μm. This method is discussed in detail in chapter 4.

2.3.1 DETERMINING DIFFUSION COEFFICIENTS

For the concentration profiles that approach a Gaussian shape, the values of the diffusion coefficients *D* can be obtained from the measurements of the profiles when the initial profile $\phi(\xi,0)$ in equation 2.7 is approximated by [9]

$$\phi_0(x) = \frac{K}{2\sqrt{\pi D t_0}} \exp\left(\frac{-x^2}{4Dt_0}\right) \tag{2.9}$$

where *K* and t_0 are adjustable constants. Then equation 2.7 reduces to

$$\phi(x,t) = \frac{K}{2\sqrt{\pi D(t+t_0)}} \exp\left(\frac{-x^2}{4D(t+t_0)}\right) \tag{2.10}$$

Defining the profile width W(t) as the full with at half maximum (*FWHM*) such that

$$\phi(W,t) = \frac{1}{2}\phi(0,t) \tag{2.11}$$

one has from equation (2.10)

$$[W(t)]^2 = 4Dt\ln(2) + [W(0)]^2 \tag{2.12}$$

Thus the slope of the plot of $[W(t)]^2$ versus the annealing time *t* at constant temperature yields the diffusion coefficient *D*. To completely describe diffusion, the maximum diffusion coefficient at infinite temperature (or pre-exponential factor) D_o and the activation energy for diffusion E_A, are found by establishing the diffusion coefficients at three or more difference temperatures and using them to solve the unknowns (i.e. D_o and E_A,) in the Arrhenius equation (2.8) [10].

2.4 DIFFUSION IN DISORDERED MATERIALSS

In this thesis glassy carbon is used as a substrate to study the diffusion of silver and cesium. Glassy carbon, which was briefly discussed in chapter 1, is a particularly interesting form of disordered carbon made from a resin that is carbonized at very low heating rate [11]. As was already indicated in Chapter 1 glassy carbon can be considered to be a predominantly amorphous material.

There are different classes of disordered materials, and the diffusion process differs in each class. Amorphous materials that are formed by quenching from a liquid phase are called glasses. These are materials that can be cooled into a glassy state from the liquid because their molecular motion is slow. Amorphous materials are usually not the lowest free energy configuration, but their random arrangement persists because the atoms do not have enough mobility to rearrange into a lower free energy crystalline array. There are network of glass formers such as silica, and there are molecular glass formers, such as Sasol and glycerol. The glassy phase of silica has dangling bonds that promote diffusion [6].

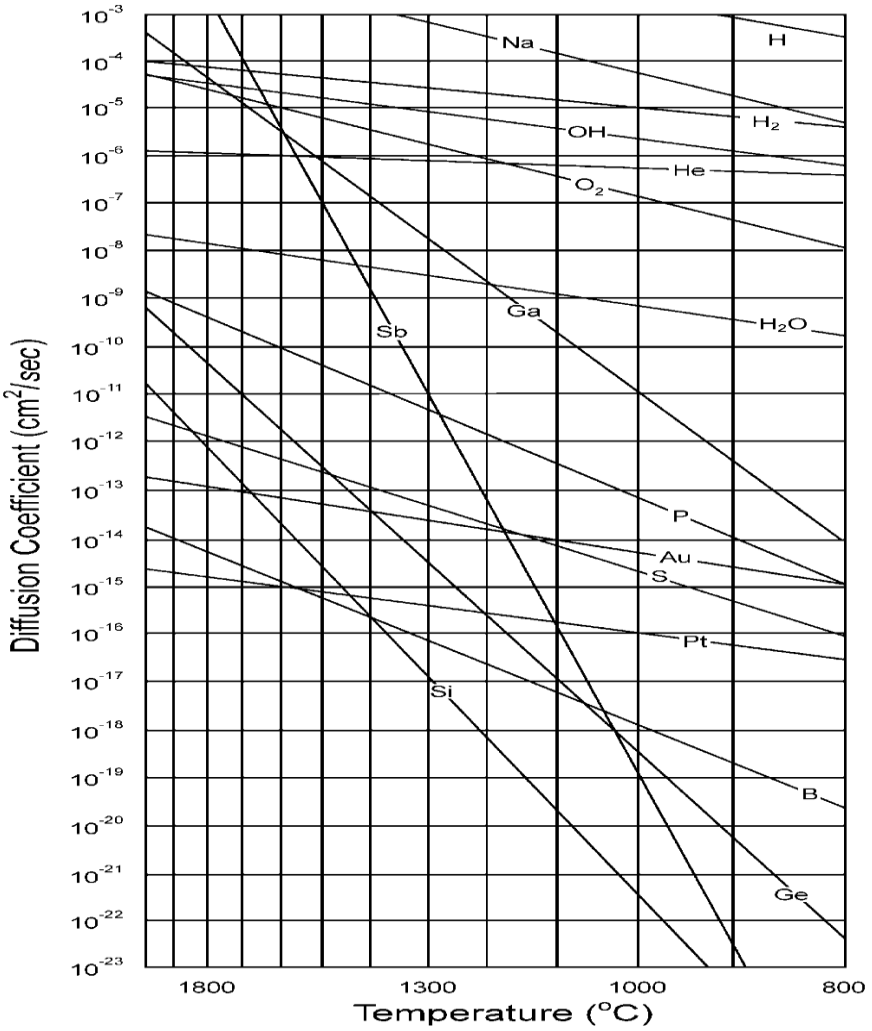

Figure 2.4 Diffusion coefficients of various elements in silica. Taken from [6].

Data for the diffusion coefficients of various elements in silica are presented on an Arrhenius plot if figure 2.4. Atoms that occupy and move through the open space between the silicon and oxygen atoms of the matrix are called interstitial atoms. They diffuse rapidly, and are at the top of the chat. When the diffusing atoms replace the silicon or oxygen atoms in network matrix of the silica, they are called substitutional atoms. They diffuse more slowly and are at the bottom of the chart.

2.5 REFERENCES

[1] D. Gupta, Ed., *Diffusion processes in advanced technological materials*. New York: Willian Andrew, Inc, 2005.

[2] R. M. Barrer, *Diffusion in and through solids*. Cambridge: Cambridge University Press, 1941.

[3] J. B. Malherbe, P.A. Selyshchev, O.S. Odutemowo, C.C. Theron, E.G. Njoroge, D.F. Langa, T.T. Hlatshwayo, "Diffusion of a mono-energetic implanted species with a Gaussian profile," *Nucl. Instruments Methods Phys. Res. Sect. B Beam Interact. with Mater. Atoms*, pp. 708–713, 2017.

[4] M. N. Rudden and J. Wilson, *Elements of solid state physics*, 2nd ed. Chichester: John Wiley and Sons Ltd, 1993.

[5] P. Shewmon, "Diffusion in solids," *Miner. Met. Mater. Soc. Diffus. Solids. Second Ed. Cover. States), 1989*, p. 246, 1989.

[6] K. A. Jackson, *Kinetic Processes: Crystal Growth, Diffusion, and Phase Transformations in Materials*. Weinheim: John Wiley & Sons, 2004.

[7] L. G. Harrison, "Influence of dislocations on diffusion kinetics in solids with particular reference to the alkali halides," *Trans. Faraday Soc.*, vol. 57, pp. 1191–1199, 1961.

[8] P. Heitjans and J. Kärger, Eds., *Diffusion in condensed matter: methods, materials, models*. Heidelberg: Springer Science & Business Media, 2005.

[9] S. M. Myers, S. T. Picraux, and T. S. Prevender, "Study of Cu diffusion in Be using ion backscattering," *Phys. Rev. B*, vol. 9, p. 3953, 1974.

[10] T. T. Hlatshwayo, "Diffusion of silver in 6H-SiC," University of Pretoria, PhD thesis, 2010.

[11] S. Yamada and H. Sato, “Some physical properties of glassy carbon,” *Nature*, vol. 193, pp. 261–262, 1962.

CHAPTER 3

ION IMPLANTATION

Ion implantation is a low temperature technique of introduction of impurities (dopants) into the target material. The dopant atoms are volatilized, ionized, accelerated, separated by the mass-to-charge ratios, and directed to the target. The ions enter the target, collide with the host atoms, lose energy, and finally come to rest at some depth within the solid. The ions slow down gradually along their path by the interaction with electrons, and they can also be scattered by making direct collisions with the nuclei of the atoms in the substrate. The strength of these two types of interaction depends on the type of incident ion, on its accelerating energy and on the substrate material [1]. In this thesis, the ion implantation was used to investigate the migration kinematics of silver and cesium to the surface of glassy carbon.

3.1 ION STOPPING POWER

Since the initial ion energy, typically several tens of keV, is much higher than lattice binding energies, the ion scattering process can be simulated based on elastic collisions between pairs of nuclei while ignoring the relatively week lattice forces. A second component of scattering comes from inelastic collisions with electron in the target. The total stopping power S of the target, defined by the energy loss (E) per unit length (x) of the ion, is the sum of these two terms:

$$S = \frac{dE}{dx} = \left(\frac{dE}{dx}\right)_{nuclear} + \left(\frac{dE}{dx}\right)_{electronic} \qquad (3.1)$$

Figure 3.1 shows the relative distribution to S of each of the terms over a wide energy range. The nuclear stopping dominates at low energies and the electronic stopping dominates at higher energies. Not shown in Figure 3.1, is the fact that at very low energies, i.e. when the ion energy is in the range of atomic binding energies, electronic stopping dominates. Because of the complexity of this process we shall not discuss this any further. Energies typical for ion implantation fall on the far left of the figure, a region dominated by nuclear stopping.

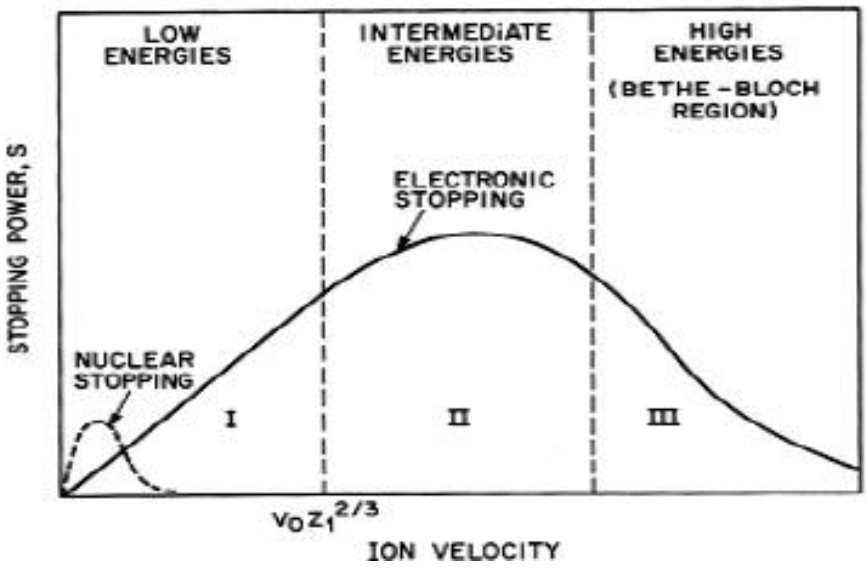

Figure 3.1 Nuclear and electronic components of the ion stopping power as a function of ion velocity. Taken from [2].

3.1.1 NUCLEAR STOPPING

Nuclear stopping is caused by a collision between two atoms, and can be described by classical kinematics. If the atoms were bare nuclei, the actual atomic potential, known as the Coulomb potential, at some radius *r* between them can be given as:

$$V_C(r) = \frac{e^2 z_1 z_2}{4\pi\varepsilon_0 r} \tag{3.2}$$

where z_1 and z_2 are the atomic number of the implanted and the target atoms, respectively, *e* is the electron charge, ε_0 is the electric permittivity of free space and *r* is the interatomic distance. Equation 3.2 show that the potential decreases rapidly with increasing atomic separation. This situation is not changed when screening functions are introduced and the entire collision sequence associated with ion implantation over the energy range of present interest in the study can be described in terms of successive binary collisions. In reality, the nuclear charges are screened by both sets of the electrons. Therefore, a screening function $f_s(r)$ is included, giving:

$$V(r) = V_C(r) f_s\left(\frac{r}{a}\right) \tag{3.3}$$

where $V(r)$ is the screened potential, $V_C(r)$ is the unscreened potential and a is the screening parameter. Thus from equation 3.3, the screening function is define as the ratio of actual atomic potential at some radius to the potential caused by unscreened nucleus. The screening parameter is an important concept. It moderates the effect of the nuclear positive charge on the electrons because the inner electrons shield some of the nuclear charge [3].

The amount of energy that can be transferred in an elastic collision is dependent on the masses of the particle and the impact parameter. Since in the present study we are working with energies greater than 1 keV where many body effects can be neglected, the binary collision approximation (BCA) methods can be used. The BCA treats the passage of an ion through matter as a series of discrete collision between two atoms. The elastic scattering configuration of a collision between an energetic ion and the stationary target atom is shown in figure 3.2. The incident ion (mass M_1) moves with an initial energy of E_0 towards the stationary target atom (mass M_2), with some perpendicular distance between the line of center of the particles, p, called the impact parameter. The incident ion will be scattered at an angle θ reducing its own energy to E_1 and energy will be imparted to the target ion causing it to recoil with energy E_2 at an angle ϕ [4][5].

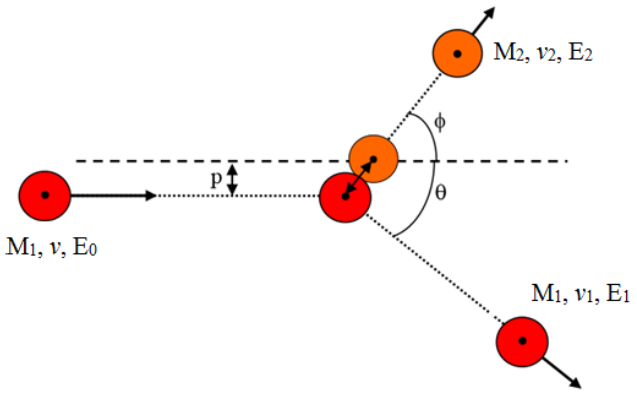

Figure 3.2 The elastic scattering configuration showing a collision between an energetic ion of mass M_1 with an initial energy of E_0 and the stationary target atom of mass M_2.

Because there are no external constraints total energy and momentum are conserved. As a consequence of conserving energy and momentum, and eliminating the projectile scattering angle (θ), the kinetic energy E_2 transferred to the target atoms is calculated to be

$$E_2 = E_0 \frac{4M_1M_2}{(M_1+M_2)^2} cos^2 \emptyset \qquad (3.4)$$

The energy transferred is found to be a function of the target recoil angle ϕ, projectile energy E_0, the mass of the projectile M_1, and the mass of the target M_2 [6]. In the center of coordinates system, the energy transferred is

$$E_2 = E_0 \frac{4M_1M_2}{(M_1+M_2)^2} sin^2 \left(\frac{\emptyset_c}{2}\right) \qquad (3.5)$$

where ϕ_c in the recoiling energy in the center of mass coordinate system [7]. The angles depend on the mass and on the impact parameter p. The maximum energy transferred is when $p = 0$ and $\phi = 0$, in which case equation 3.4 reduces to

$$E_2 = E_0 \frac{4M_1M_2}{(M_1+M_2)^2} \qquad (3.6)$$

The energy transferred will decrease with increasing impact parameter and the average energy transferred is half that of its maximum value. The path of each ion depends on the individual collisions that it encounters and hence the final path of an implanted ion will be subjected to statistical variations [4]. The rate of energy loss due to the number of nuclear collisions per unit length can be calculated by integrating the energy loss multiplied by the probability of a collision occurring. If the maximum possible energy transfer in a collision is E_{max} and there are N target atoms per unit volume, then nuclear stopping power is given by

$$S_n = \left(\frac{dE}{dx}\right)_{nuclear} = N \int_0^\infty E d\sigma \qquad (3.7)$$

where $d\sigma$ is the differential cross section. During the elastic collision of the incident ion with the target, energy is transferred to the target atom. It is subsequently recoiled away from its lattice site, thus creating a defects, i.e. radiation damage [8][9].

3.1.2 ELECTRONIC STOPPING

The electron stopping is caused by the interaction between the incoming ions and the electrons in the target. The interactions between a charged particle and the bound electrons are very complex and therefore rather difficult to describe theoretically. That is to say, electrons in the target can both collide in-elastically with a projectile and be excited or ionized, and the same processes can take place for the electrons of the energetic ion. The energy loss by incident ions is dissipated through the electron cloud into the thermal vibration of the target. The possible origins of the electron energy loss are [3]:

Direct energy transfer to target electrons, mainly due to electron-electron collisions.

i. Excitation or ionization of target atoms.
ii. Excitation of band- or conduction-electrons, i.e. weakly bound or unlocalized target electrons.
iii. Excitation, ionization or electron-capture of the projectile itself.

Lindhard's theory [10][11] makes the assumption that the interaction between the ion and the substrate electrons can be approximated by the interaction of the ion with a free electron gas. The initial electron gas is of uniform density. The interaction of the charged particle is a small perturbation of the electron gas and all particles velocities are non-relativistic. The electron stopping of a charged particle in the local density approximation may be stated as

$$S_e = \int I(v, \rho) Z_1^2 \rho dV \qquad (3.8)$$

where S_e is the electron stopping cross section; I is the stopping interaction function of a particle of unit charge with velocity v, Z_1 is the charge of the particle, ρ is the electron density of the target, and the integral is performed over each volume element dV of the target [3][12].

The electron energy loss of the ions has a peak at intermediate energies (Fig. 3.1). The rate of inelastic energy loss is dependent on the ion energy, and can be considered to consist of two different velocity regimes. For low velocities (Region I) the electron stopping is found to be proportional to $E^{0.5}$ [8] and the incident ions is assumed to retain all its electrons. Since the transferred energy from the projectile to the target electron is proportional to the projectile

velocity, the electron stopping power is proportional to the projectile velocity and can be approximated as [10][11]:

$$S_e = \left[\frac{2q^2 a_0 Z_1^{7/6} Z_2 N}{\epsilon_0 \left(Z_1^{2/3} + Z_2^{2/3}\right)^{3/2}}\right] \frac{v}{v_0} \qquad (3.9)$$

where Z_1 and Z_2 are the atomic numbers of the incident ion and the target respectively, a_0 and v_0 are the Bohr radius and velocity, and N is the target wafer atomic density.

The maximum of the stopping curve lies in the general vicinity of the Thomas-Fermi velocity (Region II) given by $Z_1^{2/3} v_0$ (v_0 is the Bohr velocity and, $v_0 = e^2/\hbar$ where e and $\hbar$ are the electron charge and Planck's constant respectively). At relativistically high projectile velocities, in the Bethe-Bloch formalism (Region III), the electronic stopping decreases as the projectile is stripped of all its valence electrons, becomes smaller and virtually sees neither the target nuclei nor electrons [13][14].

There are a number of models describing the inelastic energy loss. Bohr used classical mechanics to describe the interaction of a charged particle with the electron in the target [15][16]. The energy loss under these circumstances is based on the classical calculation of the momentum and energy transferred to an electron by the ion collision. The ionization energy required to separate the electron from the atom has to be accounted for and therefore the scattering event becomes inelastic. Bohr showed that the rate of energy loss varies with the ion velocity. A number of approximations were developed to take into account possible energetic states of an electron in the target and the average population of these states. The work of Bethe [17] and Bloch [18] produced a quantum mechanical approach to the inelastic energy loss. The Bethe – Bloch formula only describes the energy loss well at energies beyond the maximum in the dE/dx curve to near relativistic velocities. In this region there is an increase in the inelastic stopping power for a decrease in velocity.

For lower energies, two models that better describe the inelastic energy loss are that of Firsov [19]. Firsov's expression is based on a simple geometric model of momentum exchange between the projectile and target atom during the interpenetration of the electron clouds surrounding the two colliding atoms. Another way to look at the inelastic energy loss is the

model of Linhard and Scharff [11]. The model assumes that the free electron gas consists of electrons at zero temperature on a fixed uniform positive background with overall charge neutrality. A fast charge particle entering the system brings about a polarization of the medium which causes energy absorption.

3.2 RANGE DISTRIBUTION

The two key parameters defining the final implant profile are fluence Φ (usually given in atoms/cm^2) and energy E (in ke$V$). The fluence is related to the beam current I by the following formula:

$$\Phi = \frac{It}{q_i A} \tag{3.10}$$

where t denotes implantation time, A beam area and q_i is the charge per ion. When the ions enter the substrate they continuously loose energy and change direction by collisions with the target atoms. The total path length that each implanted ion come to rest at will vary. Knowledge of the stopping power allows the overall slowing down to be described in a quantitative way. It therefore enables calculation of the range. Rearranging the total stopping power in equation 3.1 and integrating from the maximum energy E_o (i.e. the implantation energy – the energy of the bombarding ions) to zero yields the total path length, $R(E)$, of the ion.

$$R(E) = \int_0^{E_o} \frac{dE}{\left(dE/dx\right)_n + \left(dE/dx\right)_e} \tag{3.11}$$

In theory, the final density of implants $n(x)$, irrespective of the species, is statistically distributed as a function of the depth x and may be roughly approximated by a Gaussian distribution [13][20][21] given by:

$$n(x) = \frac{\emptyset}{\Delta R_p \sqrt{2\pi}} . exp\left\{-\frac{\left(x-R_p\right)^2}{2.\Delta R_p^2}\right\} = n_0 . exp\left\{-\frac{\left(x-R_p\right)^2}{2.\Delta R_p^2}\right\} \tag{3.12}$$

where n_0 is the peak concentration. The other parameters used to define this distribution are the mean projected range R_p, the average deviation from the mean projected range called the projected range straggling σ_p (or ΔR_p) and the total number of ions per unit area ϕ. These statistical parameters are illustrated schematically in figure 3.3. It is worth noting from this figure that the average total path length called the range R, which comprises of both lateral and vertical motions, is longer than the projected range [22].

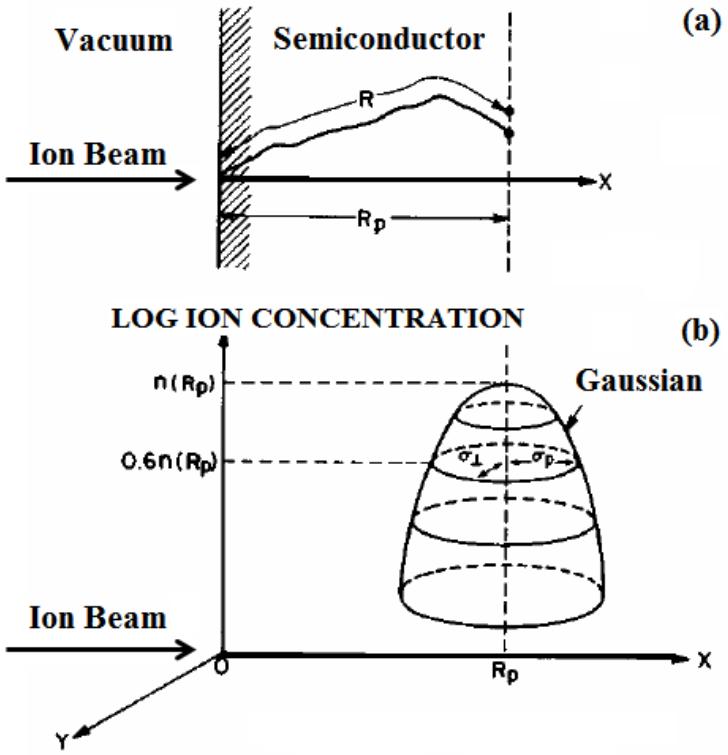

Figure 3.3 A distribution (depth and lateral) of the implant concentration with respect to the depth of the implanted material. Taken from [22].

Several different distributions have been employed to give a more accurate fit to the implanted ion distribution than a Gaussian. The most popular of these is the Pearson IV fit, though in this thesis we mostly used the Edgeworth expansion [23] and Gaussian expansion to fit the profile in our results. Figure 3.4 compares experimental boron profiles (dotted lines) implanted in silicon for energies between 30 keV and 800 keV under non-channelling conditions. The fitted distribution are shown with solid lines [22]. As the implantation energy is increased, the profiles become more negatively skewed and deviate more significantly from

a true Gaussian. The variation in the skewness is explained by increased electron stopping for faster moving ions in the pre-expected range (depth) region.

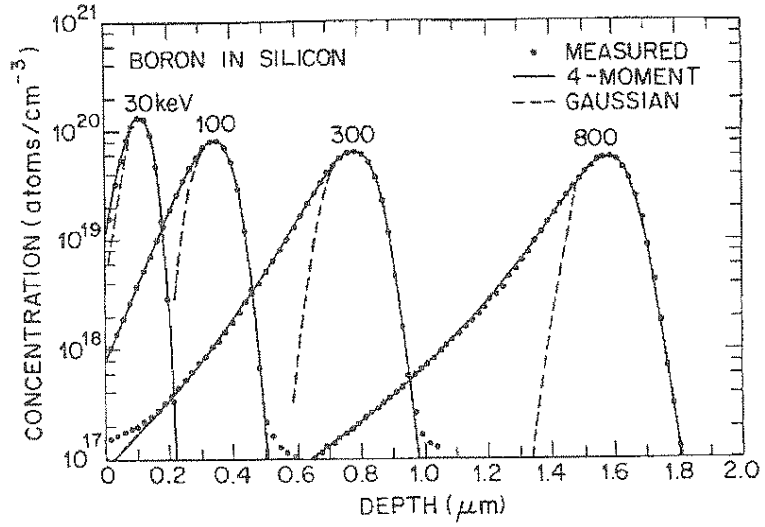

Figure 3.4 Boron implanted atoms distribution, comparing measured data points with four-moment (Pearson IV) and Gaussian fitted distribution. Taken from [22].

3.3 SIMULATION OF ION IMPLANTATION

Several computer codes have been developed to calculate parameters such as range and straggling of implanted ions. The Stopping and Range of Ions in Matter (SRIM) [24] is a group of programs which calculate the stopping and range of energetic ions into matter using a fit to a full quantum mechanical treatment of ion-atom collisions. The most comprehensive of these programs is the Transport of Ions in Matter (TRIM). It was developed for determining ion range and damage distributions as well as angular and energy distribution of backscattered and transmitted ions. This program provides particularly high computer efficiency, while still maintaining accuracy. This is obtained mainly by applying the analytic formula for determining nuclear scattering angles, and by suitably expanding the distance between collisions at high energies [3].

The TRIM/SRIM simulations code is widely used for simulating the effects of ion implantation and has been useful within this study to compare theory to the experimental depth profiles obtained from the Rutherford Backscattering (RBS) experiments. Because of the statistical nature of the paths of implanted ions simulations TRIM/SRIM uses Monte Carlo

methods and binary collision algorithm to calculate the ion trajectories of many implanted ions. As with other simulation programs, it consists of following a large number of individual ion or particle histories in a target. Each history begins with a given energy, position, and direction. The particle is assumed to change direction as a result of binary nuclear collision and move in straight free-flight-paths between collisions. The energy is reduced as a result of nuclear and electronic energy losses as described in sections 3.1.1 and 3.1.2. A history is terminated either when the energy drops below pre-specified value or when the particle's position is outside the target. The target is considered amorphous with atoms at random locations, and thus the directional properties of the crystal lattice are ignored. This simulation method is applicable to a wide range of incident energies from approximately 0.1 keV to several MeV. The lower limit is due to the inclusion of binary collisions only, while the upper limit results from the neglect of relativistic effects. Nuclear reactions are not included.

It will accept complex targets made of compound materials, and calculate the final 3D distribution of implanted ions and also all kinetic phenomenon associated with ion's energy loss: target damage, sputtering, ionization and phonon production. As an example, a simulation of the paths of twenty each implanted silver (Ag) and boron (B) atoms into glassy carbon with implant energy of 360 keV, are shown in figure 3.5 (a) and (b) respectively. Shallower implantation and smaller amount of straggling are seen with Ag compared to B. From equations 3.6, one would observe that larger mass of the implanted silver ions yields higher energy transferred to the target atoms. These later leads to higher stopping power by the target atoms, according to equation 3.7.

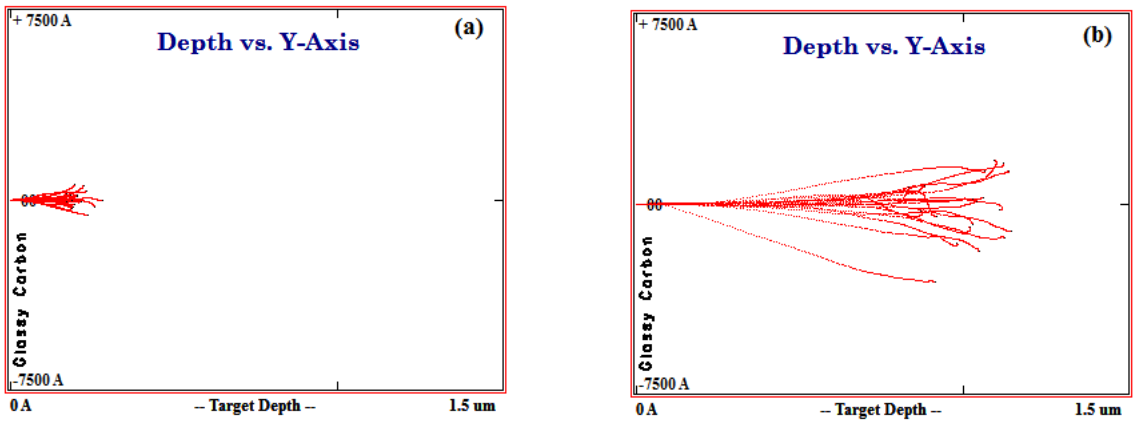

Figure 3.5 Results of TRIM simulation showing the trajectories of 20 (a) 360 keV Ag ions and (b) 360 keV B ions, implanted into glassy carbon. Taken from [24].

3.4 REFERENCES

[1] K. A. Jackson, *Kinetic Processes: Crystal Growth, Diffusion, and Phase Transformations in Materials*. Weinheim: John Wiley & Sons, 2004.

[2] B. Schmidt and K. Wetzig, *Ion beams in materials processing and analysis*. Heidelberg: Springe-Werlag Wien, 2012.

[3] J. F. Ziegler, J. P. Biersack, U. Littmark, and H. H. Anderson, *The stopping and ranges of ions in matter. Vol 1 ; The stopping and range of ions in solids, by J.F. Ziegler, J.P. Biersack and U. Littmark ... Vol 6 ; Handbook of range distributions for energetic ions in all elements, by U. Littmark and J.F. Ziegler. Vo*. New York: Pergamon, 1985.

[4] G. Carter and W. A. Grant, *Ion implantation of semiconductors*. New York: John Wiley and Sons, 1976.

[5] G. Dearnaley, *Ion implantation*, vol. 8. Amsterdam: North-Holland Publishing Company, 1973.

[6] W. M. Gibson, *The physics of nuclear reactions*. New York: Pergamon Press, 1980.

[7] J. F. Ziegler, Ed., *Ion Implantation Science and Technology 2e*, 2nd Ed. New York: Academic Press, Inc., 1988.

[8] P. D. Townsend, J. C. Kelly, and N. E. W. Hartley, *Ion implantation, sputtering and their applications*. New York: Academic Press, 1976.

[9] J. F. Ziegler, “Ion implantation physics,” in *Handbook of Ion Implantation*

Technology, vol. 1, J. F. Ziegler, Ed. Amsterdam: North-Holland: New York, 1992, pp. 1–68.

[10] J. Lindhard and M. Scharff, "Stopping Power of Heavier Substances," *Phys. Rev.*, vol. 85, pp. 1058–1059, 1952.

[11] J. Lindhard and M. Scharff, "Energy dissipation by ions in the keV region," *Phys. Rev.*, vol. 124, pp. 128–130, 1961.

[12] J. F. Ziegler, "The Stopping of Energetic Light Ions in Elemental Matter," *J.Appl.Phys/Rev.Appl.Phys.*, vol. 85, pp. 1249–1272, 1999.

[13] M. S. Dresselhaus and R. Kalish, *Ion implantation in diamond, graphite and related materials*, vol. 22. Heidelberg: Springer-Verlag Berlin, 1992.

[14] J. W. Mayer, L. Eriksson, and J. A. Davies, *Ion Implantation in Semiconductors*, vol. 3. New York: Academic Press, 1970.

[15] N. Bohr, "II. On the theory of the decrease of velocity of moving electrified particles on passing through matter," *London, Edinburgh, Dublin Philos. Mag. J. Sci.*, vol. 25, pp. 10–31, 1913.

[16] N. Bohr, "The penetration of atomic particles through matter," *Mat. Fys. Medd. Dan. Vid. Selsk.*, vol. 18, pp. 19–26, 1948.

[17] H. A. Bethe, "On the Stopping of Fast Particles and on the Creation of Positive Electrons," *Proc. R. Soc. A Math. Phys. Eng. Sci.*, vol. 146, pp. 83–112, 1934.

[18] F. Bloch, "Zur bremsung rasch bewegter teilchen beim durchgang durch

materie," *Ann. Phys.*, vol. 408, pp. 285–320, 1933.

[19] O. B. Firsov, "A qualitative interpretation of the mean electron excitation energy in atomic collisions," *Zhur. Eksptl'. i Teoret. Fiz.*, vol. 36, pp. 1517–1523, 1959.

[20] M. Nastasi, J. Mayer, and J. K. Hirvonen, *Ion-solid interactions: fundamentals and applications*. Cambridge: Cambridge University Press, 1996.

[21] J. S. Williams, "Materials modification with ion beams," *Reports Prog. Phys.*, vol. 49, pp. 491–587, 1986.

[22] P. K. Chu and J. F. Gibbons, "Ion Implantation," *E-learning City Univ. Hong Kong [Online]. Available http//personal. cityu. edu. hk/~ appkchu/AP4120/9. PDF [2009, May 20]*, 1976.

[23] F. Y. Edgeworth, "The Law of Error. Part I," *Trans. Cambridge Philos. Soc.*, vol. 20, p. 36, 1908.

[24] J. F. Ziegler, "The Stopping and Range of Ions in Matter (SRIM), 2013 software." 2013.

CHAPTER 4

ANALITICAL TECHNIQUES

4.1 SCANNING ELECTRON MICROSCOPY

The scanning electron microscope (SEM) is one of the most versatile instruments available for the examination and analysis of the topographical characteristics of solids objects. For the instrument, the area of the specimen to be examined or analysed is irradiated with finely focused electron beam which is scanned across this area. The basic components of the SEM are the lens system, the electron gun, the electron collector, visual and the cathode ray tube, and the electronics associated with them. The first commercial packaging of these components was made available in 1965. Though the earliest work describing the constructing of the SEM was in 1938, where scan coils were added to a transmission electron microscope (TEM). In so doing this produce what amounts to the first scanning transmission electron microscope (STEM). The function of the electron gun is to provide a stable source of electrons to form the electron beam. Different electron guns are used in the commercial SEMs which vary in the amount of current they can produce into a small spot, the stability of the emitted current, and the life-time of the source.

At the early stage of SEM construction, tungsten or LaB_6 thermionic emitters were used while some of the new SEMs use the cold, thermal or Schottky field emission electron gun. In the field emission electron gun, the cathode is usually in the form of a rod with a very sharp point at the end of the order of 100 nm diameter or less. Holding the cathode at negative potential compared to the anode, the electric field at the tip become strong (to magnitudes greater than 10^7 V/cm). As a result electrons are emitted and a cathode current density of between 1000 and 10^6 A/m^2 may be obtained. This give a far better brightness which is a hundred time than that of a thermionic source at the same voltage. The image quality at high magnification is largely depended on the brightness [1]. The strategy needed in selecting the optimum operating conditions of the SEM depend on understanding the following:

i. What happens when the beam of energetic electrons strikes the sample, and

ii. How the signal produced by the electron beam-sample interaction is converted into images.

Figure 4.1 shows the path followed by the beam of electrons produced from the electron gun till they strike the sample. Electrons are produced by the electron gun at the top of the column, accelerated down passing through a series of magnetic lenses and apertures to produce a focused beam of energetic electron which strikes the surface of the sample that is mounted in the chamber area. Both the column and the chamber are evacuated by a vacuum pump and the level of the vacuum normally depends on the design of the microscope. The position of the electron beam on the sample is controlled by the scan coils which allow the beam to be scanned over the surface of the sample. This beam scanning, as the name of the microscope suggest, enables information about a defined area of the sample to be collected. As a result of the electron-sample interaction, a number of ray particles are produced that are then detected by appropriate detectors. By detecting the appropriate ray particles the SEM is able provide information on the following:

i. Topography, which gives the arrangement of the natural and artificial physical features of the scanned surface area.

ii. Morphology, which gives information of the shape and size of the particles marking up the sample.

iii. Composition, which gives the elements, and compounds that the sample is composed of and their relative amounts.

iv. Crystallography, which gives the arrangement atoms in the sample.

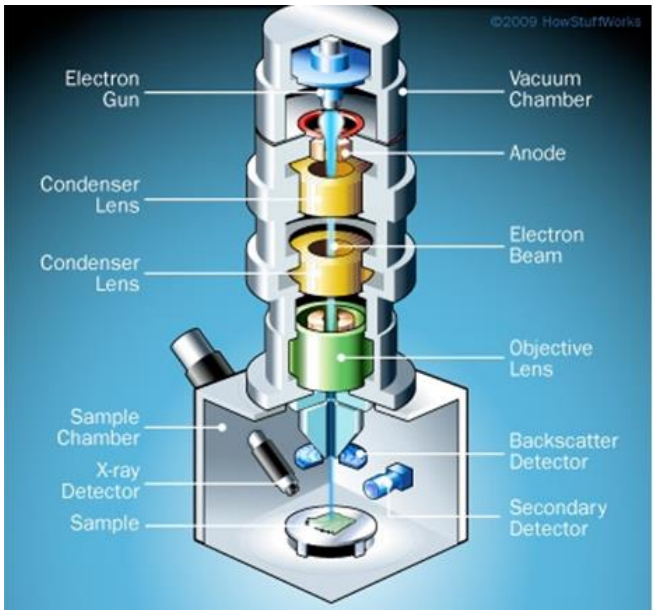

Figure 4.1 A representation of the key components of the SEM. Taken from [2]

Before we discuss how the signal produced by the electron beam-sample interaction are converted into images, we need to understand the general electron material interactions. The beam of energetic electron can interact with the coulomb (electric charge) field of both the specimen nucleus and electrons. These interactions are responsible for the production of the backscattered electrons (BSE), secondary electrons (SE), X-Rays, Auger electrons and catholuminescence, as shown in figure 4.2.

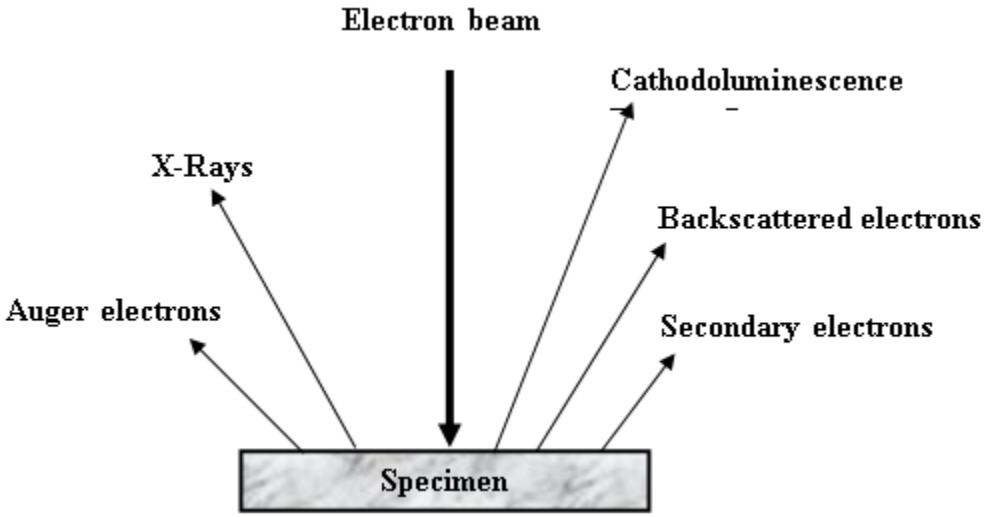

Figure 4.2 A schematic diagram showing the signals produced when a beam of energetic electrons interact with the sample

Figure 4.3 displays a cross section of the volume of primary excitation illustrating zones from which these signal may be detected [3]. For the purpose of this research our discussion will focus on the backscattered electrons, secondary electrons and in-lens secondary electrons. Backscattered electrons are the result of an elastic collision and scattering event between the incident electrons and target nuclei or electrons. These incident electrons can be scattered from deeper into the target material than the secondary electrons. The backscattered electrons helps to resolve topographical contrast and atomic number contrast. Inelastic events occur when an incident electron beam interact with the electric field of the target material electron. The result is the transfer of energy to the sample electron atom followed by the expulsion of electrons from that target atom as secondary electrons (SE). Secondary electrons detected by the secondary electron detector in a SEM have energies less than 50 eV. The low-energy secondary electrons will be accelerated to a sufficient energy to generate light in the scintillator.

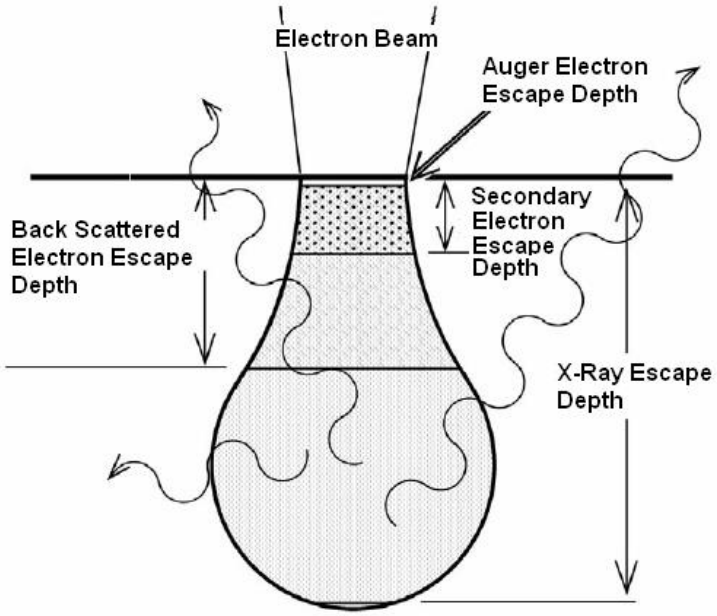

Figure 4.3 A schematic diagram showing the escape depth of different signals from the electron-sample interaction. Taken from [3].

The principle of the in-lens detection system in that the in-lens detector in placed on top of the final piece in the SEM along the path of the incident electron beam as shown in figure 4.4. The secondary electron detector is also shown in the figure positioned outside the lens system. The positioning of the secondary electron detector favours both SE1 and SE2 electrons (see Figure 4.4 for clarification of the notation) but the in-lens system favours mostly SE1s. The SE2 originate from inner parts of the sample while the SE1 originates from the sample

surface and the incident beam centre. The SE1 can be detected very efficiently by the in-lens detector. As a result, high contrast images are easily achieved, even at lower escape depths and energies [4]. Secondary electrons have a fairly constant emission level as one moves away from the very light elements. However at very low accelerating voltages secondary electron emission varies considerably. The maximum yield of secondary electrons falls between two critical voltages, which vary for each element or compound [5]. Backscatter signal levels continue to increase with atomic number. With smoother specimen surfaces different elements give rise to images exhibiting "atomic number contrast", i.e. the denser the element the brighter the image.

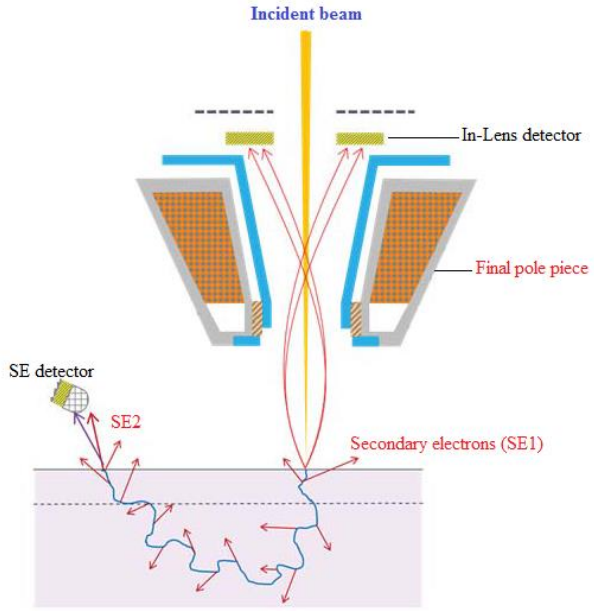

Figure 4.4 Principle of the secondary electron detection with both a secondary electron detector and an in-lens detector. Taken from [4].

Figures 4.5 shows the contrast difference between secondary (a) and in-lens (b) detector images which were collected from a palladium on carbon catalyst. In figure 4.5 (a) the image was taken at 20 kV and shows lesser degree of detail. This is mainly due blurring effect of SE2 electrons since they come from inner parts of the material. In figure 4.5 (b), the image was taken at low voltage of 1.6 kV. The image is much sharper and more detailed.

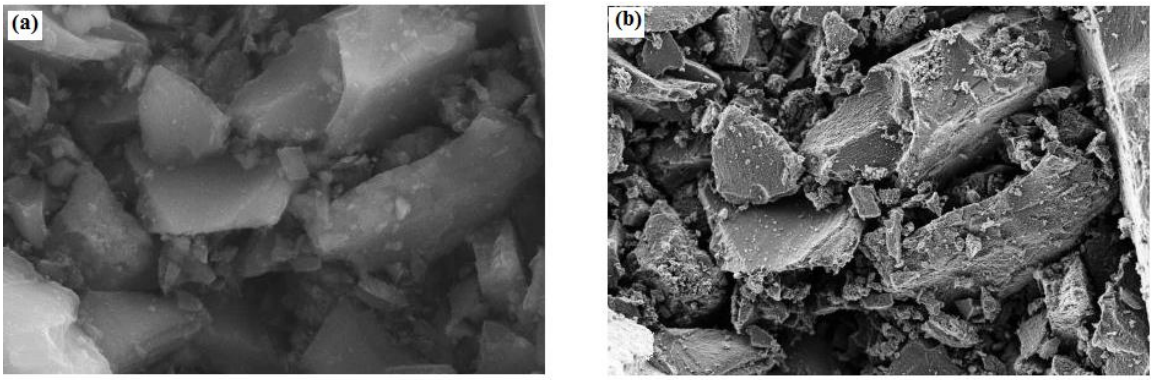

Figure 4.5 Palladium on carbon catalyst. (a) Secondary electron (SE2) image taken at 20 kV; (b) secondary electron (SE1) taken at 1.6 kV image using the in-lens detector. Taken from [4]

The interaction volume of the incident electron beam within the target is influenced by the following parameters:

(i) **Beam energy**: The size of the interaction volume is a strong function of the energy with which the beam of incident electrons interact with the target. Firstly, the cross section for elastic scattering is inversely proportional to the square of the energy as shown in equation, $Q \sim 1/E^2$. As the energy increase the elastic cross section becomes smaller. Thus, the electrons penetrate more deeply into the solid before the effect of multiple elastic scattering causes some of the electrons to move back to the surface. Secondly, the energy loss with distance travelled is inversely related to the energy, $dE/ds \sim 1/E$. Increasing the beam energy enable the electrons to penetrate to a greater depth because they lose their energy at a lower rate [1]. On the contrary, at lower incoming beam energy the interaction volume becomes smaller. If the incident beam energy is low enough (< 50eV), this would yield secondary electrons which would escape out of the surface of the sample depending on their work function. Figure 4.6 show the two major energy areas of electrons leaving the analyzed sample.

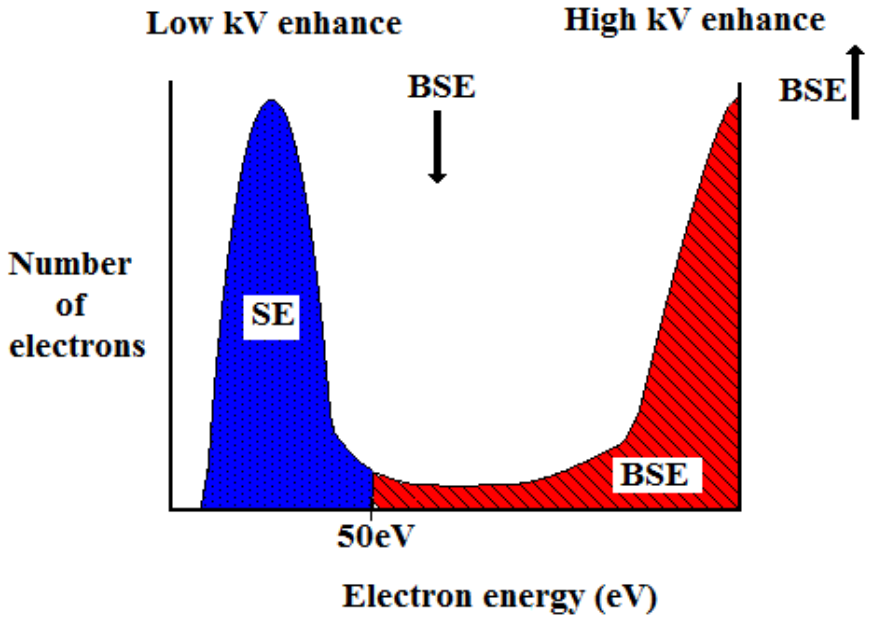

Figure 4.6 Schematic representation of the two major energy distribution of electrons emitted from the target. Backscattered electrons (BSE) – red and secondary electrons (SE) – blue.

(ii) **Atomic number**: For analyzed target samples with higher atomic number elements, the dimensions of the interaction volume decreases. The energy loss of the electron beam increases with atomic number and thus electrons do not penetrate as deeply into the sample. Also, the probability for elastic scattering and the average scattering angle increases with atomic number causing the interacting volume to widen. This is a direct consequence of the increase in the cross section for elastic scattering. As the electron beam loses energy faster because of high atomic number, some of the shallow penetrating electrons would be at energies below 50 eV. Upon interacting with the target atom would yield secondary electrons.

(iii) **Sample surface tilt**: The interaction volume becomes smaller and more asymmetric as the angle of inclination of the incident electron beam with the sample surface increases.

The image formation mechanism involved a high energy electron beam focused into a fine beam which is scanned across the surface of the sample. The interaction of the electron beam with the surface produces a wide variety of radiation products as discussed earlier. A sample of this radiation, e.g. secondary electrons, is collected by the detector. The collected signal is amplified and displayed on the cathode ray tube (CRT). The construction of the image, referred to as mapping, can be displaced in two principal ways, viz. line scans and area scans. In the line scan mode, the beam is scanned along a single vector on the sample, e.g. in the x or the y direction. The same generator signal is used to derive the horizontal scan of the CRT. In the area scan mode, the electron beam is scanned on the sample x-y pattern while the CRT is scanned in the same x-y pattern.

In this research, a Joel SEM was used at the earlier stages of study and later with the purchase of the Zeiss Ultra 55 field emission SEM, work was further carried on the new machine. The earlier SEM used the tungsten electron gun and later we used the SEM with the field emission electron gun. The field emission SEM is equipped with a variety of detectors. The secondary electron (SE) detector used to detect steep surfaces and edges that tend to be brighter than flat surfaces which results in images with a well-defined three-dimensional appearance. The backscattered electron (BSE) detector used to detect contrast between areas with different chemical compositions. The in-lens secondary electron (SE) detector which is highly surface sensitive with its efficiency improving as the accelerating voltage drops lower. For our research, depending on what we were looking for different detectors were used to study the surface of glassy carbon before irradiation, after irradiation and after annealing of irradiated samples. The results and discussions are given in chapter 6.

4.2 RAMAN SPECTROSCOPY

In 1928, Sir CV Raman discovered the phenomenon that bears his name that sunlight can be in-elastically scattered to produce patterns that represent different materials. He used sunlight as the source and telescope as the collector, the detector was his eyes. Gradually, improvements in the various components of Raman instrumentation took place where early research was concentrated on the development of better excitation sources (e.g., helium, bismuth, lead, zinc). But these proved to be unsatisfactory because of low light intensities. It was until 1962 that laser sources were developed for use with Raman spectroscopy. Eventually, the Ar^+ laser with wavelength ranging from 351.1 – 514.5 nm and the Kr^+ laser with wavelength

ranging from 337.4 – 676.4 nm became available [6]. In this research, the Ar/Kr mixed gas laser with wavelength ranging from 457.9 – 641.7 nm was used.

Raman spectroscopy is a technique based on inelastic scattering of light. Inelastic scattering means that the frequency of photons in the light changes upon interaction with a sample. Photons of the laser light are absorbed by the sample and then reemitted. The frequency of the reemitted photons is shifted up or down in comparison with original frequency, which is called the Raman effect. This shift provides information about vibrational, rotational and other low frequency transitions in molecules. If the scattering is elastic, the process is called Rayleigh scattering [7]. Today, laser Raman spectrometry has become an important method allowing the identification of molecules and a study of their structure, the characterization of chemical reactions, determination of some thermodynamic functions, and qualitative and quantitative analysis of molecular systems [8]. Though Raman spectroscopy is regarded as a non-destructive technique to study material, it can become destructive if high laser power is used or laser beam is focused on a spot for a long time leading to sample annealing or damage.

Modern instrumentation typically consists of a laser that is focused through a number of lenses onto the sample surface, and scattered light is passed into a spectrometer, which disperses the light onto a charge coupled device (CCD) detector, and the output collected and analyzed by the computer software, as shown in figure 4.4. The choice of laser wavelength can be varied depending upon the required application. One of the major advantages of dispersive Raman is that it offers the possibility to select the optimal laser excitation wavelength to permit the recording of the best Raman information. For example, wavelengths can be selected to offer the best resonance with the sample under investigation. It is the shift in wavelength of the inelastically scattered radiation that provides the chemical and structural information. Raman shifted photons can be of either higher or lower energy, depending upon the vibrational state of the molecule under study. A simplified energy diagram that illustrates these concepts is shown in figure 4.5. Stokes radiation occurs at lower energy (longer wavelength) than the Rayleigh radiation, and anti-Stokes radiation has greater energy. The energy increase or decrease is related to the vibrational energy levels in the ground electronic state of the molecule, and as such, the observed Raman shift of the Stokes and anti-Stokes features are a direct measure of the vibrational energies of the molecule. A schematic Raman spectrum is shown in figure 4.6. The energy increase or decrease from the excitation is related to the vibrational energy spacing

in the ground electronic state of the molecule and therefore the wavenumber of the Stokes and anti-Stokes lines are a direct measure of the vibrational energies of the molecule.

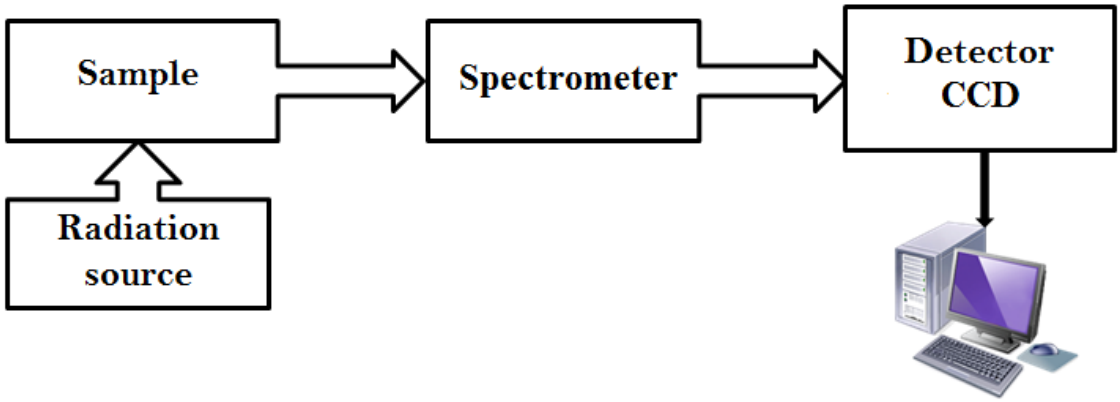

Figure 4.4 A typical Raman layout

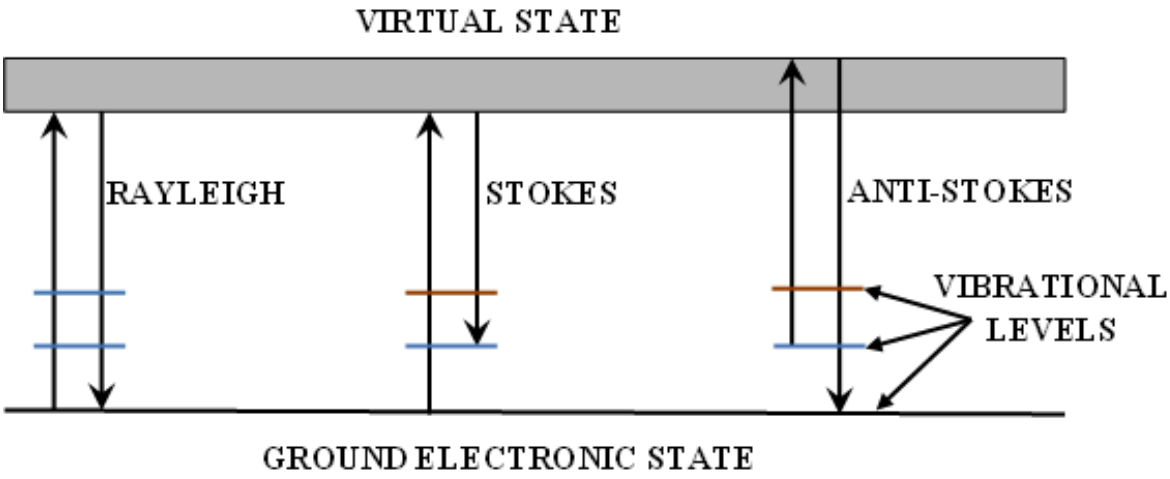

Figure 4.5 A simplified energy diagram for scattering of photons. Taken from [7].

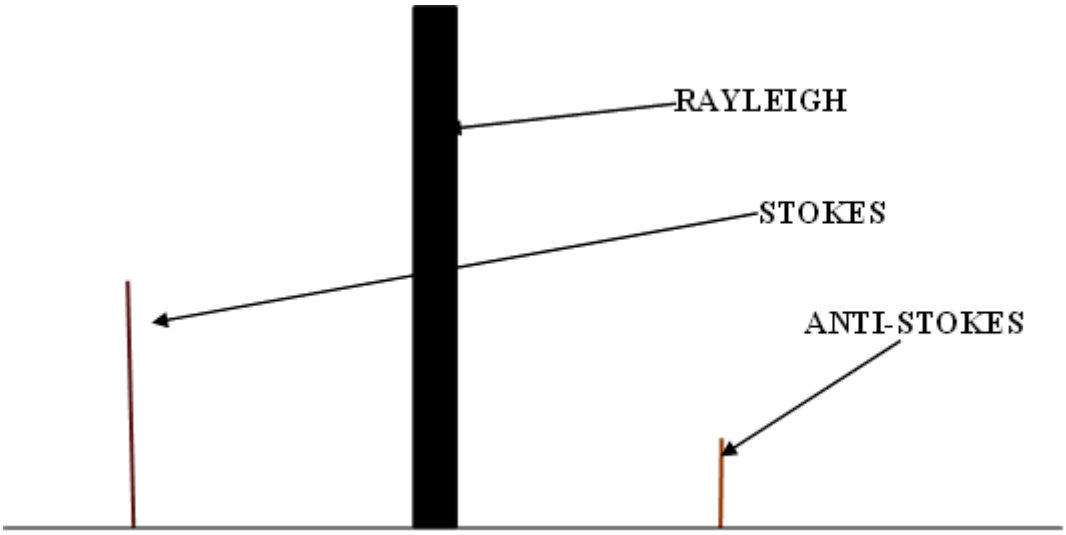

Figure 4.6 A schematic Raman spectrum. Taken from [7].

The Raman spectra contain a number of bands that enable the identification of substance by comparing the spectral pattern with those of the reference spectra, if the latter is available. Bands in the characteristic spectral region can be assigned to the molecular or crystal vibrations if information of the chemical composition of the sample is available. The vibrations of the symmetrically and weakly polar atoms normally result in intense Raman bands, since the Raman activity is connected to the changes in molecular polarizability during vibration. Unlike the infrared spectroscopy in which bands from vibration causing changes of the dipole moment dominates the spectrum. This is not required for Raman spectroscopy, because the scattering of the photons is elastic, and they have the same frequency and wavelength as the incident photons [9].

In this research the Raman effect on glassy carbon before and after ion irradiation and heat treatment of the irradiated samples were investigated. Thus it is importance to understand the Raman effect of carbon based materials. In this thesis we look at diamond, graphite, amorphous carbon, glassy carbon and how they differ from one another. Their Raman spectrums are shown in figure 4.7.

- **Pure diamond**: In the case of pure diamond, where the material consists of highly uniform C–C bonds in a tetrahedral crystal structure is very simple. The characteristic fingerprint of single crystal diamond (i.e. pure diamond) identified by Raman spectroscopy is a single sharp Raman line at 1332 cm^{-1}, known as the D peak. It consists

of single band because all of the bonds in the crystal are of the same orientation and strength resulting in a single vibrational frequency [Fil05]. This Raman peak characterizes the sp^3 configuration associated with diamond, where four valence electrons of carbon atoms are each assigned to a tetrahedrally directed sp^3 orbital [10]. In heavier crystalline atoms which share the same tetrahedral crystal configuration as diamond, the vibrational frequency is slowed down and this result in the shift of the corresponding Raman band to lower frequency [11].

- **Graphite**. In the three fold sp^2 configuration of graphite, three of the four valence electrons enter trigonally directed sp^2. The spectrum of single crystal graphite, like highly orientated pyrolitic graphite produces a single peak at 1575 cm^{-1} called the G peak. The reason for the main peak to shift from 1335 cm^{-1} in diamond to 1582 cm^{-1} in graphite is because the bond energy of the sp^2 bonded carbon atoms is higher than that of the sp^3 bonds in diamond. Since graphite, depending on growth, is not quite as uniform as diamond, there is normally the presence of an additional bands in the graphite spectrum. These additional bands are the signature of the difference in bond energies of the sp^2 bonds in graphite. These additional peaks that appear in crystalline graphite shouldn't be confused with the second peak that appears at 1335 cm^{-1} (called the D peak) in disordered graphite materials, like carbon black and activated charcoal. The intensity D peak increases relative to the G peak as (i) the amount of disordered carbon increase and (ii) the graphite crystal size decreases [11][12].

- **Amorphous carbon**. Amorphous carbon (a-C) is an unstructured mixture of sp^3 and sp^2 hybridized carbon. The ratio of the sp^2 to the sp^3 (sp^2/sp^3) of amorphous carbon film is determined by the deposition condition. The properties of these films are strongly depended on this ratio. Amorphous carbon films called tetrahedral amorphous carbon (ta-C) have high sp^3 content. By virtue of the way amorphous carbon films are prepared it is common for them to contain hydrogen, and are called hydrogenated amorphous carbon [12][13]. The Raman features of amorphous carbon films deposited at room temperature shows a broad signal in the region of 1000 – 1700 cm^{-1} [14].

- **Glassy carbon**. Glassy carbon is a particular form of disordered carbon and its Raman spectrum consists of a characteristic graphite peak at ≈ 1590 cm^{-1} (the G peak) and the disordered induced D peak at ≈ 1350 cm^{-1} [15]. As in disordered graphite explained above the D peak is a sort of disorder in glassy carbon. The G peak characterizes the sp^2

bonds just like in graphite and these confirm the theory that glassy carbon is consisting of graphite-like ribbons [14][15].

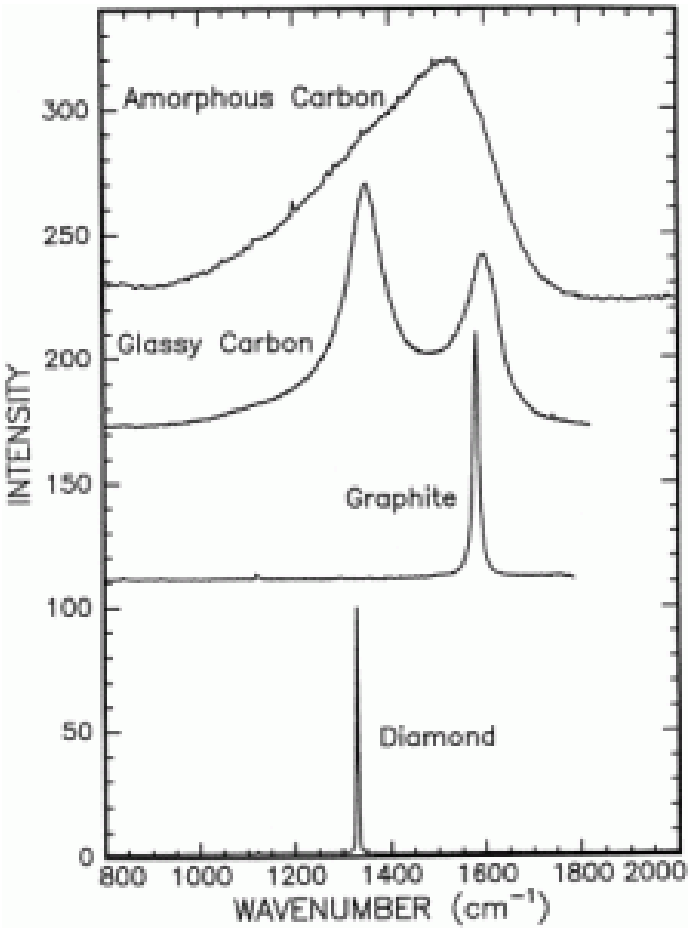

Figure 4.7 Raman spectrum of different kind of carbon based materials. Taken from [13].

4.3 RUTHERFORD BACKSCATTERING SPECTROMETRY

Rutherford backscattering spectrometry (RBS) was first introduced in the 1960s. It is one of the techniques used to address thin film properties in material research. RBS is frequently used for the quantitative analysis of the composition, layer thickness, and depth profiles of thin films.

4.3.1 RUTHERFORD BACKSCATTERING INSTRUMENTATION

A typical Rutherford backscattering spectrometry setup consists of a particle accelerator that can deliver a beam of low mass ions in the MeV range. In the case of this research helium

ions (He^+) and a van der Graaff accelerator were used. The typical ion beam scattering setup including the van der Graaff accelerator and the scattering chamber in the backscattering configuration are shown in figure 4.8. The ion source produces negative ions (He^-) that are accelerated towards positive potential. The He^- ions are transported in a vacuum system and at the high voltage electrons are stripped off and they become positive (i.e. He^+). Then the positive He ions repelled by the high positive voltage and increase their kinetic energy further. The beam of He^+ ions then passes through the focusing magnetic to get the straight beam at a desired current. Later the He^+ is bended by the analyzing magnet in the direction to the target chamber passing through a series of magnetic lenses that collimate the beam. The beam diameter is about a millimeter at the target. The detector, a Si surface barrier detector, is normally mounted in a backscattering angle θ. The scattering angle for optimum mass resolution would be 180° [9], but because of the detector size, as in the case of this research, 165° is chosen. As the incident He^+ particles penetrate the target some of them will experience a Coulomb force from the target nuclei and be deflected from their path. These collisions are governed by the Rutherford cross section and a small, though sufficient, number of the deflected ions will be backscattered into the detector. The kinematics of this choice of the backscattering angle and Rutherford backscattering cross section are discussed in detail in section 4.3.2.

In the silicon solid state detector used for the determination of energy of the backscattered ions, the ions create electron-hole pairs which are separated by an applied electric field and create a charge pulse. The number of electron-hole pairs is proportional to the backscattered ion energy. The energy resolution of silicon detectors has limitations that arise by fluctuation in energy transfer to electrons and phonons, and fluctuations in the annihilation of electron-hole pairs. The energy resolution for protons is almost independent of the backscattered ion energy [16][17].

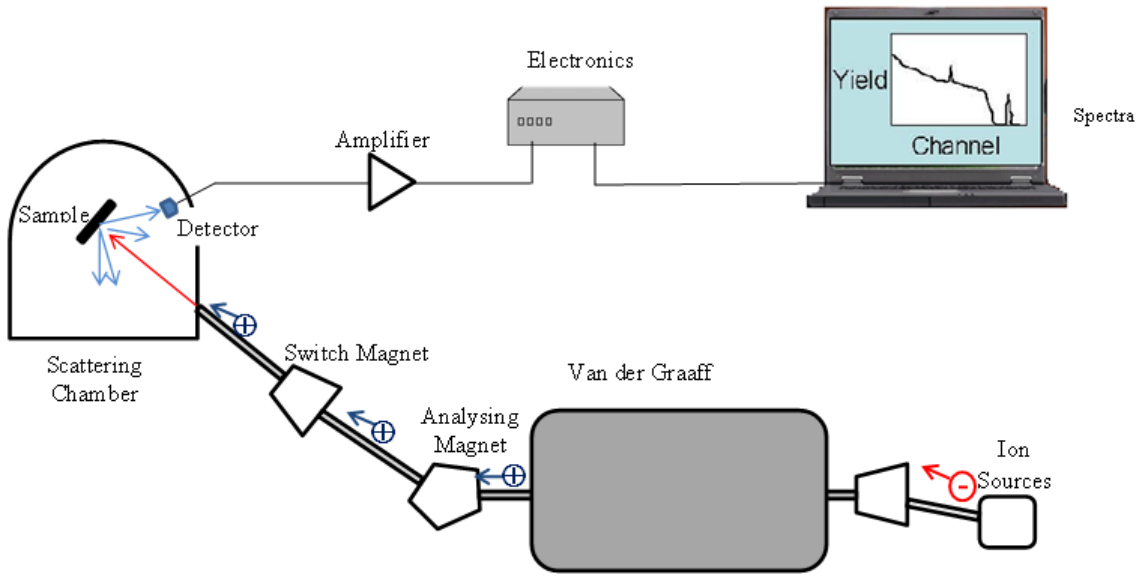

Figure 4.8 A typical layout of the RBS ion beam scattering setup

4.3.2 PRINCIPLES OF RUTHERFORD BACKSCATTERING SPECTROSCOPY

The basic principle in Rutherford backscattering is contained in the kinematics for binary collisions. A beam of energetic ions, normally He^+ or H^+ of energy ranging typically from 0.5 to 2.5 MeV, is directed at a target of particular mass, and the energies of the ions which are scattered backwards collected by a detector are analysed.

4.3.2.1 SCATTERING GEOMETRY AND KINEMATICS

A beam of incident particles (ions) with mass M_1 is given energy E_0 and directed onto the sample containing the particles with mass M_2 that are to be investigated. The scattering geometry used in this research is shown in figure 4.9. In this setup the target is placed in such a way that the incident beam is normal to the surface of the target sample and the detector is placed at the backscattering angle of $\theta = 165°$ with respect to the incident beam.

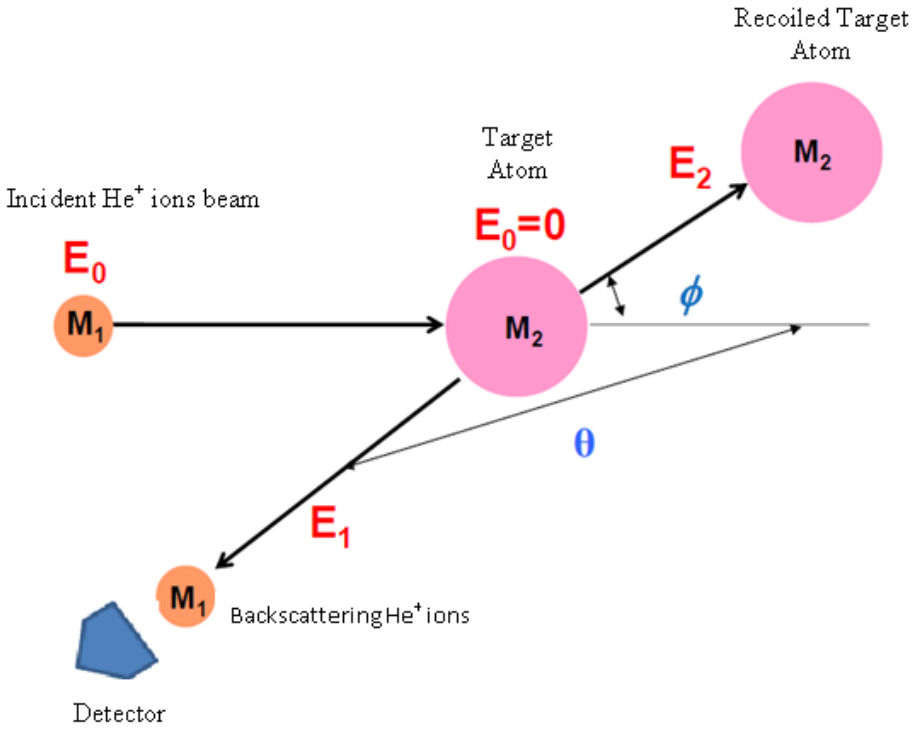

Figure 4.9 Scattering geometry for the RBS experiment setup at the University of Pretoria

During the collision, energy is transferred from the incident particle to the stationary target atom. For $M_1 < M_2$, as in the case of this research, the energy ratio between the backscattered energy E_1 after collision and the incident energy E_0 before collision derived from the binary collision theory is given in the laboratory system by [16][9]:

$$K = \frac{E_1}{E_0} = \left[\frac{\left(M_2^2 - M_1^2 \sin^2\theta\right)^{1/2} + M_1 \cos\theta}{M_1 + M_2}\right]^2 \qquad (4.1)$$

where K is called the kinematics factor. Equation 4.1 gives the ratio of the projectile energy after elastic scattering to that before collision. However, in RBS the incident ions penetrate the target and they may be backscattered at any point along their path. As the particles traverse the solid, they lose energy along the incident path and on the outward path they also again lose energy. The total energy loss per unit length, dE/dx, is called the stopping power and was discussed in detail in chapter 3. These additional energy losses as the incident beam traverse the target material broaden the peak to be observed in an RBS spectrum for thin samples. The particle that are scattered by the surface atoms have the energy KE_0. Those that traversed

through the target and scattered at a depth *x*, they lose energy through the inward part and the outward path. Their energy detected when they emerge from the surface is E_1. The energy E_1 depends on the path at which scattering occurred. The backscattering yield at that energy depends on the number of atoms present at that depth. Figure 4.10 describes the events that are happening when the incident particles traverse through the consisting of one element.

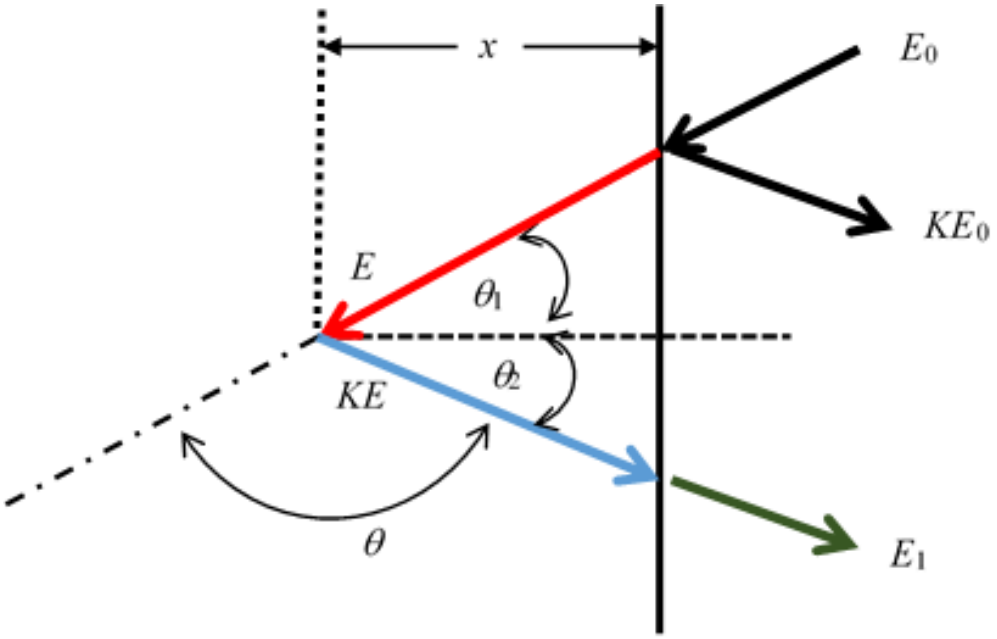

Figure 4.10 A schematic diagram of the incident beam with energy E_0 traversing through the material. The energy immediately before scattering at a depth x is E, and the energy of the particle emerging from the surface is E_1

From equation 4.1, one observes that target atoms (M_2) with lower mass will have a smaller kinematic factor as compared with those with heavier mass. Thus the energy spectrum produced by scattering from lower mass atoms will start at lower energies compared to scattering from higher mass atoms [9]. This observation will be shown in the results of this research in chapter 6, where glassy carbon is implanted with silver or cesium. If the film deposited on the surface of the substrate is of lower mass as compared to the substrate, then the peak arising from the surface layer will merge in the broad continuum and appear as a small feature on top of it. Equation 4.1 also contains the essence of how backscattering spectrometry acquires its ability to sense the mass of an unknown target atom. If the energy E_0 and the mass M_1 of the incident ion is known, and the energy E_1 of the backscattered ions is measured at the

known angle θ. That leaves the mass M_2 of the target that prompted the scattering as the only unknown in the equation [16].

4.3.2.1 DEPTH AND COMPOSITION MEASUREMENTS

In RBS, energy loss of a backscattered ion is dependent on two processes, i.e. the energy lost to small-angle scattering from the sample electrons, and the energy lost in scattering events with sample nuclei. The first energy loss process, the stopping power of the sample electrons, does not result in large discrete losses such as those produced by nuclear collisions. Instead it creates a gradual energy loss dependent on the electron density and the distance traversed in the sample. This energy loss will lower the measured energy of ions which backscatter from nuclei inside the sample in a continuous manner dependent on the depth of the nuclei. The result is that instead of the sharp backscattered peaks one would expect on a spectrum, with the width determined by energy and angular resolution, the peaks observed trail off gradually towards lower energy as the ions pass through the depth occupied by that element. Thus by knowing the composition of the target element it is possible to determine the depth scale for the distribution on an element, or to measure the layer thickness from the energy of the scattered particles. The relation between the energy of backscattered particles and the sample depth is given by [18]:

$$\Delta E = [S] \cdot x \tag{4.2}$$

where

$$\Delta E = KE_0 - E_1 \tag{4.3}$$

The energy E_1 is the measured value of a particle scattered from an atom at depth x. The energy KE_0 is the edge of the backscattering spectrum and correspond to the energy of particle scattered from atoms at the surface of the target. The symbol ΔE represents the energy difference between E_1 and KE_0, and [S] is called the energy factor.

The quantity S reflects the total stopping power for the incident and scattered particles, and is called the stopping cross-section or the energy loss factor, given by [19][16]:

$$S(E) = \frac{K}{\cos\theta_1}\frac{dE}{dx}\bigg|_{E_{in}} + \frac{1}{\cos\theta_2}\frac{dE}{dx}\bigg|_{E_{out}} \tag{4.4}$$

The second process is dependent on the scattering cross-section of the nucleus and thus on its mass and atomic number. For a given measurement angle, nuclei of two different elements will therefore scatter incident ions to different degrees and with different energies, producing separate peaks on a spectrum of measurement count versus energy. These peaks are characteristic of the elements contained in the material, providing a means of analyzing the composition of a sample by matching scattered energies to known scattering cross-sections. Relative concentrations can be determined by measuring the heights of the peaks. The height H of an RBS spectrum at the surface is given by [20]:

$$H = F\left(\frac{d\sigma}{d\omega}\right)_{E_0} \frac{sNdE}{S_0} \tag{4.5}$$

In practice, then, a compositional depth profile can be determined from an RBS N(E) measurement. The elements contained by a sample can be determined from the positions of peaks in the energy spectrum. Depth can be determined from the width and shifted position of these peaks, and relative concentration from the peak heights. This is especially useful for the analysis of a multilayer sample, for example, a sample with a composition which varies more continuously with depth.

4.4 REFERENCES

[1] J. Goldstein *et al.*, *Scanning Electron Microscopy and X-ray Microanalysis*, 3rd ed. New York: Plenum Press, 2003.

[2] J. Atteberry, "HowStuffWorks.com," *"How Scanning Electron Microscopes Work."* [Online]. Available: http://science.howstuffworks.com/scanning-electron-microscope.htm. [Accessed: 19-Aug-2015].

[3] B. Hafner, "Scanning electron microscopy primer," *Charact. Facil. Univ. Minnesota-Twin Cities*, pp. 1–29, 2007.

[4] W. C. H. Kuo, M. Briceno, and D. Ozkaya, "Final Analysis: Characterisation of Catalysts Using Secondary and Backscattered Electron In-lens Detectors," *Platin. Met. Rev.*, pp. 106–110, 2014.

[5] N. R. Whetten, "Methods in Experimental Physics IV," *Part A, At. Electron*, 1962.

[6] J. C. Ferraro, K. Nakamoto, and C. W. Brown, *Introductory raman spectroscopy*. Academic press, 2003.

[7] E. Smith and G. Dent, *Modern Raman spectroscopy: a practical approach*. Chichester: John Wiley & Sons, 2005.

[8] H. Baranska, A. Labudzinska, and J. Terpinski, *Laser Raman spectrometry: analytical applications*. New York: John Wiley and Sons, 1987.

[9] G. Friedbacher and H. Bubert, Eds., *Surface and Thin Film Analysis: A*

Compendium of Principles, Instrumentation, and Applications. Weinheim: John Wiley & Sons, 2011.

[10] J. Robertson, "Diamond-like amorphous carbon," *Mater. Sci. Eng. R Reports*, vol. 37, pp. 129–281, 2002.

[11] J. Hodkiewicz, "Characterizing carbon materials with raman spectroscopy," *Thermo Sci. Appl. Note*, vol. 51901, pp. 1–5, 2010.

[12] J. Filik, "Raman spectroscopy : a the lightest touch," *Spectrosc. Eur.*, vol. 17, pp. 10–16, 2005.

[13] P. K. Chu and L. Li, "Characterization of amorphous and nanocrystalline carbon films," *Mater. Chem. Phys.*, vol. 96, pp. 253–277, 2006.

[14] J. Schwan, S. Ulrich, V. Batori, H. Ehrhardt, and S. R. P. Silva, "Raman spectroscopy on amorphous carbon films," *J. Appl. Phys.*, vol. 80, pp. 440–447, 1996.

[15] S. Prawer, F. Ninio, and I. Blanchonette, "Raman spectroscopic investigation of ion-beam-irradiated glassy carbon," *J. Appl. Phys.*, vol. 68, pp. 2361–2366, 1990.

[16] W. K. Chu, J. W. Mayer, and M. A. Nicolet, *Backscattering Spectrometry*. New York: Academic Press, 1978.

[17] M. Mayer, "Rutherford backscattering spectrometry (RBS)," *ICTP Lect. Notes*, p. 55, 2003.

[18] L. C. Feldman and J. W. Mayer, *Fundamentals of surface and thin film*

analysis. Amsterdam: North-Holland Publishing Company, 1986.

[19] J. O'Connor, B. A. Sexton, and R. S. C. Smart, *Surface analysis methods in materials science*, vol. 23. New York: Springer, 2003.

[20] J. M. Walls, Ed., *Methods of surface analysis: techniques and applications*. Cambridge: Cambridge University Press, 1990.

CHAPTER 5

EXPERIMENTAL

The samples used for this research were SIGRADUR®G glassy carbon from Hochtemperatur-Werkstoffe (HTW), Germany. The glassy carbon (GC) samples as the substrate had a thickness of 1 mm and were mechanically polished to a mirror finish with a 1 μm diamond solution and cleaned consecutively with alkaline soap, de-ionized water, acetone, and methanol and dried with nitrogen gas. Finally, the samples were placed in an oven at 80ºC about 30 minute to evaporate volatile impurities on the surface. Two different methods were used to investigate the diffusion behaviour in glassy carbons. Firstly, thin silver films deposited onto the glassy carbon surface by thermal evaporation then annealed to investigate the diffusion into the carbon. Secondly, the samples were implanted at room and high temperatures, separately, with silver and cesium ions. Scanning Electron Microscopy (SEM) was employed to investigate the effect of implanted ions and annealing on the microstructure of the substrate. The depth profiles of the implanted samples before and after annealing were obtained by ion beam technique, viz. Rutherford Backscattering Spectrometry (RBS). Raman spectroscopy has been used to monitor the changes induced in the structure of glassy carbon as a result of implantation and heat treatment.

5.1 THERMAL VAPOUR DEPOSITION

This silver film of about 100 nm thickness was grown on to the glassy carbon substrate, mounted on the multiple steel samples holder, by thermal evaporation at room temperature. The thickness of the grown layer was monitored by the water cooled crystal monitor by controlling the rate of the material evaporate and time. The substrate was placed in a high vacuum chamber under a vacuum of about 10^{-6} Pa. This is done in a high vacuum, both to allow the vapor to reach the substrate without reacting with or scattering against other gas-phase atoms in the chamber, and reduce the incorporation of impurities from the residual gas in the vacuum chamber. The silver to be evaporated was placed in the molybdenum crucible connected the tungsten wires (see figure 5.1).

A current of about 4 A was applied through the tungsten wires to the molybdenum crucible until it heat up beyond the melting point of silver. In this system a shielding plate is placed between crucible, and substrate and crystal monitor until the silver has reached its melting point and evaporate. Then the shielding will be turned to allow the evaporating silver to reach the substrate and the crystal monitor. This is done to minimize the contaminants from the crucible to deposit onto the substrate before the desired silver layer. Upon opening the shielding plate, the evaporating silver condensed on the entire exposed cool surface in the vacuum chamber. As shown in figure 5.1, the deposition of silver onto the substrate was only performed of the side facing the crucible. Evaporated materials deposit non-uniformly if the substrate has a rough surface. The crystal monitor was used to calculate the approximate thickness of the later growth.

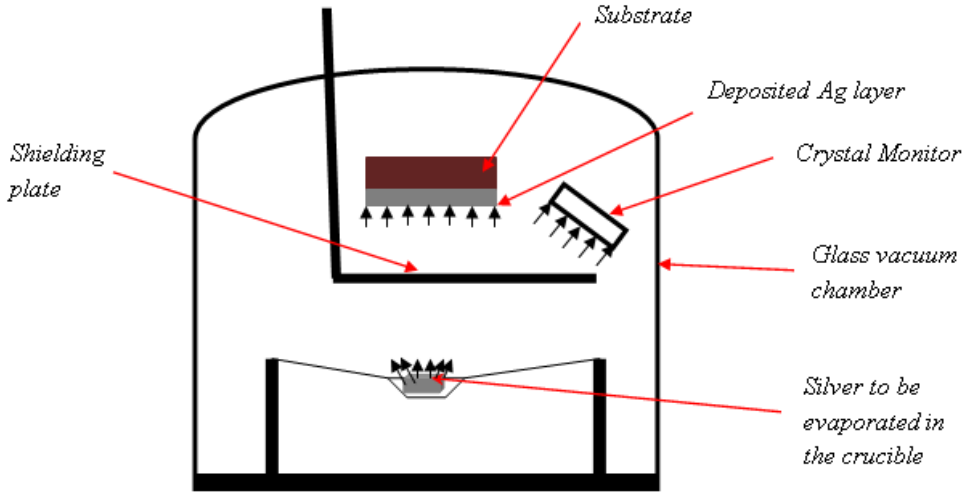

Figure 5.1 A schematic representation of the silver deposition process in a vacuum chamber

5.2 IMPLANTATION OF SILVER AND CESIUM

Silver was implanted on the polished and the unpolished glassy carbon samples while cesium was only implanted on the polished samples. All the implantations for this research were performed by the 400 keV ion implanter at the Institut für Festkörperphysik, Friedrich-Schiller-Universität, Jena, Germany. Silver and cesium ions were implanted at an energy of 360 keV to a fluence of 2×10^{16} ions/cm^2. The flux was maintained at the rate of about 10^{13} cm^{-2}s^{-1} to minimize the increase in the substrate temperature, reducing the probability of

simultaneously annealing some of the radiation damage produced during the room temperature implantations ions. The implantations were done at three different substrate temperatures, viz. room temperature (RT), 350 and 600 °C at a time of approximately 33 minutes.

5.3 SAMPLES ANNEALING

The samples were placed quartz glass tube attached to a turbo pump vacuum system. The quartz tube was then evacuated to about 10^{-6} mbar. The trolley mounted annealing tube furnace, with a maximum temperature of 1000 °C, can move front and back to insert the glass tube until the sample is positioned approximately at the center of the tube furnace. This maximum temperature is reached in the center of the oven and decreases towards tube opening and slight towards the side of the tube. A thermocouple placed near the sample's position is connected to computer software to record the temperature as a function of time during annealing. Before annealing was performed, the furnace was allowed to stabilize at the preset temperature before moving it to a position where the sample was centered in the middle of the furnace for annealing. This method allows the sample to reach the annealing temperature quickly, thereby minimizing any diffusion at temperatures lower than the annealing temperature. The schematic representation of the annealing system used in this research is shown in figure 5.2. The double heated arrow illustrated on the tube furnace simple show that the furnace is placed on a movable table allowing the back and front motions. At the end of the annealing time, the tube furnace was moved back and the sample was the allowed to cool down quickly (again minimizing any diffusion at temperatures lower than the annealing temperature) to room temperature before breaking vacuum to take out the sample. All the annealing studies were conducted using this furnace.

The unpolished glassy carbon samples with silver grown on the surface were annealed at temperatures ranging from 350 to 750 °C. These temperatures are all below the melting point (962 °C) of silver. The silver implanted samples were annealed at temperatures ranging from 350 to 800 °C while the cesium implanted samples were annealed at temperatures from 200 up to 600 °C, temperatures above the melting point (~28 °C) but below boiling point (~671 °C) of cesium. A typical annealing curved is depicted in figure 5.3 for samples annealed at about 430 and 680 °C.

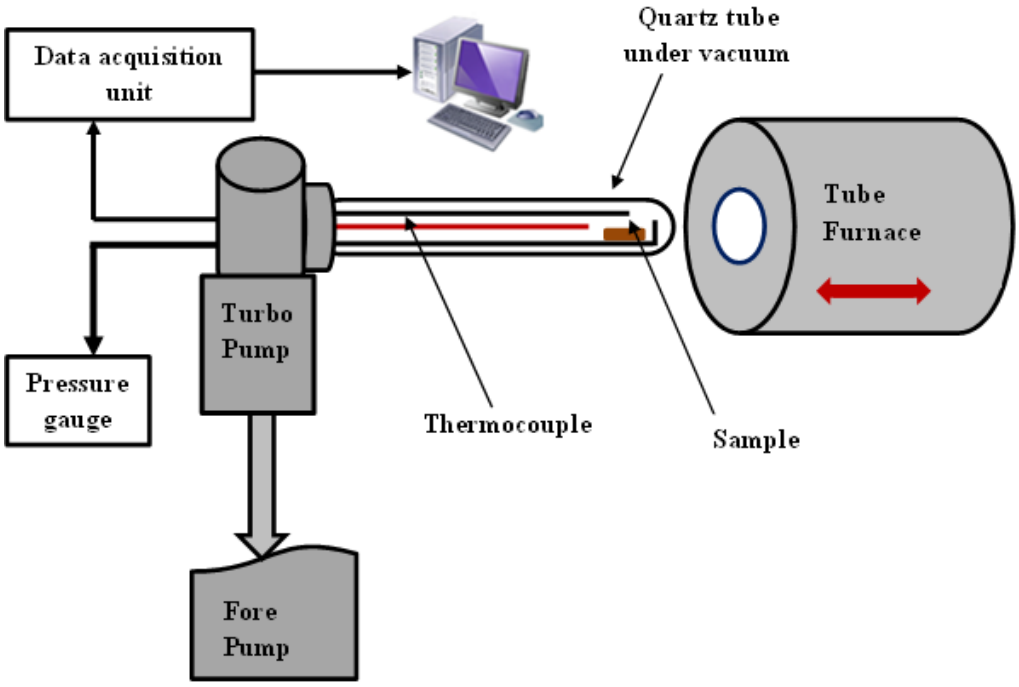

Figure 5.2 The schematic representation of the annealing system

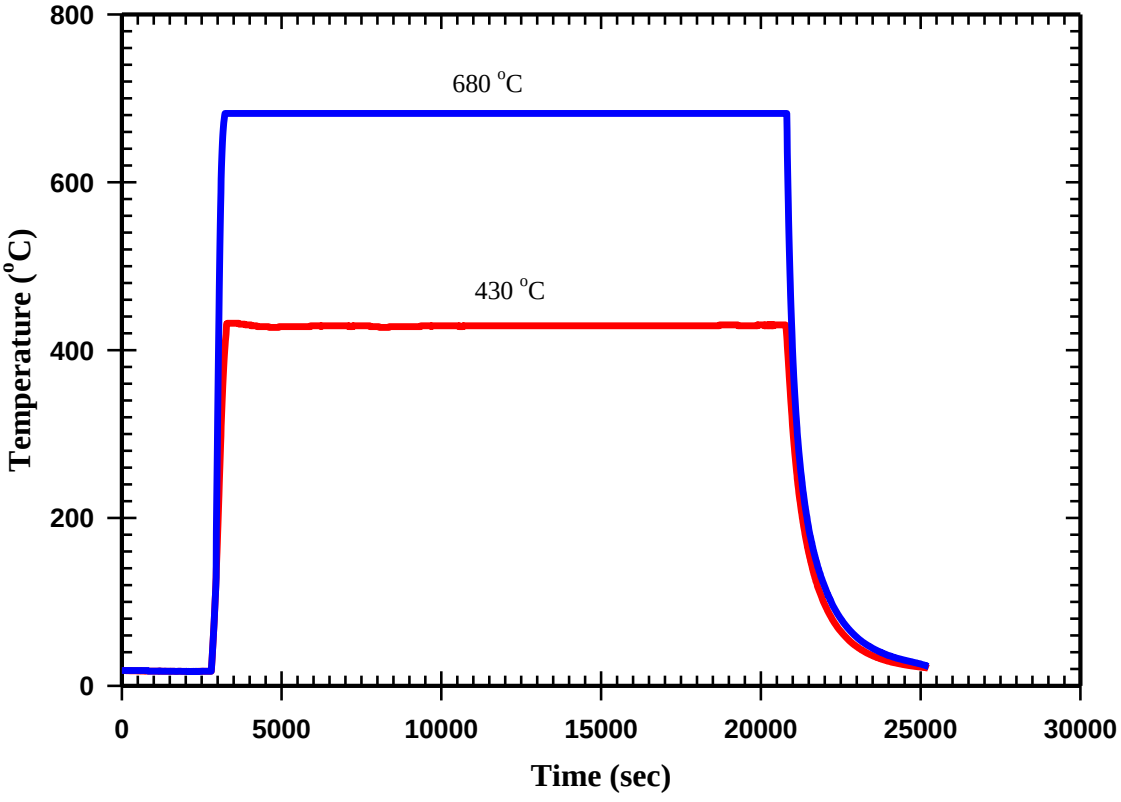

Figure 5.3 Annealing temperature vs annealing time

5.4 ANALYSING AND MEASUREMENTS METHODS

5.4.1 SCANNING ELECTRON MICROSCOPY (SEM)

A JEOL JSM-5800 LV scanning electron microscopy (SEM) was used at the beginning and later we acquired an Ultra ZEISS 55 field emission gun. They were employed to investigating the effect of implantation and annealing temperature on the microstructure of the samples surface. The accelerating voltage was varied between 2 and 20 kV depending on to whether we wanted a dominance of the secondary electrons or the backscattered electrons to use for a particular measurement. Higher accelerating voltages yield more backscattered electrons while lower accelerating voltages yield more secondary electrons. Having said that, the in-lens detector used in this study is a high efficiency detector for high resolution secondary electron imaging. Since the efficiency of the in-lens detector is dependent on the electric field of the electrostatic lens and this electric field decreases exponentially with distance, the working distance was optimised to minimise the effects on the signal-to-noise ratio of the in-lens detector. The accelerating voltage of the primary beam was maintained very low. This allowed the primary electron range to be more and shallower. So that an increasing fraction of the secondary electrons are produces near the surface and can therefore escape.

5.4.2 RAMAN SPECTROSCOPY

The glassy carbon structural changes due to implantation and heat treatment were monitored with a T64000 micro-Raman spectrometer from HORIBA Scientific, Jobin Yvon Technology. The Raman spectra were excited with the 514.5 nm line of an Inova 70v argon laser from Coherent and it is equipped an Olympus confocal microscope with 10×, 50× and 100× microscope objective to focus the laser beam on the sample. An integrated triple spectrometer was used in the double subtractive mode to reject Rayleigh scattering and dispersed the light onto a liquid nitrogen cooled Symphony CCD detector to produce the Raman signal. In this study, optimum recording conditions were obtained by varying laser power but always maintained less than 10 mW to prevent sample heating. To ensure uniformity, the 50× objective and acquisition time of 120 seconds (×2) were used throughout. Only for one sample where laser beam annealing of the sample surface was done, the 20 mW power and 100× objective were used. A clean part of the sample surface was selected by visual examination

under the microscope objective before analysis to obtain the Raman signature. Each sample was analysed in more than one spot to make sure that the spectra were representative. All measurements were performed at room temperature.

5.4.3 RUTHERFORD BACKSCATTERING SPECTROMETRY (RBS)

5.4.3.1 DATA ACQUISITION

The block diagram for the RBS electronic circuit used in the detection, amplification and collection of the backscattered alpha particles is illustrated by the schematic diagram in figure 5.4. These backscattered particles were detected by a silicon surface barrier detector located at an angle of 165° relative to the incident beam. The detector requires a biased voltage of 40 V and is supplied by the Canberra 30103D high voltage device. The output charge signal from the detector were first amplified by the Canberra 220 pre-amplifier before being fed into the Tennec 243 main amplifier. The main amplifier produces the bipolar output signal that was fed to a digital oscilloscope to monitor the shape of the output pulse. On the other end the same amplifier produces a unipolar output signal that was fed to the multi-channel analyser (MCA). The MCA identifies the number and energy of the alpha particles scattered through large angles by the sample into the detector.

The current collected at the back of the target sample was transported to a digitized Ortec 439 current integrator. From the current integrator a logical signal was send to the charge counter where its output was delivered to the MCA. The logical signal from this current command the MCA when to start processing the unipolar signal. The data acquisition system was the multichannel analyser and the computer. The MCA converted the signal height, which is proportional to the energy, into 512 channels with energy ranging from 0 to 1.6 MeV. In each channel a reading was collected which have a specific energy of the scattered alpha particle. The data was displayed as counts versus channel number. The beam current during measurement was maintained between 10 and 15 nA to minimize heating the target sample, and the charge collected in all the samples spectra was 8 μC. Ten runs per sample analysed were taken in order to reduce the statistical error, and the average of the runs was used for further analysis.

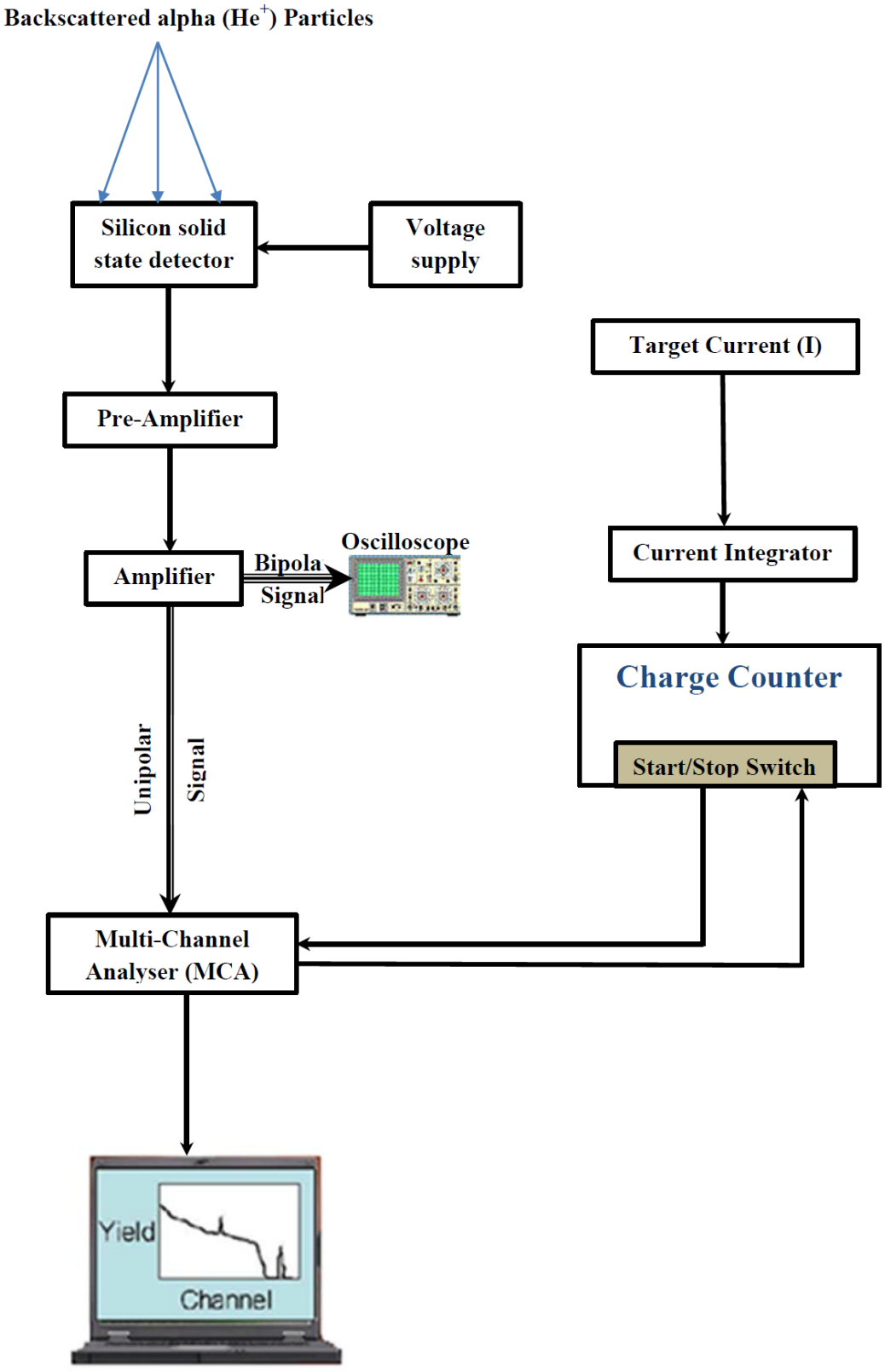

Figure 5.4 Block diagram for the RBS electronic circuit at the University of Pretoria

5.4.3.2 DATA ANALYSIS

All the spectra which were stored in the computer connected to the MCA were taken for further analysis. The energy calibration required for depth profiling analyses was calculated from the RBS measurement of silicon carbide, as our calibration sample, using energies of 1.4 and 1.6 MeV α-particles. Using the kinematic factor of carbon and silicon calculated from equation 4.1, the energy

$$E_1 = E_0 K \tag{5.1}$$

for the two different incident energies was calculated. The surface channel numbers for the carbon and silicon at these two incident energies were also extracted from the RBS spectra of silicon carbide. Then the graph of the channel numbers versus energy (E_1) was plotted. The energy per channel, in keV/channel, was calculated from the slope of the graph. The offset was extracted from the graph as the channel number when the energy $E_1 = 0$. These values were used to convert counts versus channel profiles to counts versus depth profiles using the computer program spectra management. This was done for both the silver and cesium spectra.

The counts were converted to percentage relative atomic density (RAD %) of silver or cesium into glassy carbon (GC) using the equation:

$$\text{RAD}\% = \frac{\rho_{Ag}}{\rho_{GC}} \times 100\% \tag{5.2}$$

Note that the subscript Ag relate to the calculation with silver as the implanted material, but the same equations were used in case of cesium. For this study glassy carbon has density of 1.42 g/cm^3, with an equivalent atomic density (ρ_{GC}) of 7.119×10^{22} atoms/cm^3. The density of silver inside glassy carbon (ρ_{Ag}) was calculated using the equation:

$$\rho_{Ag} = \frac{(\text{Total fluence})(\text{count/channel})}{ND} \tag{5.3}$$

where N is the total number of silver counts and D is the depth resolution taken from the difference between two successive depth values. A Matlab program was written in-house to fit our depth profile data for isochoric annealing and extract the diffusion coefficients at the

different temperatures when the diffusion was Fickian. From this program we also get the experimental projected ion range (R_p) and the straggling (ΔR_p) [1].

The other method we used in determining the diffusion coefficient, was to isothermal anneal the samples. Using OriginPro 8.1 the depth profiles for isothermal annealing were fitted using the Breit-Weigner-Fano (BWF) equation. From the fittings peak analysis was performed to calculate the half width at maximum $[W(t)]^2$. Then the linear graph of $[W(t)]^2$ versus annealing time was plotted. Using the slope of the graph and the equation

$$[W(t)]^2 = (4D\ln 2)t + [W(0)]^2 \qquad (5.4)$$

the diffusion coefficient (D) for isothermal annealing was calculated.

5.5 REFERENCE

[1] J. B. Malherbe, P. A. Selyshchev, O. S. Odutemowo, C. C. Theron, E. G. Njoroge, D. F. Langa, and T. T. Hlatshwayo, “Diffusion of a mono-energetic implanted species with a Gaussian profile,” *Nucl. Instruments Methods Phys. Res. Sect. B Beam Interact. with Mater. Atoms*, vol. 406, pp. 708–713, 2017.

CHAPTER 6

RESULTS and DISCUSSION

Experimental results, characterization results as well as simulation results of this study are reported in this chapter. A complete analysis and discussion are also presented herein, whilst the summary and conclusion derived from these results as well as suggestions for further studies are deferred to the next chapter. This chapter is organized to present the measurement and analysing techniques results and discussion as follows: section 6.1 the scanning electron microscopy, sections 6.2 the Raman spectroscopy and 6.3 Rutherford backscattering.

6.1 SCANNING ELECTRON MICROSCOPY RESULTS

Diffusion of silver into glassy carbon (SIGRADUR® G) was first investigated using the surface layer in-diffusion. The glassy carbon samples with 100 nm thickness layer of naturally occurring silver on their surface were vacuum annealed for 5 hours at temperatures of 600°C and 750°C. Figure 6.1 presents the SEM results of these samples. From the SEM investigation of the sample annealed at 600 °C, it was observed that silver did not diffuse into the surface but rather moved along the surface making island structures. This was because as the temperature was increased, there was surface diffusion of silver. Also observed was silver crystals formation of different sizes and crystal orientations with some formed on top of others. This solid state crystal formation was in line with the BCF theory [1]. At a temperature of 750 °C the island structures became smaller resulting in lines of silver in a preferred cell structure on the surface of glassy carbon, see figure 6.1 (B). This preferred cell structure formed by silver could be the signature of the surface defects on the substrate. This negative result (for in-diffusion) was attributed to a wetting problem between silver and glassy carbon, resulting from a stronger silver-silver bonding as compared to the silver-glassy carbon bonding.

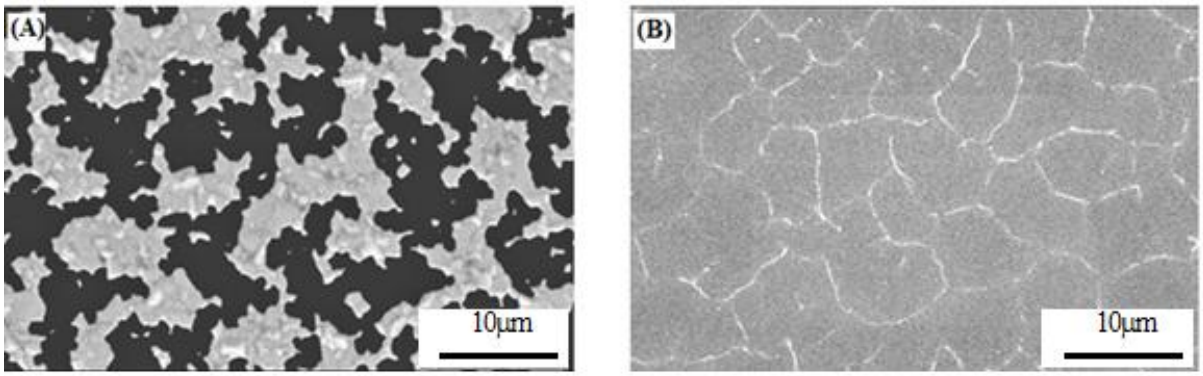

Figure 6.1 SEM micrograph of glassy carbon with silver on the surface after annealing for 5 hours at temperatures of (A) 600 °C and (B) 750 °C.

Due to the negative results of the silver layer in-diffusion onto glassy carbon, further research was undertaken into the diffusion in glassy carbon by employing the second method, viz. ion implantation. With this method the diffusion of silver and cesium were investigated by implanting them separately into glassy carbon at room temperature (RT), 350°C and 600°C. In figure 6.2 we show the SEM micrographs of the glassy carbon sample taken by the InLens detector for the secondary electrons (SE1) (see figure 4.4), under the following conditions:

(i) un-polished,

(ii) polished

(iii) un-polished and implanted with carbon with silver implanted at 360 keV with a fluence of 2×10^{16} Ag^{+}/cm^{2} at room temperature, and

(iv) polished and implanted with silver implanted at 360 keV with a fluence of 2×10^{16} Ag^{+}/cm^{2} at room temperature

The InLens detection system has an objective lens that sends a strong magnetic field to the sample plane. The major consequence of the strong magnetic field is to trap with high efficiency the SE1 – see section 4.1. The un-polished surface in figure 6.2 (a) looked fairly smooth with no visible features. After Ag implantation on the unpolished surface, we observed some holes, as shown in figure 6.2 (c). Similar results were reported when glassy carbon implanted with neon ions and the holes are revealed [2]. In a subsequent experiment, we

polished the glassy carbon surface then implanted with Ag again. The holes that were observed earlier were not seen. It was concluded that the holes observed were on the surface glassy carbon substrate and were an artifact of the manufacturing process. Since such cavities may affect the RBS analysis of our samples, all glassy carbon samples were polished before being used in our experiments.

The polished surface shows some polishing marks, though not prominent, as shown in figure 6.2 (b). This was due to the fact that some of the glassy carbon material removed during polishing was loosely bonded to the surface/bulk of the glassy carbon substrate within the polishing marks. There loosely bonded carbon material were not removed during the ultrasonic cleaning process used in this study. After implantation with silver ions at room temperature, the polishing scratch lines were much more visible as observed in figure 6.2 (d). This was due to the preferred sputtering of the loosely bounded carbon atoms to expose the scratches. The polished surfaces showed no holes after implantation. This indicated that the observed cavities and the appearance of holes during implantation was due to a manufacturing artifact as discussed above.

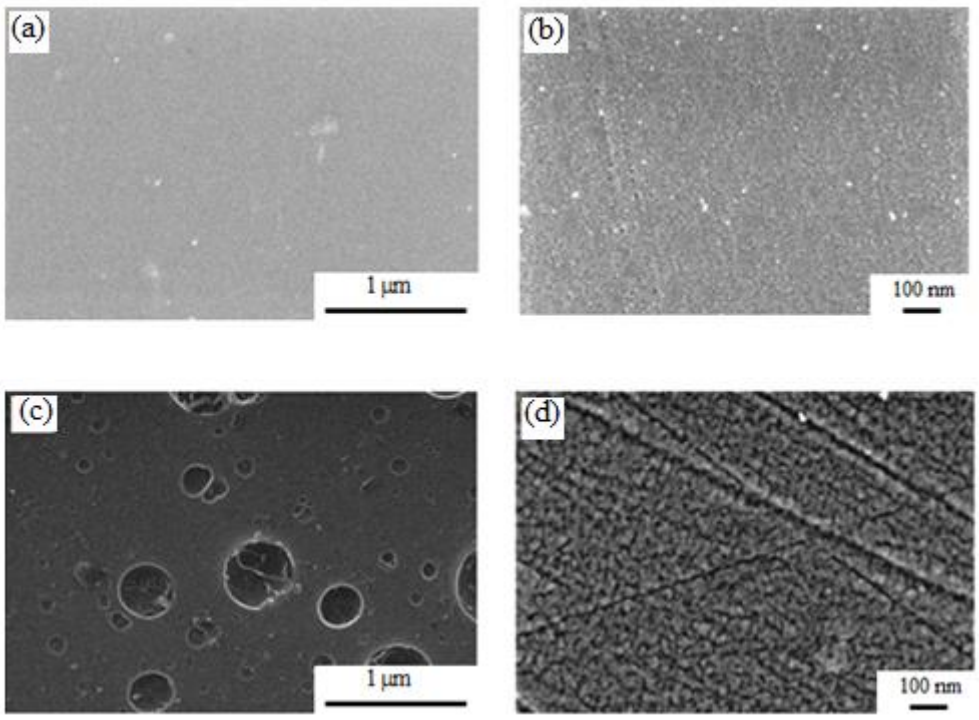

Figure 6.2 SEM micrograph of glassy carbon (a) un-polished, (b) polished (c) un-polished and implanted with silver, and (d) polished and implanted with silver.

As can be seen in figure 6.2 (c), the details of the bottom of the holes are not that visible. This is because of the collection of the SE1 depends on the magnetic field of the objective lens penetrating into the cavity. The image of the InLens detector is limited to the depth to which this magnetic field can reach. To determine whether the features observed in figure 6.2 (c) were either cavities or hillocks, the sample was tilted and a normal SEM image was taken, i.e. using SE2 (see figure 4.4). Though for this detector some of the backscattered electrons (BSE) would reach the surface of the detector. To minimize the effect of large number of collection of BSE, the detector is biased positively. The low-energy secondary electrons will be accelerated to a sufficient energy to generate light in the scintillator. The orientation of the sample is shown with the red line parallel to the surface of the image/page while the beam struck the sample at the angle of 46° into the page. Extreme bright regions on the sample were due to the increased electrons emission levels from areas pointing towards the detector. A cavity or a dip would have a bright back and dark front, while a mound or bump would have a dark back and bright front. Thus, from Fig. 6.3 we can conclude that what we observed were cavities.

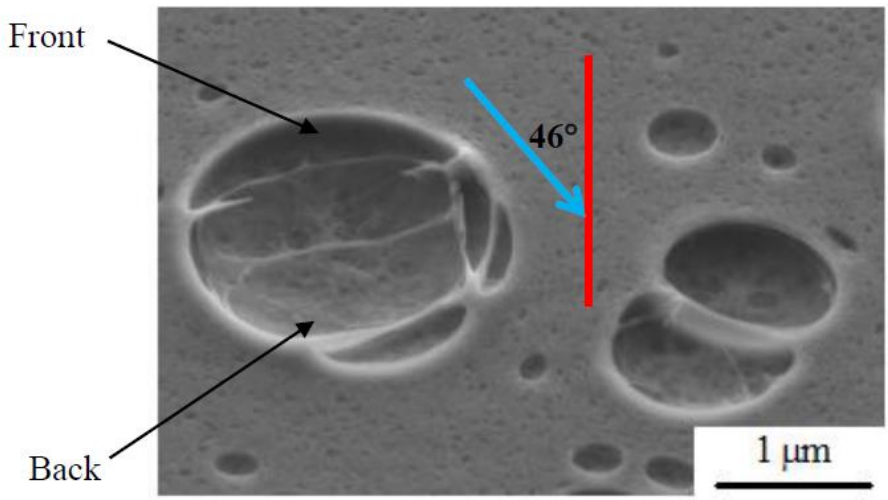

Figure 6.3 SEM micrograph of the un-polished glassy carbon implanted with silver at 360 keV.

Polished glassy carbon samples were also implanted with 2 x 10^{16} Cs^{+}/cm^{2} at room temperature and 600 °C. The room temperature samples were annealed at 200 °C for 8 hours. Figure 6.4 (a) – (c) show the SEM images of the glassy carbon surface of three samples which were taken at a very low incident beam voltage of 0.6 kV using the InLens detector. The polishing scratches became more prominent on the glassy carbon implanted with cesium at room temperature after annealing at 200 °C temperature for 8 hours. The structure of the

polishing marks will be discussed below. Polishing marks were not observed on the Cs implanted into glassy carbon at room temperature as well as at 600°C. Increasing the substrate temperature during implantation increased the cesium movement out to the surface. During the implantation process as the incident cesium ions were implanted into the substrate some were diffusing out at a rate, which depended on the temperature. Thus ultimately a layer of cesium was formed on the surface of glassy carbon during higher temperature implantations. Due to minimization of the surface energy (Gibbs energy) hollow regions will first fill-up leading to the absence of the polishing marks in the SEM images for these 600°C implanted samples. The RBS spectrum in figure 6.13 shows a Cs peak that appear on the surface channel number (480). The dose of this Cs layer on the surface depends on the substrate temperature during implantation (see table 6.4).

Cesium has a melting point of 28.35 °C with an equilibrium vapor pressure of 2.91×10^{-4} Pa. At its evaporation point of 676.9 °C it has an equilibrium vapor pressure of 1.38×10^{5} Pa. At annealing temperatures of 200 °C and 600 °C, the cesium equilibrium vapor pressures are 11.9 Pa and 6.09×10^{4} Pa, respectively. At annealing temperature of 600 °C, the equilibrium vapor pressure of cesium in greater than the equilibrium vapor pressure of iodine (34.2 Pa) at room temperature which illustrate that the surface Cs layer would evaporate/sublimate into vacuum and be pumped away.

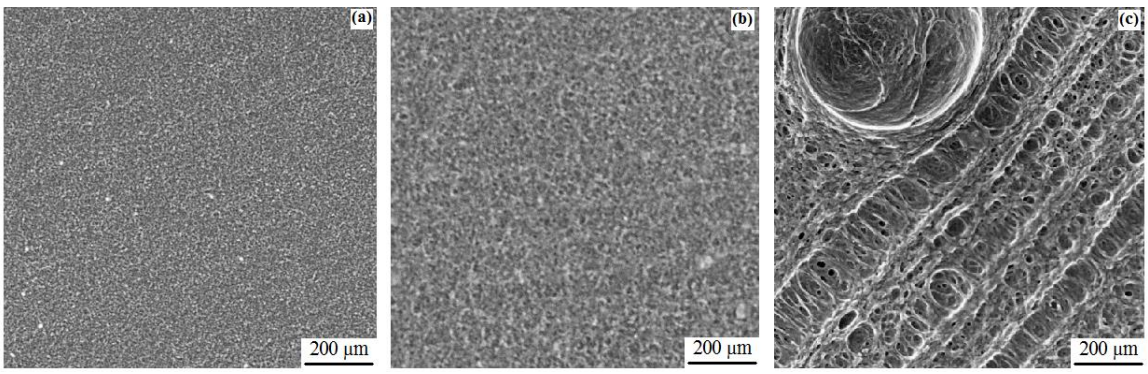

Figure 6.4 SEM micrograph of polished glassy carbon implanted with 360 keV cesium ions at a fluence of 2×10^{16} Cs^{+}/cm^{2} at (a) room temperature (RT), (b) 600 °C, and (c) the RT implanted sample annealed at 200 °C for 8 hours.

A sponge-like structure inside the micro-pores or cavities could be clearly seen on the annealed sample. This feature was not seen in the virgin glassy carbon before implantation. For

clear observation of the feature explained, a higher magnification SEM image of figure 6.4 (c) was taken as shown in figure 6.5. The structure inside the micro-pore can be clearly seen. This structure is in accordance with the model of a fullerene related structure for commercial glassy carbon consisting of fragmented curved sheets of carbon proposed by Harris [3]. Similar results were observed after glassy carbon was implanted with 100 keV N^+ ions to a dose of 4 x 10^{17} N^+/cm^2 [4]. However, an alternative explanation was given for the observed structure. They proposed that the nitride formation at the deeper depth could rupture the material inside the micro-pore to form the sponge-like structure [4]. It is, however, also possible such rapture process could expose the Harris-proposed microstructure of glassy carbon.

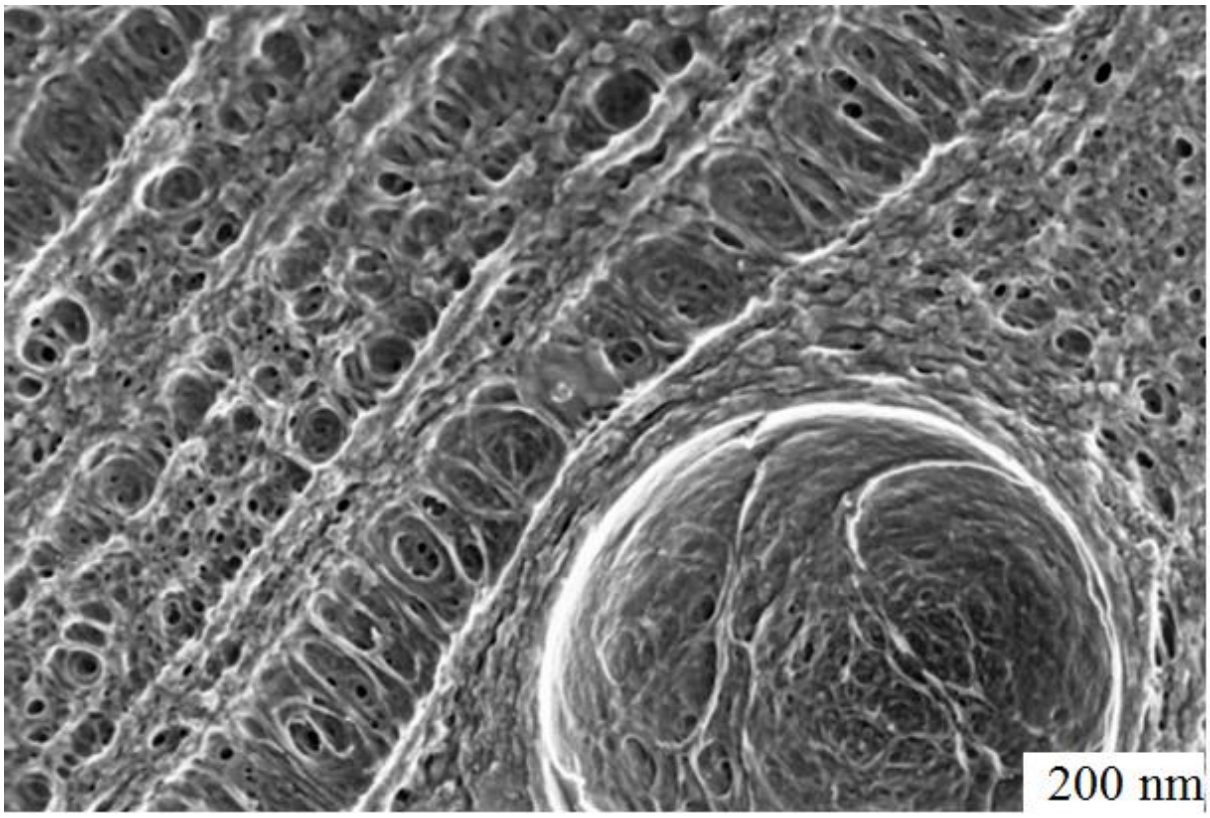

Figure 6.5 SEM micrograph of polished glassy carbon implanted with 360 keV cesium ions at a fluence of 2×10^{16} Cs^+/cm^2 at room temperature (RT) then annealed at 200 °C for 8 hours. This is a higher magnification SEM image of figure 6.4 (c).

To investigate the effect of laser beam annealing during Raman measurements at high power, the glassy carbon implanted with cesium at room temperature was placed under the Raman laser beam at a power of 90 mW for 10 minutes. This means that an energy of about 60 J was added to the surface of the glassy carbon sample in a concentrated spot. Figure 6.6

shows the SEM micrograph of the spot where the laser beam was focused and a hole is observed. Since the laser annealing is done under ambient air and moisture, the cesium ignites spontaneously in the presence of air and reacts explosively in water [5]. During this explosive reaction carbon atoms on the damaged layer were removed, exposing the bulk of the material that was not affected by implantation. This also means the depth of the hole is directly related to the depth of cesium into the glassy carbon during implantation. Figure 6.6 also reveals the polishing marks underneath the glassy carbon layer implanted with cesium, implying that mechanical polishing creates damages on the surface that goes deep into the sample. The significance of this is that laser beam annealing was effecting in etching out only the damaged layer of the glassy carbon. The level of increase in the damage of the implanted glassy carbon layer is observed by the Raman spectrum broadening of the D and G peaks. A heavily damaged implanted layer was illustrated by a broad asymmetric Raman spectrum centred on 1500 cm^{-1}. This will be discussed further in the next section.

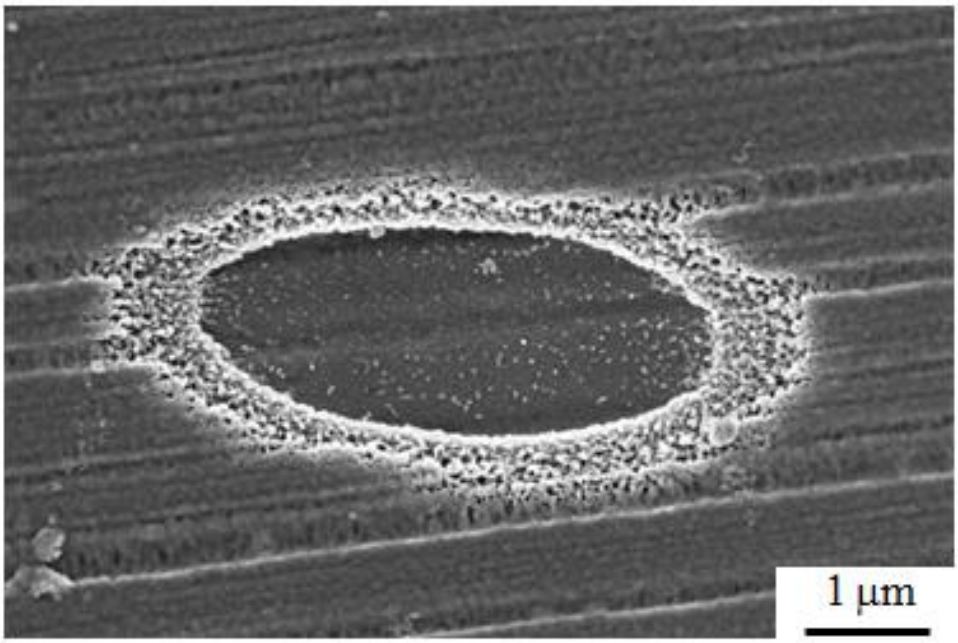

Figure 6.6 SEM micrograph of glassy carbon implanted with 360 keV cesium ions at a fluence of 2×10^{16} Cs^{+}/cm^{2} at room temperature (RT) and laser beam annealed.

6.2 RAMAN SPECTROSCOPY RESULTS

Though the glassy carbon was implanted separately with cesium and silver, we only present the Raman measurements for the cesium implanted samples. We chose to do Raman measurements on the cesium implanted glassy carbon since it is little heavier than silver though similar damages are expected. Raman spectroscopy with the 514.5 nm line of an Inova 70v argon laser was used to monitor the changes induced in glassy carbon as a result of irradiation with cesium and the subsequent heat treatment. Figure 6.7 shows the Raman spectrum of a polished virgin glassy carbon sample. Though not presented in this study, the Raman spectrum of the as-received glassy carbon is the same as the polished one. The spectrum of the intact glassy carbon surface, which is a disordered carbon, showed two sharp peaks, namely the D (disorder) and G (graphite) peaks at 1350 cm^{-1} and 1592 cm^{-1}, respectively. It is worth mentioning a significant fact that for disordered carbons, the Raman spectra are dominated by these D and G modes of graphite even when the carbon does not have a particular graphitic order [6]. One reason for the dominance of the D and G modes is that the Raman spectrum of a disordered carbon like glassy carbon, is dominated by the sp^2 sites. The σ- and π-bonds, which were explained in chapter 1, have different energies. The π-bond has a lower energy that the σ-bond and that makes it more polarizable. This gives the sp^2 sites a larger Raman cross section than sp^3 sites, so they dominate the Raman spectrum [7]. The existence of the G band illustrates the existence of the sp^2 carbon network. The sp^3 and sp carbon network show the characteristic Raman features at 1333 cm^{-1} (diamond) and in the range 1850–2100 cm^{-1} (linear carbon chains), respectively [8]. Thus we consider the appearance of the D peak on the glassy carbon surface at 1350 cm^{-1} not only as a defect induced Raman feature but also to characterize the presence of the sp^3 carbon network. However, it is worth noting that the intensity of the D peak has no relation to the amount of the sp^3 bonds, but only indicates their existence in glassy carbon. A large intensity of the D peak implies large number of sp^2 clusters [9]. Though *Cuesta* and coworkers reported that in graphite and well organized materials the D peak has a low intensity that the G peak. For more disordered solids the D peak becomes equivalent or more than the G peak [10].

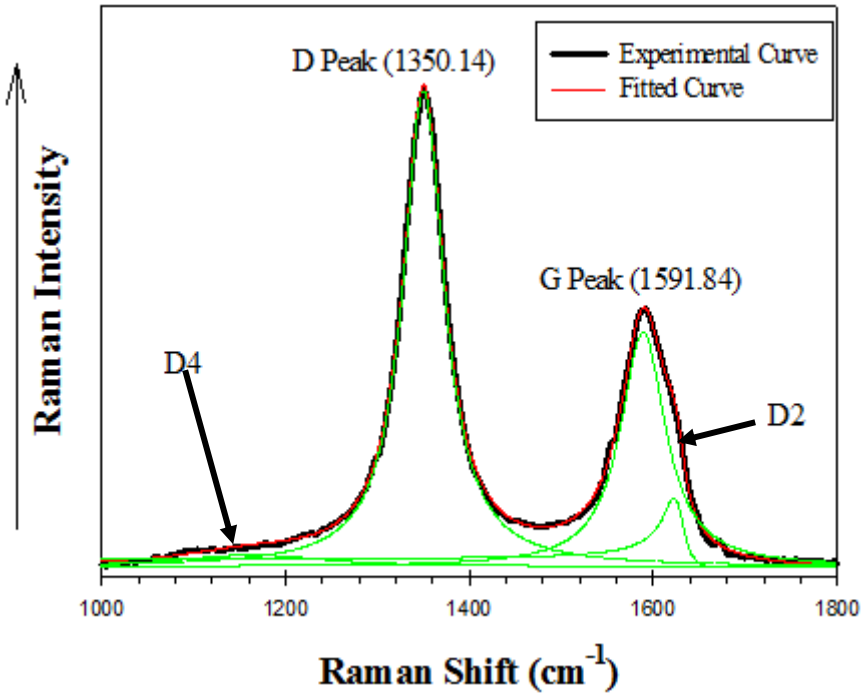

Figure 6.7 Raman spectrum of polished glassy carbon.

Curve fitting for analysis and determination of spectral parameters of the first order Raman bands was performed with the software program Origin Pro 8.1. The goodness of fit was indicated by the reduced R^2 value which is also known as the coefficient of determination. This value would be unity for the perfect agreement between the calculated fit and the experimental spectrum. Several fitting procedure were compared before selecting the most accurate one. In this study, the Lorentzian and Breit-Wigner-Fano (BWF) functions were used and this are given by the equations:

Lorentzian equation

$$y = y_0 + \frac{2A}{\pi}\frac{w}{4(x-x_c)^2+w^2} \tag{6.1}$$

where y_0 = offset, x_c = center, A = area and w = full width at half maximum (FWHM).

Breit-Wigner-Fano (BWF) equation

$$y = y_0 + \frac{H\left(1+\frac{x-x_c}{qw}\right)^2}{1+\left(\frac{x-x_c}{w}\right)^2} \tag{6.2}$$

where y_0 = base, x_c = center, H = height, q = skewness factor (asymmetry) and w = full width at half maximum (FWHM).

For the Raman spectrum shown in figure 6.7, we used two Lorentzian functions for the D4 (1164) and D (or D1) (1350) bands, and two Breit-Wigner-Fano (BWF) functions for the G (1592) and D2 (1624) bands. This gave the R^2 value of 0.9944427 indicating the goodness-to-fit of the calculated fitted curve (red line) to the experimental spectrum (black line). From earlier studies [11] it was revealed that all five first order Raman bands (G, D1, D2, D3, D4) for soot have to be taken into account for a complete analysis and interpretation of the first order spectral region (1000–2000 cm^{-1}). Soot, is primarily composed of greater than 80% carbon comprising of crystalline and amorphous material and their results are shown in figure 6.8. The parameters of the G and different D peaks found in our study and those from [11] are given in table 6.1. The D3 peaks in our study was not fitted because it gave a large value for the coefficient of determination R^2, hence living it out we got a reduced value as mentioned above.

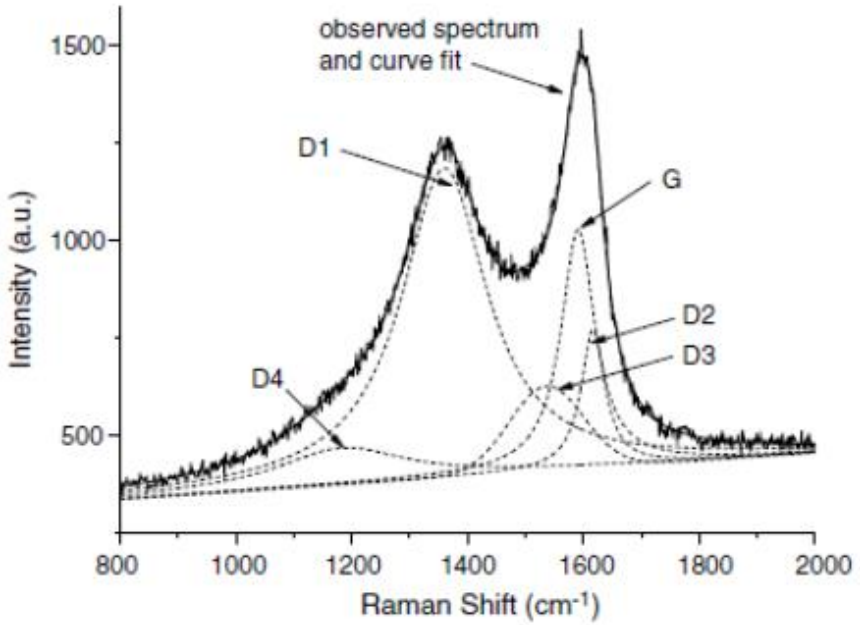

Figure 6.8 Curve fit with band combination for the first order Raman spectra (λ_0 = 514 nm) of soot [11].

Table 6.1 Parameters of the G and different D peaks of glassy carbon and soot.

	Glassy carbon	Soot [11]
G	1592 cm^{-1}	1580 cm^{-1}
D1 (D)	1350 cm^{-1}	1350 cm^{-1}
D2	1624 cm^{-1}	1620 cm^{-1}
D3	—	1500 cm^{-1}
D4	1164 cm^{-1}	1200 cm^{-1}

The ratio of the D and G band intensities (I_D/I_G) has been used for many years to estimate the crystallite sizes L_a in disordered carbon materials. From the Tuinstra-Koenig relationship, the general equation for the determination of the crystallite size L_a in the visible range is given by the empirical formula

$$L_a(\mathrm{nm}) = C_\lambda \left(\frac{I_D}{I_G}\right)^{-1} \tag{6.3}$$

where C_λ is the constant of proportionality between L_a and $(I_D/I_G)^{-1}$ [12]. This constant is laser wavelength dependent and for 514.5 nm laser excitation, as was used in this study, it was taken as 44 Å [12][9][13]. In this equation the integrated intensities (areas) of the D and G bands were considered instead of using the ratio of the peak amplitudes. From the Lorentz and BWF fittings, we found the ratio (I_D/I_G) = 1.32 and the G peak full width at half maximum (FWHM) of 61.14 ± 0.43 cm^{-1} which is a measure of disorder and increases continuously as the disorder increases [14][6]. Using equation (6.3) on the Raman spectrum given in figure 6.7 with the ratio (I_D/I_G) = 1.32 and the 514.5 nm laser line wavelength (E_{laser} = 2.41 eV) used in the experiment, the crystallite size L_a of the un-implanted polished glassy carbon was calculated to be 3.32 nm. Jenkins and his colleagues obtained the crystalline sizes ranges from 2 to 6 nm for commercial glassy carbon prepared by heat treatment ranging from 900 to 2700 °C [15].

The ion implantation into glassy carbon changes the Raman spectrum showing that the D and G peaks merged into a broad peak indicating amorphization of the glassy carbon [9]. In figure 6.9 we show the Raman spectra of the glassy carbon implanted with 360 keV cesium ions to a fluence of 2×10^{16} Cs^{+}/cm^{2} at different substrate temperatures, i.e. room temperature (blue curve), 350 °C (green curve) and 600 °C (red curve) together with the un-implanted polished glassy carbon (black curve). Also shown in the figure are the fits of the Lorentzian-BWF line shape combination represented by the dotted line on each curve. The fitted curves were used to calculate the G peak full width at half maximum (FWHM) and the parameters of the G and D peaks. These parameters of the D and G peaks are shown in table 6.2. For implantation with the substrate at room temperature (blue line), it is observed that glassy carbon is greatly damaged with no clear distinct appearance of the D and G peaks. But at the highest substrate temperatures both the D and G peaks could be observed. This is attributed to the fact that at high implantation temperatures, the atoms of the substrate material (glassy carbon) have the mobility to retain some of their original structure in the bulk of the damaged region.

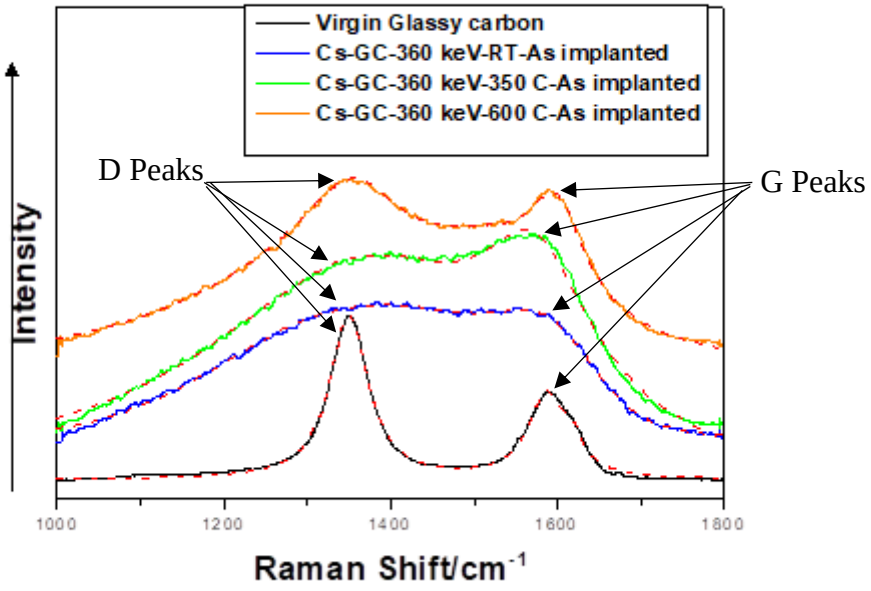

Figure 6.9 Raman spectra of the glassy carbon implanted with 360 keV cesium ions to a fluence of 2×10^{16} Cs^{+}/cm^{2} at substrate temperatures of room temperature (blue curve), 350 °C (green curve) and 600 °C (red curve) together with the un-implanted polished glassy carbon (black curve). The dotted lines in all the spectra represents the fits of the Lorentzian-BWF line shape combination.

Comparing the glassy carbon sample implanted with cesium at 350 and 600 °C substrate temperature, the radiation damage is less at higher implantation temperature. Meaning that at lower substrate implantation temperature, glassy carbon is more amorphous as compared to higher temperature. Observed from figure 6.9 was that there is a slight Raman shift to the right of the G peak position and a decrease in the G peak FWHM as the substrate temperature is increased. Those changes confirmed that the amount of sp^2 conversion to sp^3 in the 350 °C implanted sample is higher than the 600 °C [6][16]. The G peak FWHM has been widely used to determine the crystallinity of carbon materials, where the crystalline carbon materials shows a sharper Raman G peak than amorphous carbon material [17].

After implantation of cesium into the glassy carbon substrate at the various conditions mentioned earlier, damages-related defects are introduced into the substrate. Tuinstra and Koenig (TK) [12] did a comparative study between XRD and Raman spectroscopy on carbon materials to establish the relation between ratio I_D/I_G and the crystallite size L_a. They reported that the ratio I_D/I_G varied inversely with the crystallite size L_a. Knight and White have shown that this relation holds for wide a range of sp^2 bonded carbons over the range of $2.5 < L_a < 300$ nm for laser wavelength of 488 and 514.5 nm [18]. Furthermore, it was reported that L_a increased with heat treatment for disordered carbons [19]. The G and D peak parameters extracted from the fits to the data in figure 6.9 for the glassy carbon implanted with 360 keV cesium ions to a fluence of $2 \times 10^{16}\,Cs^+/cm^2$ at substrate temperatures of room temperature, 350 °C and 600 °C are shown in table 6.2. Using the Tuinstra-Koenig equation (6.3) on the Raman spectra of these implanted samples with the ratios I_D/I_G, their crystalline size L_a of the as-implanted samples were calculated (see table 6.2). Despite the large errors involving extracting the ratio of the D and the G peaks from the broad and overlapping D and G peaks, a clear trend is evident of the decrease in the I_D/I_G as a function of increasing substrate temperature during implantation.

Ferrari and Robertson [20] proposed an alternative equation for the calculation the crystallite size where defects are progressively introduced into the graphite layer, viz.

$$L_a^2 C_\lambda^{'} = \frac{I_D}{I_G} \qquad (6.4)$$

C'_λ is the constant of proportionality between L_a^2 and I_D/I_G [20]. The constant C'_λ used in for 514.5 nm laser excitation ≈ 0.0055 $Å^{-2}$. For interest, we also calculated the crystalline size L_a using the equation 6.4 and are also shown in table 6.2. The crystallite sizes are below 2 nm and decreasing. This is in contrary with the expected increase in crystallite size as the implantation temperature increases, making equation 6.4 invalid in this study.

Table 6.2 Parameters of the G and D peaks for the glassy carbon implanted with 360 keV cesium ions to a fluence of 2×10^{16} Cs^+/cm^2 at substrate temperatures of room temperature, 350 °C and 600 °C.

		Cs□GC□RT	Cs□GC□350°C	Cs□GC□600°C
D Peak	Position	1379.51 cm□1	1368.09 cm□1	1355.76 cm□1
	Intensity Amplitude (ID)	437.49	484.90	413.83
	Width	482.78 cm□1	416.09 cm□1	268.75 cm□1
G Peak	Position	1579.10 cm□1	1574.56 cm□1	1601.61 cm□1
	Intensity Amplitude (IG)	207.14	400.82	438.97
	Width	144.21 cm□1	161.32 cm□1	158.88 cm□1
Intensity Ratio (ID/IG)		2.14	1.21	0.94
La (Equation 6.3-TK)		2.06 nm	3.64 nm	4.68 nm
La (Equation 6.4)		1.96 nm	1.48 nm	1.31 nm

The G peak parameters, i.e. the full-width at half maximum (FWHM) and peak position, extracted from the fits to data in figure 6.9 are plotted as a function of implantation temperature in figures 6.10. It was evident from the calculations that there was an increase in the FWHM of the individual G peak after implantation at room temperature. However, this decreased as the

substrate temperature increased. The increase in the G peak width after room temperature implantation was attributed to an increase in the bond angle disorder and the introduction of point defects such as interstitials and vacancies in the graphite-like planes [21]. The subsequent decrease in FWHM for higher temperature implantations mean that more defects are created at room temperature implantation as compared to the higher temperature implantations. This is supported by the downward shift in the G peak position after ion implantation. A change in the bond angle away from the ideal 120° results in the decrease in the frequency of the G peak. Therefore, the observed decrease in the G peak position indicates that the level of disorder has increased sufficiently to change the average bond angle within the implanted layer away from 120° [22].

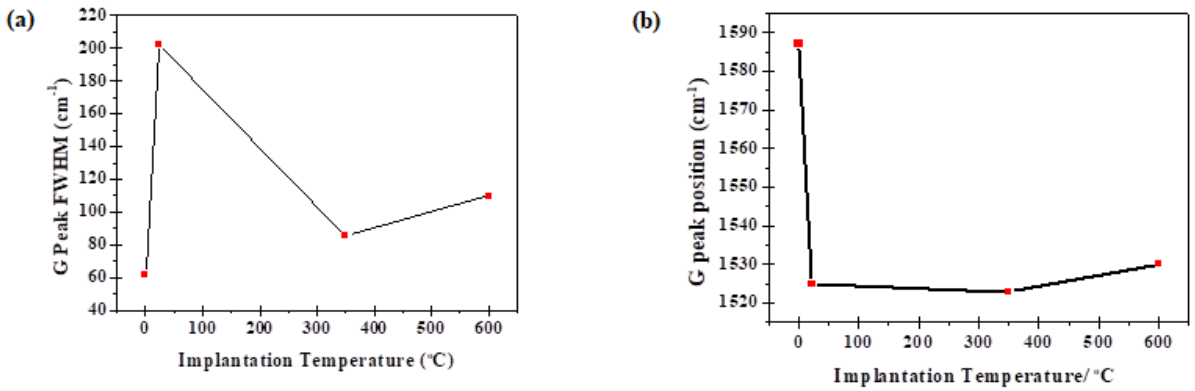

Figure 6.10 The (a) FWHM and (b) position of the G peak plotted against the substrate implantation temperature.

Figure 6.11 shows the Raman spectra of glassy carbon implanted with cesium at room temperature and individually annealed for one hour at temperatures ranging from 300°C to 1200°C. From the point of view of the above results glassy carbon was transformed into amorphous carbon during the implantation process. The Raman spectra did not change much for lower annealing temperatures of 300°C to 400°C. Lower annealing temperatures up to 500°C did not show much difference on the intensity of the D- and the G-peaks. At higher annealing temperature from 600°C a clear distinct appearance of the two peaks was seen. We also observed that the amorphous layer is partially annealed at the higher temperatures up to 1200°C. The G peak shifted towards the right and also became narrower with increasing annealing temperatures. The Raman shift to the right and the narrowing of the G peak can be

attributed to the decrease in the bond angle disorder and an increase in the crystalline size [23]. On the other hand the D peak position remained constant at all annealing temperature.

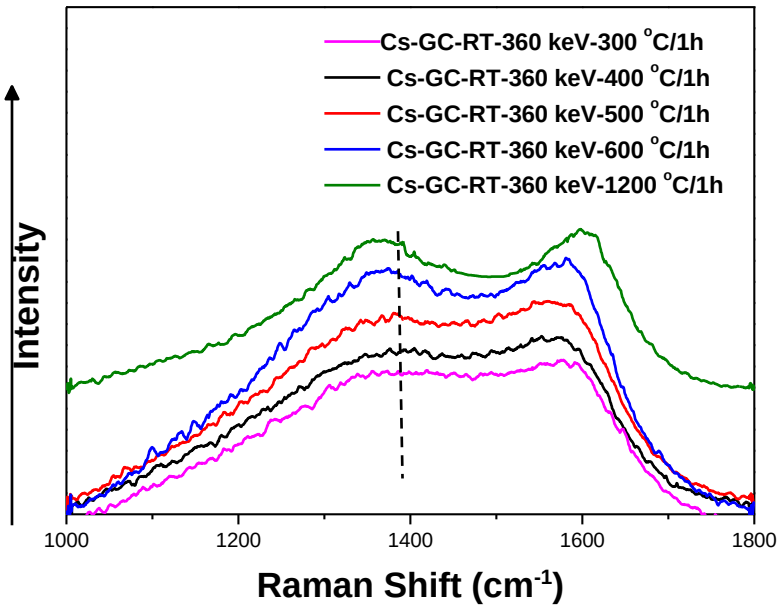

Figure 6.11 Raman spectra of cesium implanted glassy carbon at room temperature then annealed from 300 to 1200 °C for 1 hour.

The intensity of the G peak become higher than the D-peak as the temperature increased from 600°C to 1200°C. This means a decrease in the ratio (I_D/I_G) with increasing annealing temperature and a corresponding increase in the average graphitic crystal sizes. Dillon and coworkers also observed the decrease in the ratio (I_D/I_G) at high annealing temperatures and they interpreted their results as follows. For amorphous glassy carbon, i.e. lower annealing temperature, the crystalline size and number are too small to couple effectively to the incoming laser beam, thus they contribute little to the Raman spectrum [16]. The G and D peak parameters extracted from the fits to data in figure 6.11 for the glassy carbon implanted with 360 keV cesium ions to a fluence of 2×10^{16} Cs^+/cm^2 at room temperature then annealed separately at 300°C, 400°C, 500°C, 600°C and 1200°C for 1 hour are shown in table 6.2. Again using equation (6.3) on the Raman spectra of these implanted samples with the ratios I_D/I_G, their crystalline size L_a of were calculated. At annealing temperatures between 500 and 1200 C the intensity ratios I_D/I_G decreased and the crystalline sizes L_a increased as the annealing temperature increased, which is what was expected. The problem was the intensity ratios I_D/I_G

and the crystalline sizes L_a at the lower annealing temperature, 300 and 400 C, can have an error in the fitting, giving incorrect answers.

Dillon and co-workers [16] found similar results when they were investigating disorder and crystallite formation in carbon films prepared by ion-beam sputtering of carbon target in argon ions. They found that as the annealing temperature of amorphous carbon was increased, the intensity ratios I_D/I_G initially increased up to temperature of 800°C, after the ratio decreased. They interpreted their results as follows. (i) For the increase in the intensity ratios I_D/I_G: at low annealing temperatures the crystallites are small in size and number, and thus contribute little to the Raman spectrum. As the annealing temperature is increased, the crystallites grow in size and/or number, and thus contribute to the Raman spectrum, causing the intensity ratios I_D/I_G to increase reaching a maximum at 800°C. (ii) For the decrease in the intensity ratios I_D/I_G at higher temperatures (above 800°C): as the crystal grows, the effect of momentum conservation begin to increase in importance (since momentum is conserved in a large crystal), and thus the intensity ratios I_D/I_G decreases.

Table 6.3 Parameters of the G and D peaks for the glassy carbon implanted with 360 keV cesium ions to a fluence of 2×10^{16} Cs^{+}/cm^{2} at room temperature then annealed separately at 300°C, 400°C, 500°C, 600°C and 1200°C for 1 hour.

Cs-GC-350keV-RT annealed for 1 hour at		300°C	400°C	500°C	600°C	1200°C
D Peak	Position	1362.70 cm^{-1}	1366.96 cm^{-1}	1366.52 cm^{-1}	1369.33 cm^{-1}	1364.13 cm^{-1}
	Intensity Amplitude (I_D)	396.16	446.61	805.04	373.01	342.68
	Width	384.64 cm^{-1}	373.60 cm^{-1}	428.25 cm^{-1}	371.35 cm^{-1}	286.57 cm^{-1}
G Peak	Position	1590.90 cm^{-1}	1582.32 cm^{-1}	1583.94 cm^{-1}	1593.91 cm^{-1}	1613.47 cm^{-1}
	Intensity Amplitude (I_G)	387.28	426.52	534.34	379.68	559.43
	Width	157.30 cm^{-1}	204.12 cm^{-1}	167.02 cm^{-1}	233.55 cm^{-1}	170.09 cm^{-1}
Intensity Ratio (I_D/I_G)		1.023	1.047	1.507	0.982	0.613
(L_a)		**4.30 nm**	**4.20 nm**	**2.92 nm**	**4.48 nm**	**7.18 nm**

The glassy carbon implanted with cesium at room temperature then annealed for 300°C and 400°C for 1 hour shows near similar damage as the glassy carbon implanted with cesium at 350°C (See figure 6.12 (a)). However, comparing the cesium/glassy carbon sample implanted at 600°C and the room temperature implanted sample then annealed at 600°C for 1 hour, there is a distinct difference on the damages created on the glassy carbon substrate (See figures 6.12 (b)). The profile for that sample implanted at room temperature then annealed at 600°C for 1 hour was smoothened. There is more recrystallization of glassy carbon during implantation at the substrate temperature of 600°C than the Cs/GC implanted at room temperature then anneal at 600°C.

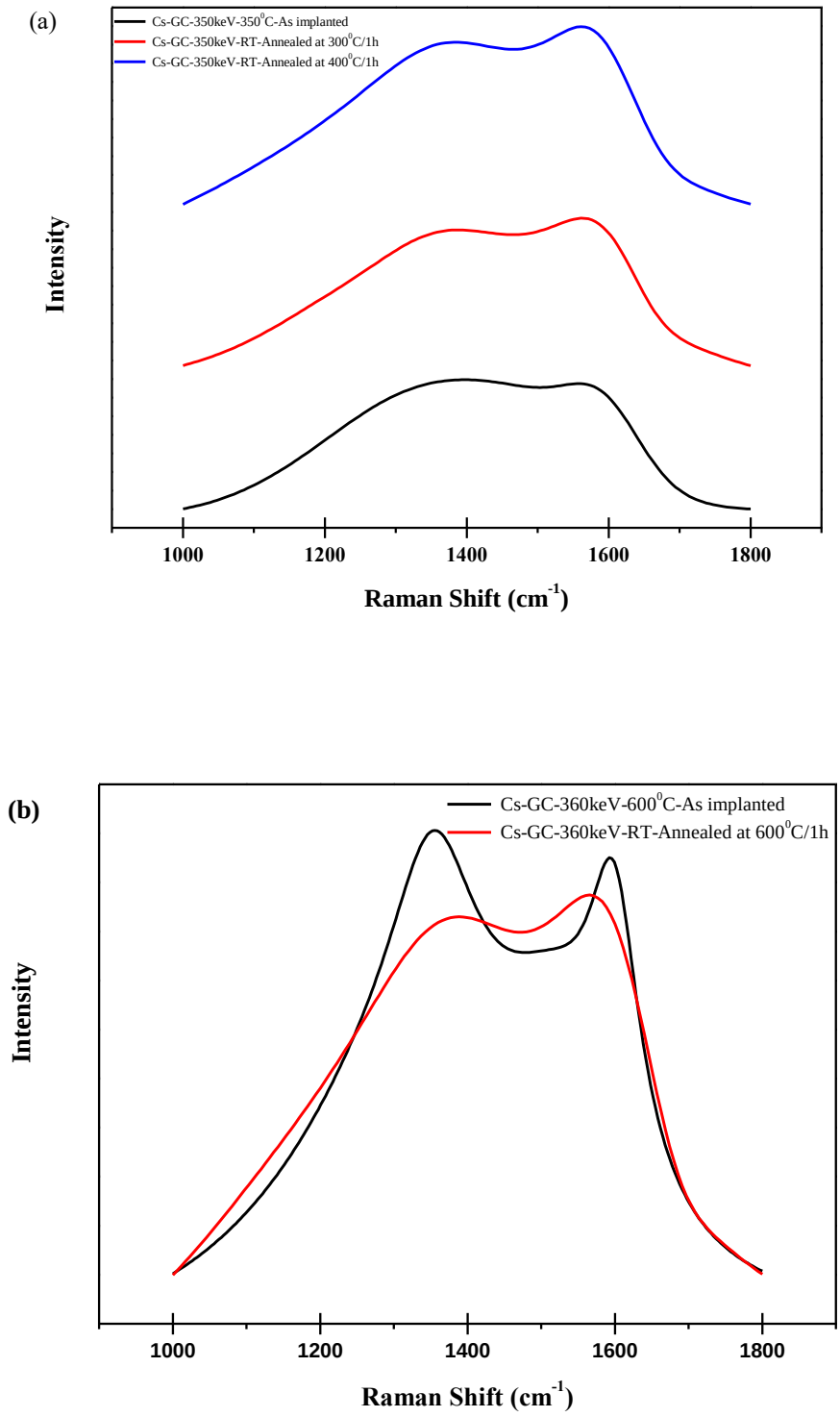

Figure 6.12 (a) The glassy carbon implanted with cesium at room temperature then annealed for 300°C and 400°C for 1 hour. (b) Cesium/glassy carbon sample implanted at 600°C and the room temperature implanted sample then annealed at 600°C for 1 hour.

6.3 RUTHERFORD BACKSCATTERING SPECTROMETRY RESULTS

Rutherford Backscattering Spectroscopy (RBS) analysis showed no in-diffusion of silver from the surface. As discussed in 6.1 this is attributed to the wetting problems of silver on glassy carbon surface. The investigation of in-diffusion of cesium deposited on the surface of glassy carbon was not performed. Similar to silver, the wetting problem of cesium on glassy carbon was anticipated. In this section the results of the investigation of the diffusion behaviour of cesium and silver, separately, implanted into glassy carbon are presented. RBS measurement was used to investigate the heat treatment of glassy carbon implanted separately with cesium and silver at room and high temperatures. The cesium and silver implanted glassy carbon measurements are given and discussed in sections 6.3.1 and 6.3.2, respectively.

6.3.1 GLASSY CARBON IMPLANTED WITH CESIUM

The RBS spectra of glassy carbon as-implanted with 360keV cesium ions at a fluence of 2×10^{16} ions/cm^2 at room temperature (RT), 350ºC and 600ºC are shown in figure 6.13. Usually an as-implanted profile of the implant is approximately Gaussian. Even the room temperature implanted profile is skewed towards the surface, showing that there is a diffusion of the implanted Cs towards the surface (see also figure 6.14). This out-diffusion of the Cs was enhanced at the two higher implantation temperatures with a distinct Cs surface peak being formed at the 600ºC sample. This was due to the substrate temperature effect and radiation-induced diffusion. The amount of Cs at the surface, with the surface channel number of 481 on glassy carbon, for the 600°C implanted sample was found to be about 1.33×10^{15} Cs^+/cm^2.

The small peak that appears at 500 is that of ~~the~~ tungsten and it only appeared for high temperature implantation. The tungsten originated from the tungsten element heating the substrate which was sputtered by the incoming beam of ions. Some of the sputtered tungsten deposited on the surface of the substrate. The peak at about 180 was identified to be oxygen.

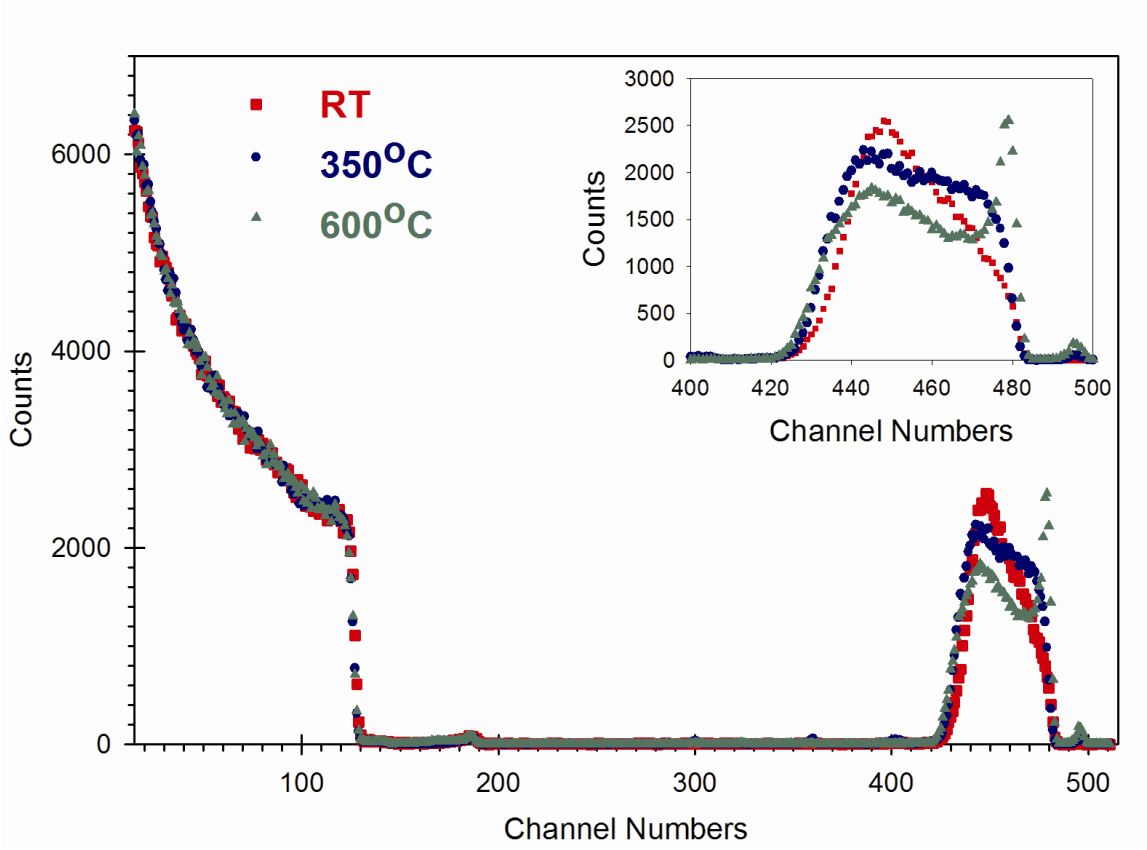

Figure 6.13 Glassy carbon implanted with 360 keV cesium ions to a fluence of 2×10^{16} Cs^{+}/cm^{2} at RT, 350 and 600 °C.

The RBS spectra show that although there is also some diffusion of the Cs into the bulk of the glassy carbon, but it is very little and does not extend deep into the bulk. This together with the diffusion/segregation towards the surface indicates that this diffusion is induced by the radiation damage in the glassy carbon. Due to knock-on effects and the Gaussian shape of the implanted ion distribution, the radiation-induced damage extends slightly beyond the implantation profiles as observed by RBS, thereby allowing some of the implanted Cs to diffuse into this damaged region. Using the data in plotting figure 6.13 and the surface channel number of cesium on glassy carbon (i.e. channel 480), we calculated the dose of Cs on the surface, as shown in table 6.4. These dose values were calculated using the spectral measurement program. The program calculated the area under the RBS spectrum from the cesium surface channel 481 to the last measured channel range of 511.

Table 6.4 The doses of cesium on the glassy carbon surface after implantation with 360 keV cesium ions to a fluence of 2×10^{16} Cs^{+}/cm^{2} at RT, 350 and 600 °C.

Substrate temperature	Dose
Room temperature	3.17×10^{14} Cs^{+}/cm^{2}
300°C	8.96×10^{14} Cs^{+}/cm^{2}
600°C	1.33×10^{15} Cs^{+}/cm^{2}

To determine whether the radiation-induced diffusion observed in figure 6.13 was purely a substrate temperature effect, we isochronally annealed the sample implanted at room temperature for 1 hour at temperatures ranging from 200ºC to 600ºC. It must be born in mind that it was expected that the room temperature implanted glassy carbon would have higher radiation damage than the samples implanted at elevated temperature. This was because of self-annealing usually taking place during high temperature implantations. The proof of this was observed from the Raman results given in figure 6.9. There we observed the room temperature implanted glassy carbon showed a broad spectrum with no clear distinction of the D- and G-peaks. While for the sample implanted at higher temperatures, the two mentioned peaks were observed. Implantation at higher temperature cause Cs to diffuse towards the surface, and remained on the surface. By calculating the areas under the Cs peaks on the surface of glassy carbon, we found that about 4.48% of the implanted Cs was lost during 350ºC and 6.65% during the 600ºC implantations.

We used SRIM [24] to calculate the damage (via vacancies) created by cesium implantation into glassy carbon. The plotted damage depth profile together with the SRIM depth profile and the measured depth profile is shown in figure 6.14. A reasonably good agreement between the calculated projected range of 206 nm and the depth at maximum Cs concentration in the measured profiles of 216 nm was observed. However, the experimental profile was not symmetric and confirms that already at room temperature implantation a strong redistribution of the implanted Cs ions took place.

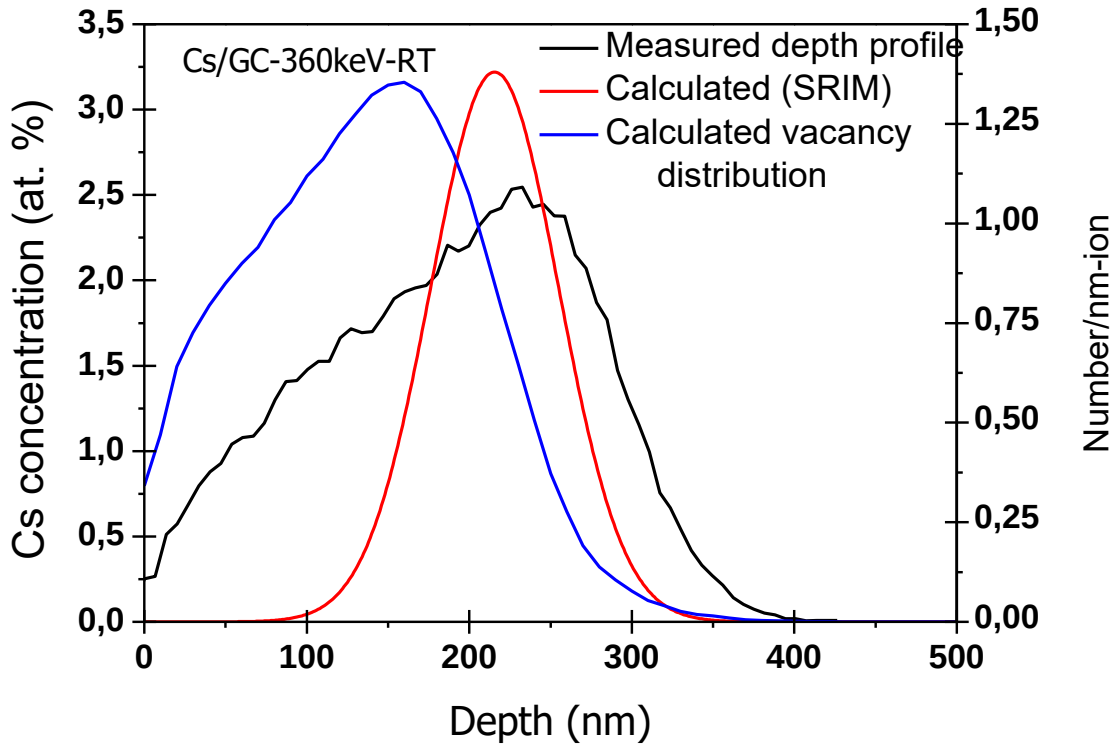

Figure 6.14 The RBS determined cesium concentration versus depth for glassy carbon implanted at room temperature with 360 keV cesium ions to a fluence of 2×10^{16} Cs^+/cm^2 (black line). For comparison the cesium depth profile (red line) and vacancy distribution (blue line) calculated with SRIM are included.

The RBS spectra of the glassy carbon implanted at room temperature with 360 keV cesium ions to a fluence of 2×10^{16} Cs^+/cm^2, and then annealed for 1 hour for temperatures ranging from 200°C to 600°C are shown figure 6.15. There were significant differences of the annealed samples in comparison with those implanted at higher temperatures (see figure 6.13).

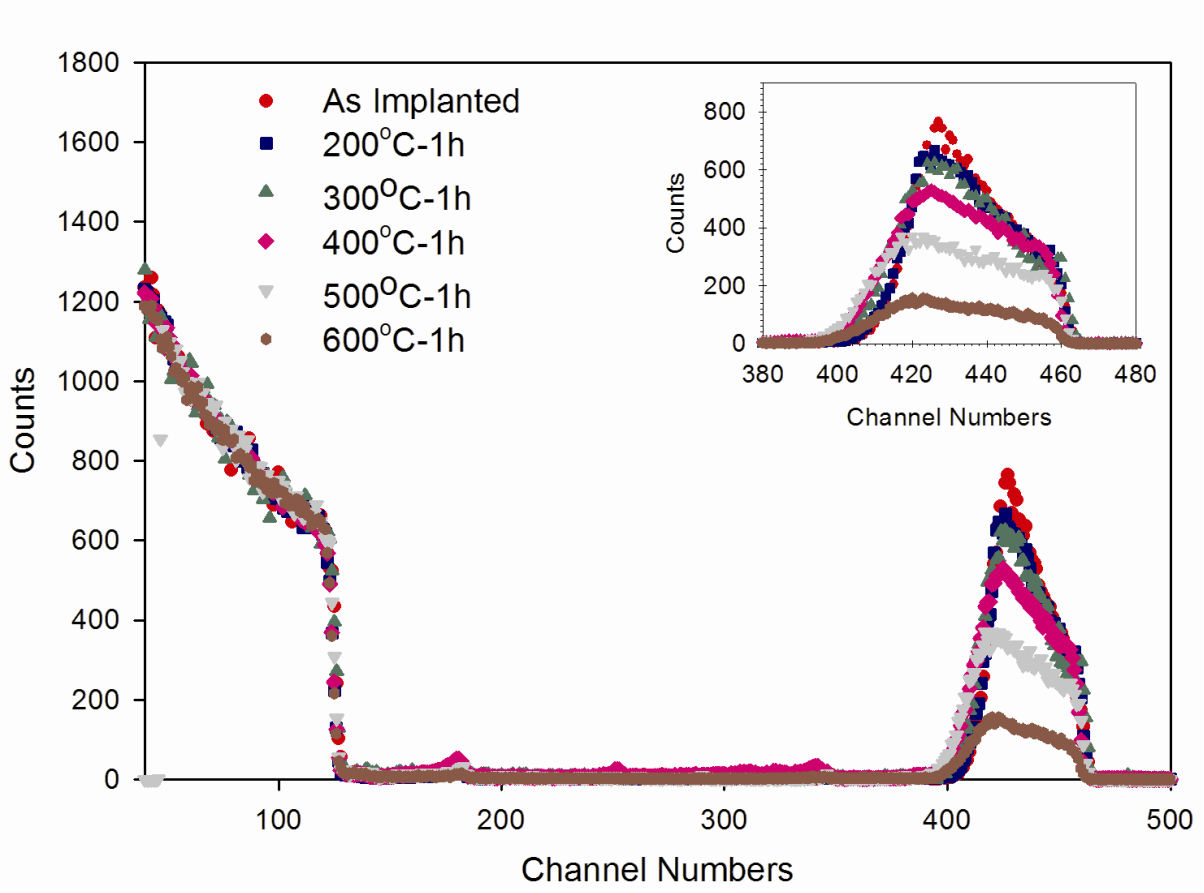

Figure 6.15 GC implanted with.360 keV cesium ions at a fluence of 2×10^{16} Cs^{+}/cm^{2} at RT, then isochronally annealed for 1 hour at 200, 300, 400, 500, and 600 °C.

In contrast, the room temperature implanted and then annealed samples lost significantly more Cs. The results are summarized in table 6.4. The out-diffusion profile shapes were also different. The Cs profiles of the isochronal annealed samples were consistent with an out-movement of Cs to the surface and a subsequent sublimation/evaporation of the Cs into the vacuum. This sublimation/evaporation of the Cs into the vacuum was due to the low melting point of 29°C of Cs. The out-movement was naturally temperature dependent which was stronger at the higher annealing temperatures resulting in the lowering of the concentration of the Cs depth profiles. From Fig. 6.15 it can be seen that there were Cs profile changes also at the bulk side of the glassy carbon as the samples were annealed. These profile changes showed some, but limited, Cs diffusion into the glassy carbon bulk due to the annealing. For the temperatures of 300°C – 600°C, the depth through which the Cs diffuse into glassy carbon is the same, suggesting that the initial ion bombardment-induced radiation damage plays a significant role in this in-diffusion process. This indicates that the Cs did not diffuse into the

pristine glassy carbon, only the damaged glassy carbon. This property would make glassy carbon a good containment of cesium.

Table 6.4. Percentages of cesium lost from GC implanted with 360keV cesium ions to a fluence of 2×10^{16} Cs^{+}/cm^{2} at RT, then isochronally annealed for 1 hour at 200ºC, 300ºC, 400ºC, 500ºCand 600ºC.

Annealing Temperatures	Cesium lost
200°C	1%
300°C	4%
400°C	6%
500°C	29%
600°C	72%

There is a significant difference between the room temperature implanted sample after annealing for 1 h at 600ºC and the sample implanted with the substrate being at a temperature of 600ºC. In the latter case the implantation time was about 30 min., i.e. shorter but comparable with the 1 h annealing of the former. The surprising and interesting aspect of this study was the sticking of the Cs to the glassy carbon surfaces during implantation at elevated temperatures. The evidence to this was observed by the existence of the cesium peak (see inset of figure 6.13) for the glassy carbon implanted with cesium at 600°C. This suggests that the implantation process at higher temperatures caused the replenishment of the Cs particle from the inside onto the surface of the glassy carbon. It is observed that cesium does move out of the glassy carbon. The movement does not follow the normal diffusion process of broadening of the profile governed by an Arrhenius type temperature dependence. Hence, the diffusion coefficient of cesium in glassy carbon were not calculated.

6.3.2 GLASSY CARBON IMPLANTED WITH SILVER

To study the diffusion behaviour of silver in glassy carbon, Ag was implanted at room temperature into glassy carbon. The projected range (R_P) of the 360 keV silver at a fluence of 2×10^{16} Ag^+/cm^2 implanted into glassy carbon was found to be 230.70 nm as compared to 210.56 nm obtained from SRIM calculation. The profiles are shown in figure 6.16. The experimental profile is slightly deeper (about 10%) as compared to the SRIM simulation. These two values agree with each other if a 5 % error in the depth is assumed for each profile. The silver profile is approximately Gaussian, which is in agreement with a typical ion implantation profile. The experimental and the theoretical values (SRIM) range parameters are summarized in table 6.3. The range straggling, ΔR_p, obtained experimentally is larger than the value predicted by SRIM. This was due to the fact silver migration to the surface was already taking place during implantation.

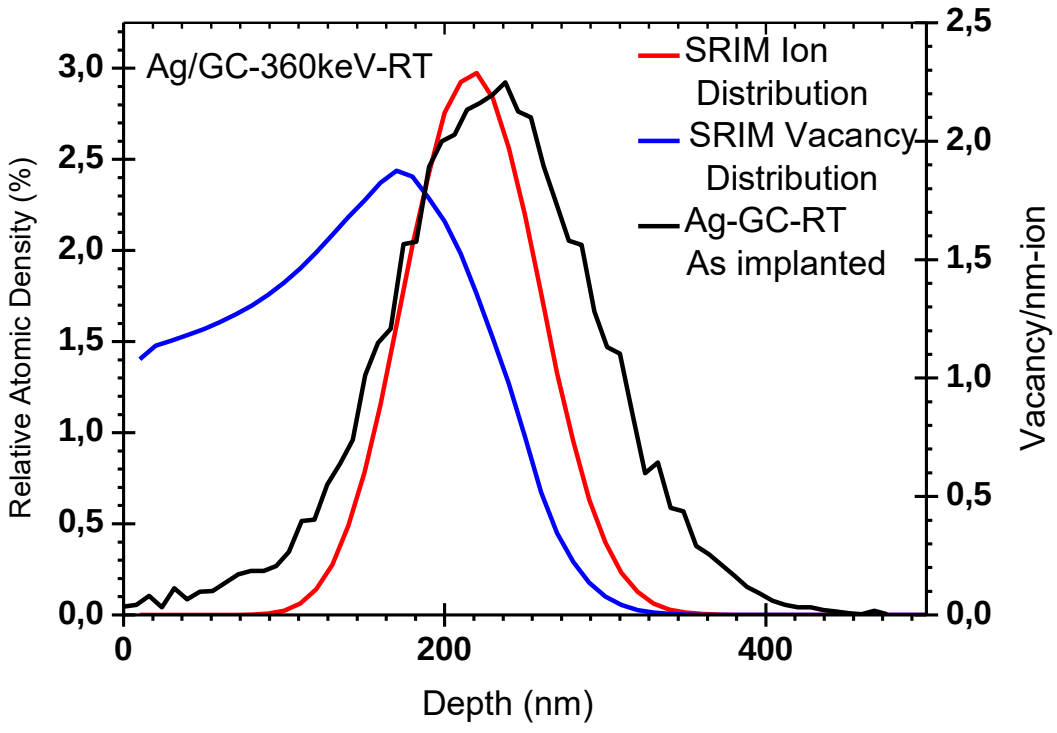

Figure 6.16 The RBS determined depth profile (black curve) of 360 keV Ag^+ implanted into glassy carbon is compared with a SRIM simulation (red curve). The vacancy distribution (blue curve) as calculated by SRIM is also shown.

The vacancy distribution, as calculated by SRIM, is also shown in figure 6.16. From this it can be seen that maximum vacancy distribution is ~ 170 nm which is significantly lower than the projected range of the experimental depth profile of the as-implanted silver. A large number of vacancies were concentrated towards the surface than in the bulk of the glassy carbon substrate. The vacancies could lead to radiation-enhanced (or even radiation-induced) diffusion of silver atoms. This will later explain the loss of silver of silver after heat treatment of the silver implanted glassy carbon at room temperature. The fact that the room temperature implanted silver into glassy carbon profile is fairly symmetric is supported by the skewness value of $\gamma = 0.117$, where the positive sign tell that the profile is skewed in behind of the projected ion range (R_P). When the profile is symmetric the skewness value is zero, and fairly symmetric if the value is between –0.5 and 0.5. The difference in the experimental and the theoretical moments, shown in tables 6.4, are due to a number of assumptions and neglects made by the SRIM program on the glassy carbon substrate. These include:

- The SRIM programs considered the target to be amorphous with atoms at random locations, and thus the properties of the crystal lattice are ignored. Glassy carbon has a fullerene-related structure.
- The implanted ion is assumed to change direction as a result of binary nuclear collision only and move in straight free-flight-paths between collisions, thus neglecting the effects of the neighbouring atoms.
- The recombination of interstitial atoms and the vacancies during implantation is neglected.

Table 6.4. The experimental and the theoretical (SRIM) range parameters.

	EXPERIMENTAL	SRIM
IONS PROJECTED RANGE (R_P)	230.7 nm	210.56 nm
STRAGGLING (ΔR_P)	62.80 nm	40.20 nm
SKEWNESS (γ)	0.117	0.0631
KURTOSIS (β)	3.485	2.8346
VACANCY DISTRIBUTION		~170 nm

The silver implanted glassy carbon sample was annealed to determine its diffusion in the glassy carbon. The goal with annealing is to obtain a diffusion profile that is distinctly different from the initial profile to indicate that noticeable diffusion has taken place. If the annealing time is too short or the temperature is too low, one might end up with a nearly uncharged distribution greatly increasing the uncertainty of the results obtained later by fitting. Figure 6.17 shows the RBS determined profiles of the glassy carbon implanted at room temperature with 360 keV silver ions to a fluence of 2×10^{16} Ag^{+}/cm^{2}, then isothermally annealed at 350°C for 30 minutes, 1 hour and 3 hours. When comparing the as implanted profile with profiles after annealing, all the annealed samples showed almost similar profiles.

The annealed profiles showed movement of silver, at the tails, towards the surface of glassy carbon and a little into the bulk of the material. The tail parts on both sides of the profile maximum are related to faster migrations. There was no broadening of the peaks after annealing and a very little reduction in the peak heights to indicate loss of silver out of the glassy carbon. The reason for the lack of movement of silver at this temperature could be that the activation energy of diffusion is too high in this temperature range. Also considering the fact that the diameter of silver atom is very large as compared to the localized open spaces in an amorphous carbon material. The above results indicated that these small localized openings could have trapped the silver atoms from diffusing out of and deeper into the glassy carbon.

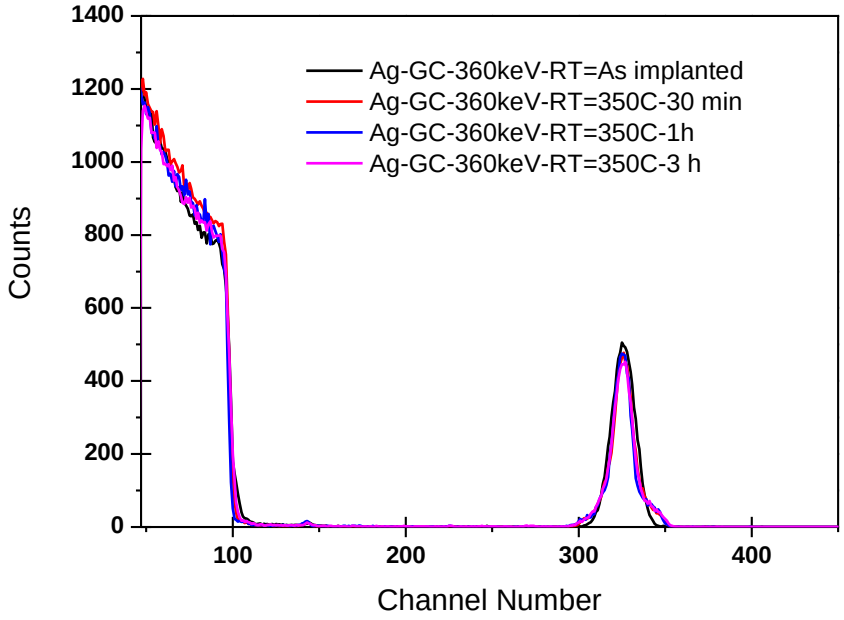

Figure 6.17 RBS determined profiles for glassy carbon implanted at room temperature with 360 keV cesium ions to a fluence of 2×10^{16} Ag^{+}/cm^{2}. The profile of the as-implanted sample is shown by the black line. Also shown are the profiles for samples isothermally annealed at 350°C for 30 minutes (red line), 1 hour (blue line), and 3 hours (pink line).

Figure 6.18 shows the RBS profiles of the as-implanted silver into glassy carbon sample annealed in vacuum for 1 hour at temperatures ranging from 400 to 700°C. As the annealing temperature increased there was a reduction in the silver peak but no clear broadening. It was also observed that from 500 to 600°C a lot of silver was lost. Interstitials and vacancies become mobile at high temperature (as in the present study) leading to rearrangement in the local bonding and the graphite-like crystallites with the defect region grow in size [25]. After annealing at 700°C, the silver disappeared completely from the glassy carbon and got lost into the vacuum.

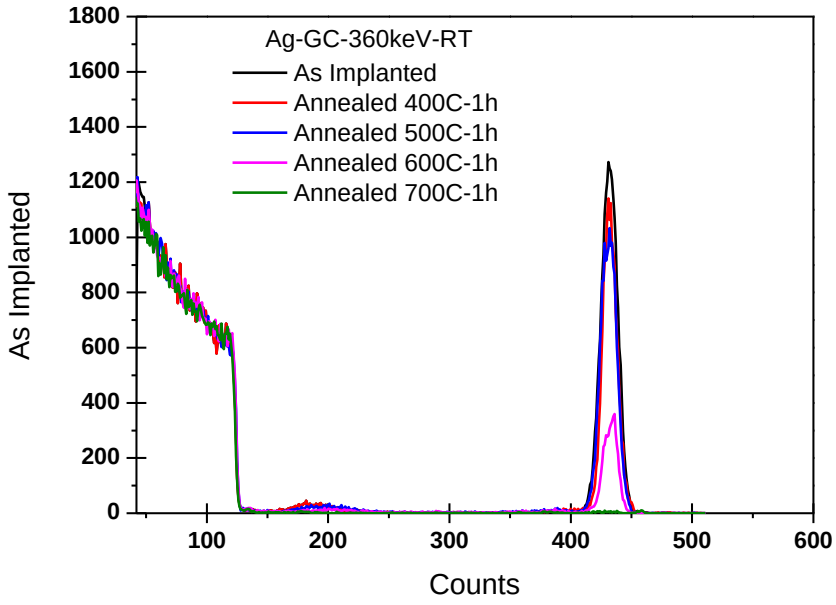

Figure 6.18 The RBS determined profiles of 360 keV Ag^{+} implanted into glassy carbon the annealed for 1 hour for temperatures ranging from 400 to 600°C

The optimum temperature of 575 °C was chosen for an isothermally annealing diffusion study for glassy carbon implanted with silver at room temperature. After the implanted samples isothermally annealed at this temperature for 2, 4, 8 hours, it was observed that silver did move out of the glassy carbon. Figure 6.19 shows the depth profile under these annealing conditions whereby the reduction in the peak height illustrate the loss of silver. It was believed that the movement of silver through the glassy carbon was through the pores and holes observed in figure 6.5. When arriving at the surface the silver sublimates under the influence of the elevated temperature and vacuum pumping. The loss of silver with increasing with annealing times does not follow the normal Fickian diffusion profile of broadening of the peaks.

Figures 6.17 and 6.18 clearly showed that there was no broadening of the silver peaks at the other increasing temperatures and times. Therefore, the loss of silver must be due to the migration of silver along the microscopic paths probably caused by radiation damage in glassy carbon during ion implantation process.

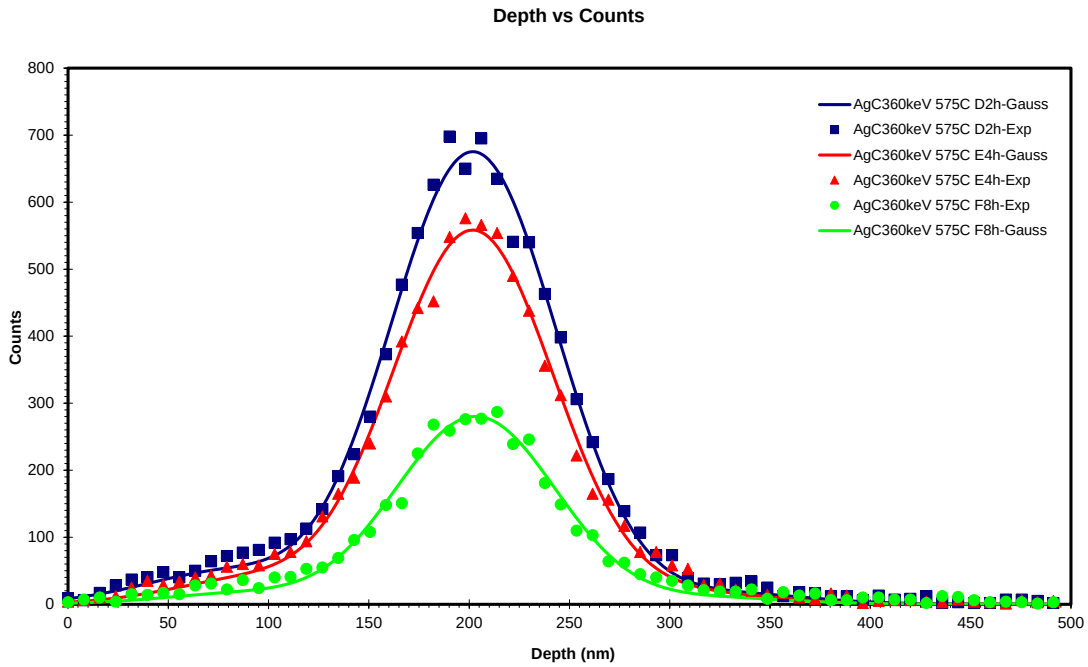

Figure 6.19 Depth profiles of 360 keV silver ions implanted to a fluence of 2×10^{16} Ag^{+}/cm^{2} into glassy carbon at room temperature and then isothermally annealed at 575°C for 2 (blue squares), 4 (red triangle), 8 hours (green solid cycles). The Gaussian fit of the profiles are also shown by the solid curves.

The profiles in figure 6.19 were fitted to the Breit-Wigner-Fano function to calculate the full width at half maximum $W(t)$. The linear function of $[W(t)]^2$ versus the annealing times was plotted as shown in figure 6.20. From equation 5.4, the gradient of the graph is

$$\text{Gradient} = 4D\ln 2 = -0.1496 \text{ nm}^2/\text{s}$$

therefore, the diffusion coefficient $D = 5.30 \times 10^{-2}$ nm^2/s.

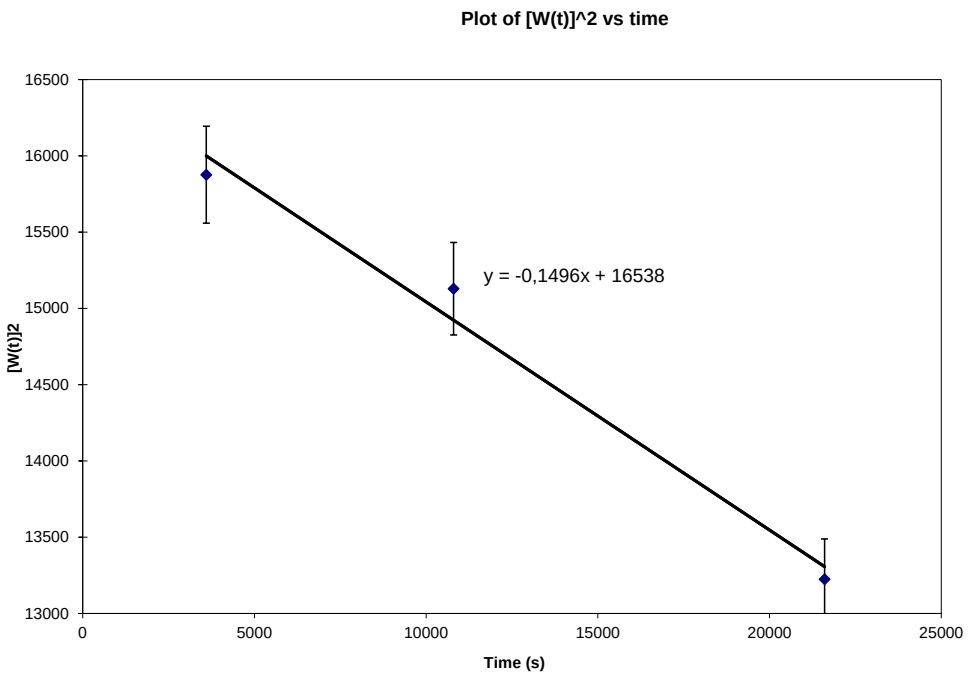

Figure 6.20 The graph of the square of the full width at half maximum $[W(t)]^2$ versus annealing times for the Ag implanted into glassy carbon substrate annealed isothermally at 575 °C.

6.4 REFERENCES

[1] B. WK, C. N, and F. FC, "BCF Theory," *Phil. Trans. Roy. Soc.*, p. 299, 1931.

[2] Y. Kazumata, "Surface erosion of pyrolytic graphite and glassy carbon by ion bombardment," *J. Nucl. Mater.*, vol. 71, pp. 178–180, 1977.

[3] P. J. F. Harris, "Fullerene-related structure of commercial glassy carbons," *Philos. Mag.*, vol. 84, pp. 3159–3167, 2004.

[4] K. Takahiro *et al.*, "Surface morphology of glassy carbon irradiated with nitrogen ions," *Nucl. Instruments Methods Phys. Res. Sect. B*, vol. 206, pp. 206–210, 2003.

[5] W. C. Butterman and H. E. Hilliard, "Mineral Commodity Profiles," 2005.

[6] A. C. Ferrari and J. Robertson, "Raman spectroscopy of amorphous, nanostructured, diamond-like carbon, and nanodiamond.," *Philos. Trans. A. Math. Phys. Eng. Sci.*, vol. 362, pp. 2477–2512, 2004.

[7] J. Robertson, "Diamond-like amorphous carbon," *Mater. Sci. Eng. R Reports*, vol. 37, pp. 129–281, 2002.

[8] M. . Pimenta, D. Dresselhaus, M. . Dresselhaus, L. . Cancado, A. Jorio, and R. Saito, "Stdying disorder in graphite-based systems by Raman spectroscopy," *Phys. Chem. Chem. Phys.*, vol. 9, pp. 1276–1291, 2007.

[9] V. Lavrentiev, J. Vacik, and H. Naramoto, "Structural phenomena in glassy carbon induced by cobalt ion implantation," *Appl. Phys. A*, vol. 92, pp. 673–680, 2008.

[10] A. Cuesta, P. Dhamelincourt, J. Laureyns, A. Martinez-Alonso, and J. M. D. Tascón, "Raman microprobe studies on carbon materials," *Carbon N. Y.*, vol. 32, pp. 1523–1532, 1994.

[11] A. Sadezky, H. Muckenhuber, H. Grothe, R. Niessner, and U. Pöschl, "Raman microspectroscopy of soot and related carbonaceous materials: spectral analysis and structural information," *Carbon N. Y.*, vol. 43, pp. 1731–1742, 2005.

[12] F. Tuinstra and J. Lo Koenig, "Raman spectrum of graphite," *J. Chem. Phys.*, vol. 53, pp. 1126–1130, 1970.

[13] M. J. Matthews, M. A. Pimenta, G. Dresselhaus, M. S. Dresselhaus, and M. Endo, "Origin of dispersive effects of the Raman D band in carbon materials," *Phys. Rev. B*, vol. 59, p. R6585, 1999.

[14] A. C. Ferrari and J. Robertson, “Resonant Raman spectroscopy of disordered, amorphous, and diamondlike carbon,” *Phys. Rev. B*, vol. 64, p. 075414, 2001.

[15] G. M. Jenkins, K. Kawamura, and L. Ban, “Formation and steructure of polymeric carbons,” *Proceeding R. Soc. London A*, vol. 327, pp. 501–517, 1972.

[16] R. O. Dillon, J. A. Woollam, and V. Katkanant, “Use of Raman scattering to investigate disorder and crystallite formation in as-deposited and annealed carbon films,” *Phys. Rev. B*, vol. 29, p. 3482, 1984.

[17] A. C. Ferrari, “Raman spectroscopy of graphene and graphite: Disorder, electron–phonon coupling, doping and nonadiabatic effects,” *Solid State Commun.*, vol. 143, pp. 47–57, 2007.

[18] D. S. Knight and W. B. White, “Characterization of diamond films by Raman spectroscopy,” *J. Mater. Res.*, vol. 4, pp. 385–393, 1989.

[19] G. A. Zickler, B. Smarsly, N. Gierlinger, H. Peterlik, and O. Paris, “A reconsideration of the relationship between the crystallite size La of carbons determined by X-ray diffraction and Raman spectroscopy,” *Carbon N. Y.*, vol. 44, pp. 3239–3246, 2006.

[20] A.C Ferrari and J. Robertson, “Interpretation of Raman spectra of disordered and amorphous carbon,” *Phys. Rev. B*, vol. 61, pp. 14095–14107, 2000.

[21] D. G. McCulloch, S. Prawer, and A. Hoffman, “Structural investigation of xenon-ion-beam-irradiated glassy carbon,” *Phys. Rev. B*, vol. 50, p. 5905, 1994.

[22] D. Beeman, J. Silverman, R. Lynds, and M. R. Anderson, “Modeling studies of amorphous carbon,” *Phys. Rev. B*, vol. 30, p. 870, 1984.

[23] S. Prawer, F. Ninio, and I. Blanchonette, “Raman spectroscopic investigation of ion-beam-irradiated glassy carbon,” *J. Appl. Phys.*, vol. 68, pp. 2361–2366, 1990.

[24] J. F. Ziegler, “SRIM Computer Code.” 2010.

[25] O. Koskelo, U. Koster, I. Riihimaki, and J. Raisanen, “Migration kinetics of ion-implanted beryllium in glassy carbon,” *Diam. Relat. Mater.*, vol. 17, pp. 1991–1993, 2008.

CHAPTER 7

CONCLUSION

The study presented in this thesis reports on the effects of ion implantation and subsequent vacuum annealing on the surface topography, structural changes and on the diffusion of cesium and silver into glassy carbon (Sigrador® G). The in-diffusion investigation was only done for the silver into the glassy carbon. The glassy carbon samples with 100 nm thickness layer of naturally occurring silver on their surface were vacuum annealed for 5 hours at temperatures of 600°C and 750°C. No silver in-diffusion was observed but the silver rather moved along the surface making island structures.

The summary and conclusions from the results obtained after several analysis on the samples implanted, separately, with cesium and silver are presented in the sections below.

7.1 CESIUM IMPLANTED GLASSY CARBON

Cesium ions were implanted into glassy carbon at 360 keV to a fluence of 2×10^{16} ions/cm^2 at room temperature, 350°C and 600°C. The SEM showed a great difference in the surface topography of the sample implanted at room temperature as compared to those implanted at higher temperatures. The room temperature implanted cesium implanted glassy carbon surface showed some polishing marks, though not prominent. But at the two higher implantation temperatures these marks were not visible by SEM. This was attributed to the cesium that diffuse from the glassy carbon to the surface making a layer that covers the polishing marks. Annealing the samples in vacuum, either the room or high substrate temperature implantation, the polishing marks and sponge-like structure inside the micro-pores or cavities could be clearly seen. The effect of laser bean annealing was investigated on the surface of glassy carbon implanted with cesium at room temperature. This was performed with a Raman laser bean at a power of 90mW for 10 minutes under ambient air and moisture. The cesium reacted explosively with air and water, and the damaged layer were removed, exposing the bulk of the material that was not affected by implantation

The effects on the structural changes induced in glassy carbon surface due to cesium ion implantation and subsequent annealing were investigated using Raman spectroscopy at a wavelength of 514.5 nm. The polished virgin glassy carbon surface showed two distinct peaks, namely the D (disorder) at 1350 cm^{-1} and G (graphite) peaks at 1592 cm^{-1}. The implantation of cesium into glassy carbon at room temperature resulted in a broad peak enclosing the D and the G peaks indication that the glassy carbon structure became amorphous. But at the highest substrate temperatures during cesium implantation both the D and G peaks could be observed.

The RBS spectra of the glassy carbon implanted with cesium at room temperature showed that there was redistribution and diffusion of the implanted Cs towards the surface. This out-diffusion of the Cs was enhanced at the higher implantation temperatures. A well-defined Cs peak on the surface of glassy was seen for cesium implanted into glassy carbon at 600°C. This was due to the substrate temperature effect and radiation-induced diffusion. Isochronal annealing of the room temperature cesium implanted glassy carbon for 1 hour at temperatures ranging from 200°C to 600 at room temperature, showed continuous redistribution and loss of cesium as the temperature was increased. Though cesium has a low melting point, there were still cesium ions remaining in the glassy carbon at annealing temperatures of 600°C

7.2 SILVER IMPLANTED GLASSY CARBON

Initially after implanting silver into unpolished glassy carbon surface, some cavities were observed with the SEM. These cavities were in the underlying layer of the surface of the glassy carbon and were an artifact of the glassy carbon manufacturing process. A secondary electron detector in the SEM with the sample tilted was used to confirm that what was observed were really cavities. In a subsequent experiment silver was implanted into a polished glassy carbon surface. The SEM micrograph obtained after glassy carbon polishing showed some polishing marks though not prominent. This was due to the fact that some of the glassy carbon material removed during polishing was loosely bonded to the surface/bulk of the glassy carbon substrate within the polishing marks. After silver implantation into the polished glassy carbon surface, the polishing mark were clearly visible. This was due to the preferred sputtering of the loosely bounded carbon atoms to expose the scratches.

RBS measurement were performed on the room temperature silver implanted into glassy carbon. The samples were isothermally annealed at 350°C for time times ranging from 30 minutes to 3 hours. Little diffusion or loss of silver was observed at this temperature and times. Though some movement of silver was observed, at the tails, towards the surface of glassy carbon and a little into the bulk of the material. Some samples were isochronally annealed for 1 hour for temperatures ranging from 400°C to 700°C. A clear loss of silver through the glassy carbon was observed by the reduction of the RBS silver area as the temperature increased. At 700°C the silver completely disappeared from the glassy carbon. To calculate the diffusion coefficient of silver into glassy carbon, the room temperature silver implanted glassy carbon was isothermally vacuum annealed at 575°C for 2, 4, 8 hours. Again the loss of silver was observed from the RBS spectra by a loss in the silver peak area. Though no clear broadening of the RBS depth profiles was observed as the annealing temperature increased, the depth profiles were fitted to the Breit-Wigner-Fano function. After fitting the RBS depth profiles of all the glassy samples implanted with silver at room temperature, then vacuum annealed at 575°C, the diffusion coefficient was calculated to be $D = 5.30 \times 10^{-2}$ nm^2/s.

From this study is was shown that silver or cesium does not diffuse through the undamaged bulk of the glassy carbon. This together with all other characteristic properties glassy carbon make it a possible future material for making nuclear waste containers.